Lithium isotope fractionation in magmatic systems: Constraints from *in situ* δ7Li determinations on magmatic minerals by femtosecond-laser ablation-MC-ICP-MS

Von der Naturwissenschaftlichen Fakultät der

Gottfried Wilhelm Leibniz Universität Hannover

zur Erlangung des Grades

Doktorin der Naturwissenschaften (Dr. rer. nat.)

genehmigte Dissertation

von

Lena Steinmann, M. Sc.

2020

Referent: Prof. Dr. Stefan Weyer

Korreferent: PD Dr. Ingo Horn

Tag der Promotion: 23.06.2020

Acknowledgements

Abstract

Investigations on the fractionation of stable metal isotopes to characterize mass flux at high temperatures have been proven to be a powerful tool during the past years. In this study, high precision *in situ* analyses on Li isotope ratios were performed on reference glasses and natural olivines at low concentration levels by femtosecond-laser ablation multi collector inductively coupled plasma mass spectrometry (fs-LA-MC-ICP-MS) in order to investigate the fractionation of Li isotopes during magma evolution.

The analytical technique was tested by analyzing a series of reference glasses *in situ* and cross calibrating them with published values acquired by other methods (solution nebulization MC-ICP-MS, SIMS and TIMS). The results of this methodical investigation showed that operating the plasma at relatively cool conditions (900 W) largely suppresses matrix-dependent isotope effects in the plasma. In order to achieve the best precision for concentrations ranging from 2 to 10 µg/g a detector combination of an ion counter for the determination of ^6Li and a faraday cup equipped with a $10^{13}\,\Omega$ amplifier for ^7Li was applied. Precise and accurate measurements of δ^7Li with ~2 ‰ (2 σ) analytical uncertainty were performed on reference glass T1-G (δ^7Li_{T1-G} = 1.6-2.4 ‰).

The fractionation of Li isotopes on the outcrop and mineral scale were investigated in this study. Bulk Li isotope analyses of an outcrop over a length of ~50 m in the French Massif Central showed that on the outcrop scale the isotopic composition varied between +2.1 and +3.3 ±2.0 ‰. The measured δ^7Li-values coincide with the range of unaltered volcanic whole-rock suites worldwide (+2.0 to +5.0 ‰) and the value determined for the bulk silicate Earth (+3.5 to +4.0 ‰).

A systems analysis was performed in order to determine melt reservoirs for two locations of distinct geotectonic settings (ocean intra-plate (Tenerife, Canary Islands, Spain) and volcanic island arc (Kluchevskoy volcano, Kamchatka peninsula, Russia)). Reservoirs of varying primitive grade in a volcanic plumbing system were determined and the passage way of crystals could be retraced by forsterite and Li contents. Diffusion of Li was modeled to be 1.4–2.5 times faster than that of the Mg-Fe diffusion couple, which is significantly less than the diffusivity determined in experimental studies.

Chemically and isotopically zoned olivines from a continental intra-plate setting (Massif Central, France) were analyzed regarding their Li isotope composition along profiles from rim to core. Variations in the Mg-Fe and Li isotopic composition revealed a diffusive origin of the zoning, and Li gives insight into a second diffusive event, which remains hidden in Mg-Fe. Profiles of the first diffusive event were modeled with fixed time scales, based on Mg-Fe inter-diffusion, acquired by Oeser et al. (2015), for the residence time in a magma reservoir. The model again resulted in lower diffusion coefficients for Li diffusion in olivine, than those determined in experimental studies. A second, relatively short-lived, diffusive re-equilibration episode was assumed to be caused by the degassing of the magma and concomitant Li decrease in the melt with no effect on Mg-Fe distribution.

Zusammenfassung

Die Untersuchung der Fraktionierung stabiler Metallisotope zur Charakterisierung des Massenflusses bei hohen Temperaturen hat sich in den letzten Jahren als leistungsstarkes Instrument erwiesen. In dieser Studie wurden Li-Isotopenverhältnisse hochpräzise *in situ* an Referenzgläsern und natürlichen Olivinen durch induktiv gekoppelte Plasma-Multikollektor-Massenspektrometrie mit Femtosekunden-Laser Ablation (fs-LA-MC-ICP-MS) analysiert. Die Untersuchung der Li-Isotopenfraktionierung bei niedrigen Konzentrationen soll Aufschluss über Prozesse während der Evolution einer Schmelze geben.

Eine Serie von Referenzgläsern wurde *in situ* analysiert und mit Ergebnissen anderer Methoden (lösungsbasierte MC-ICP-MS, SIMS und TIMS) verglichen, um die entwickelte Messmethode zu testen. Diese methodische Untersuchung zeigte, dass die Anwendung eines relativ kühlen Plasmas (900 W) matrixabhängige Isotopeneffekte weitgehend unterdrückt. Eine Detektorkombination bestehend aus einem Ionenzähler zur Bestimmung von ^{6}Li und einem Faraday-Becher mit einem $10^{13}\,\Omega$-Verstärker für ^{7}Li wurde eingesetzt, um Konzentrationen im Bereich von 2 bis 10 µg/g präzise bestimmen zu können. Die analytische Unsicherheit für das Referenzglas T1-G betrug ~2 ‰ (2 σ) (δ^7Li$_{T1-G}$=1,6-2,4 ‰).

Die Fraktionierung von Li-Isotopen im Aufschluss- und Mineralmaßstab wurde in dieser Studie untersucht. Gesamtgesteins-Li-Isotopenanalysen aus einem Aufschluss über eine Länge von ~50 m im französischen Zentralmassiv zeigten, dass die Isotopenzusammensetzung in der Aufschlussskala zwischen +2,1 und +3,3 ± 2,0 ‰ variierte. Die gemessenen δ^7Li-Werte stimmen mit dem Bereich der weltweit nicht-alterierten vulkanischen Gesamtgesteine (+2,0 bis +5,0 ‰) und dem für die Silikaterde ermittelten Wert (+3,5 bis +4,0 ‰) überein.

Eine Systemanalyse wurde durchgeführt, um Schmelzreservoire für zwei geotektonische Settings (ozeanischer Intra-Plattenvulkanismus (Teneriffa, Kanarische Inseln, Spanien) und Vulkaninselbogen (Kluchevskoy-Vulkan, Halbinsel Kamtschatka, Russland)) zu identifizieren. Reservoire unterschiedlichen primitiven Grades in einem vulkanischen Magmenkammersystem wurden bestimmt und die Migrationspfade der Kristalle konnte durch Forsterit- und Li-Gehalte rekonstruiert werden. Die Diffusion von Li war 1,4- bis 2,5-mal schneller als die des Mg-Fe-Diffusionspaares, was signifikant unter der in experimentellen Studien ermittelten Diffusivität liegt.

Chemisch und isotopisch zonierte Olivine aus einem kontinentalen Intraplatten-Setting (Zentralmassif, Frankreich) wurden hinsichtlich ihrer Li-Isotopenzusammensetzung entlang von Rand-Kern-Profilen analysiert. Variationen in der Mg-Fe- und Li-Isotopenzusammensetzung zeigten, dass die Zonierung einen diffusiven Ursprung hat. In der Li-Zonierung zeigte sich, dass ein zweites Diffusionsereignis stattgefunden hat, das in der Mg-Fe-Zonierung verborgen bleibt. Die Profile des ersten Diffusionsereignisses wurden mit festen Zeitskalen modelliert, die auf der von Oeser et al. (2015) bestimmten Verweilzeit in einem Magmareservoir basieren. Das Modell ergab erneut niedrigere Diffusionskoeffizienten für die Li-Diffusion in Olivin, als in experimentellen Studien ermittelt. Die zweite, relativ kurzlebige Episode diffusiven Ausgleichs wurde durch die Entgasung des Magmas und die damit einhergehende Abnahme von Li in der Schmelze verursacht, was keine Auswirkung auf die Mg-Fe-Verteilung hatte.

Schlagwörter/Keywords

Table of Contents

Objectives and Background

Background

Zoning patterns in crystals of major and trace elements, and isotope compositions can be utilized to identify a series of processes such as magma mixing, magma transport, degassing and fractionation (Blundy and Shimizu, 1991; Umino and Horio, 1998; Ginibre et al., 2007). Diffusive isotope zoning caused by kinetic stable metal isotope fractionation is a promising tool not only to determine processes, but also timescales and the origin of diffusion in high-temperature environments. Established isotope systems such as Fe and Mg have been observed to fractionate up to 1 ‰ at magmatic temperatures for minerals and rocks from the Earth's mantle (Weyer and Ionov, 2007; Zhao et al., 2010; Pogge von Strandmann et al., 2011). With Mg-Fe inter-diffusion, attempts have been made to understand the complex evolution of magmatic systems (e.g. Sio et al., 2013; Collinet et al., 2014; Oeser et al., 2015; Oeser et al., 2018). The authors found that Fe and Mg diffusion is coupled, indicated by inversely correlated isotope profiles, and can help distinguish between pure diffusive processes and mixing between crystal growth and diffusion. Lithium isotope profiles have been measured by various authors in pyroxenes and olivines because they are the main carriers of Li in mafic rock compositions (e.g. Coogan et al., 2005; Beck et al., 2006; Jeffcoate et al., 2007), and plagioclases in more evolved systems (Giuffrida et al., 2018; Neukampf et al., 2019). The diffusivity of Li is assumed to be faster than that of Mg-Fe inter-diffusion in olivine, but still lower than the Li diffusion in pyroxene and feldspar (Dohmen et al., 2010). Hence, Li in olivine bears a high potential to reveal processes which are too fast to be displayed by Mg-Fe inter-diffusion.

Lithium is the lightest solid element on earth with the atomic number 3 and a density of 0.543 g/cm³. It is an alkali metal with first ionization energy of 5.39 eV and its common valence state is +1. Lithium is soluble and can be volatile. In many industries (e.g. ceramics, electronics, metallurgy), it has become a key raw material due to its physical and chemical properties (Tomascak et al., 2016 and references therein). Lithium is not only of interest for us in large amounts in an economic sense, but also in small amounts. Lithium is not utilized in the biogeochemical cycle which makes it a powerful tracer for

processes, where other isotope systems are influenced by microbial activity, e.g. continental weathering (Lemarchand et al., 2010; Pogge von Strandmann et al., 2016). During the last years, Li isotope studies have come into focus in order to understand fractionation and evolution processes of melts and magmatic bodies (Elliott et al., 2004; Tomascak, 2004; Tang et al., 2007). The two stable isotopes ^7Li and ^6Li have an abundance of 92.41% and 7.59%, respectively. Lithium isotope compositions are commonly displayed in the δ-notation:

$$\delta\,^7Li = \left[\frac{\left(\frac{^7Li}{^6Li}\right)_{sample}}{\left(\frac{^7Li}{^6Li}\right)_{standard}} - 1 \right] \times 1000\ (‰) \qquad \text{Eq. (B.1)}$$

The international reference material is L-SVEC (NIST SRM 8545) (Flesch et al., 1973), Li carbonate extracted from spodumene. As NIST L-SVEC is out of stock IRMM-16, which is slightly heavier than NIST L-SVEC ($\delta^7Li = 0.14 \pm 0.04$ ‰ (2 SE)) (Jeffcoate et al., 2004), is the accepted substitute. Due to the large relative mass difference of these two isotopes with ~17%, which is only surpassed by the isotope pair hydrogen and deuterium, isotope fractionation in nature can be quite large (Figure B.1). This is the reason for a large spread of isotopic variations of more than 50 ‰ between different reservoirs. Sea water is one of the heaviest reservoirs (δ^7Li=31 ‰ (You and Chan, 1996; James and Palmer, 2000; Millot et al., 2004a; Moriguti et al., 2004) in the Li geochemical cycle. Waters are isotopically heavy because ^7Li fractionates into the bond with lower coordination number (Wunder et al., 2011). The upper continental crust is one of the lightest bulk reservoirs with δ^7Li (average δ^7Li 0 ± 4 ‰) due to loss of ^7Li in the weathering process by leaching and the formation of secondary Li-bearing minerals (Teng et al., 2004). The isotopic composition of mantle rocks is very heterogeneous with δ^7Li-values between -9.7 ‰ and +9.6 ‰ due to metasomatic overprinting (e.g. Nishio et al., 2004; Tang et al., 2012; Ackerman et al., 2013; Su et al., 2016) and kinetic isotope fractionation (e.g. Lundstrom et al., 2005; Jeffcoate et al., 2007; Rudnick and Ionov, 2007; Ionov and Seitz, 2008). Ocean island basalts (OIB), arc basalts, and continental intraplate igneous rocks have overlapping δ^7Li of ~4 ‰ (e.g. Chan et al., 2002; Tomascak et al., 2002; Ryan and Kyle, 2004; Marks et al., 2007; Krienitz et al., 2012). The δ^7Li of fresh mid-ocean ridge basalts (MORB) varies between +2 and + 5 ‰ (Chan et al., 1992; Elliott et al., 2006; Tomascak et al., 2008)) whereas altered MORB have an elevated δ^7Li-value due to the formation of clays and zeolites and uptake of

heavy seawater (Chan and Edmond, 1988; Chan et al., 1992; Chan et al., 2002)). For the bulk silicate Earth (BSE) a δ^7Li-value of +3.5 to + 4 ‰ is suggested (Seitz et al., 2004; Jeffcoate et al., 2007; Magna et al., 2008; Pogge von Strandmann et al., 2011).
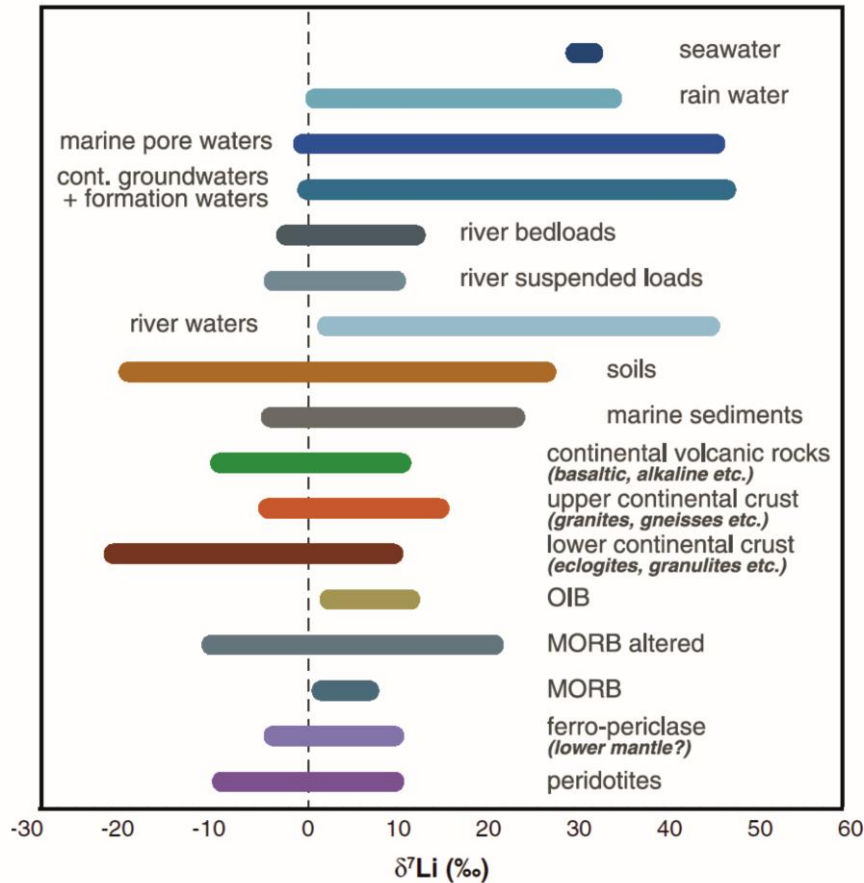
Figure B.1: Lithium isotopic composition of terrestrial and extra-terrestrial reservoirs (Fig. 1.2 from Tomascak et al. (2016), slightly modified).

In low temperature environments, equilibrium isotope fractionation can be quite large whereas at high temperatures, only little equilibrium isotope fractionation is induced, because the extent of equilibrium isotope fractionation decreases with the factor $1/T^2$ (Schauble, 2004). Hence, very limited isotope fractionation during the crystallization of a magma is found for Li isotopes (Tomascak et al., 1999a; Jeffcoate et al., 2007). Nevertheless, isotope fractionation at magmatic temperatures can be caused by kinetic isotope fractionation, such as diffusion, which causes intra-mineral isotope variations (e.g. Kasemann et al., 2005; Beck et al., 2006; Jeffcoate et al., 2007; Parkinson et al., 2007) and even such on the outcrop scale (Lundstrom et al., 2005; Teng et al., 2006).

Olivine is a nesosilicate with the chemical formula $(Mg,Fe)_2SiO_4$, with a complete solid solution between the end-members forsterite (Mg_2SiO_4) and fayalite (Fe_2SiO_4). It is the most abundant mineral in the Earth's upper mantle and is a major constituent of rocks

from ultramafic to mafic composition, with decreasing Mg/Fe ratio towards more evolved rock types (Deer et al., 2013). The structure consists of a tetrahedral site which is occupied by Si and two independent octahedral sites M1 and M2 (Figure B.2). Due to cation-cation repulsion across the shared edges of the polyhedra, the larger M2 site is distorted. The M1 site is smaller and less distorted. This can affect the crystal-chemical behavior of major and trace elements likewise (Zanetti et al., 2004). The major constituents Mg and Fe are abundant in their divalent state and have ionic radii in the octahedral coordination of 0.72 Å and 0.76 Å, respectively (Shannon, 1976). Lithium has a similar ionic radius of 0.76 Å (Shannon, 1976) in the octahedral coordination and can substitute for Mg and Fe in minerals. A trivalent cation in the M2 site and a monovalent cation, such as Li in the M1 site, yields the lowest energy pairing, and thus, is most stable (Purton et al., 1997). Lithium diffusion through the olivine structure can happen with two mechanisms. One is diffusion through vacancies in the octahedral site because only half of the octahedral sites in olivine are occupied, and the other is diffusion through interstitial sites in the crystal structure, as introduced by Dohmen et al. (2010) in the two species model for Li diffusion. The species that moves along the vacancy site is slower than the species that moves along an interstitial site. Nevertheless, the interstitial mechanism is supposedly only activated in highly oxidizing conditions and thus probably not activated in natural systems (Dohmen et al., 2010).
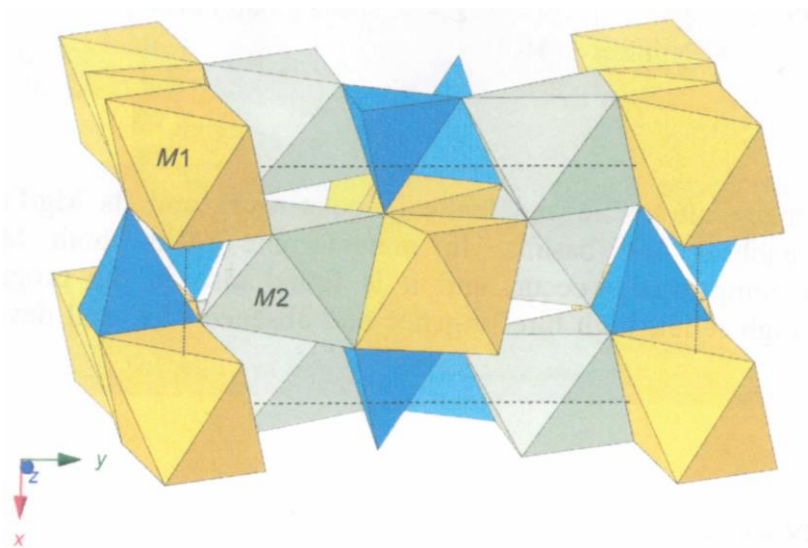
Figure B.2: Polyhedral model of the structure of olivine. The vertices of the polyhedral represent oxygens, and polyhedral structures M1 (yellow), M2 (green) and Si (blue). Crystal Maker image, Figure 2 from (Deer et al., 2013).

Objectives

Chapter 1 describes the development of a highly precise and highly spatially resolved analytical method for simultaneous *in situ* determination of Li isotopes, with femtosecond laser ablation-inductively coupled plasma-mass spectrometry (fs-LA-ICP-MS). This was necessary because no measurement technique was available, which determines Li isotopes at low concentrations both matrix-uninfluenced and with sufficient spatial resolution. The aim was to be able to measure Li isotope fractionation along 200-500 µm diffusion profiles through single crystals without applying an external matrix-correction. Low concentrations in olivine and pyroxene from 1 to 10 µg/g, can be measured with a specific detector combination of a secondary-electron multiplier and a highly resistive (10^{13} Ω) amplifier. This yields higher precision at low background signals, hence, improves the precision of the measurement. That is important at low concentrations, where low signal to background ratios are present.

In **Chapter 2** the calibration and setting up of Li bulk isotopic measurements, and column chromatographic separation of Li from the rock matrix is examined. The aim of this is to be able to compare the isotopic composition of a whole rock with the phenocryst-free matrix of a volcanic setting. It shall be deducted if isotopic variations can be observed on the outcrop scale in large magma bodies and not only on the mineral scale. In order to calibrate the separation process for an olivine matrix a hydrothermally formed olivine single crystal from Sapat (Kohistan, Pakistan) is investigated and compared to laser ablation data obtained with the analytical method from Chapter 1.

Chapter 3 aims at the determination of major, minor and trace element, and Li isotope profiles of olivine phenocrysts from two sample locations of different geotectonic environments (oceanic intra-plate and island-arc). The question if complex zoning patterns in Mg and Fe reveal more information on processes in olivines going through growth episodes in various magma chambers shall be answered. In order to define the behavior of Li diffusion relative to Mg-Fe diffusion the diffusivity is modeled with the measured profiles from natural olivines. The objective of this is to determine whether there is a coupling of the element diffusivities in natural systems and, in general, to gain a better understanding of diffusion mechanisms of minor and trace elements in natural olivine. In accordance with the modeled diffusivities, Li isotope profiles are modeled with an analytical approach applying the diffusivity determined in this chapter.

In **Chapter 4** diffusion modeling for Li chemical and isotope profiles is performed for olivines from continental intra-plate basanites, with a numerical two-step approach. The diffusion coefficients shall be modeled depending on established time scales and then compared to experimentally determined diffusion coefficients. A further question is, whether natural olivines reveal cooling histories in their Li chemical and isotope profiles, and if these processes are coupled to the diffusive events experienced by Mg and Fe. It is evaluated if Li isotopes can help gaining information on the evolution history in a magmatic system beyond the Mg-Fe isotope system due to the physical properties of Li.

Dissertation of Lena Steinmann

Chapter 1: *In situ* high-precision lithium isotope analyses at low concentration levels with femtosecond-LA-MC-ICP-MS

Chapter 1: *In situ* high-precision lithium isotope analyses at low concentration levels with femtosecond-LA-MC-ICP-MS

1.1 Abstract

In this study we have established a new method for *in situ* measurements of stable lithium (Li) isotope ratios at low Li concentration levels using UV-femtosecond laser ablation coupled with multi collector inductively coupled plasma mass spectrometer (MC-ICP-MS). Highly precise *in situ* determinations of Li isotope ratios are challenging due to low Li concentrations in most natural minerals and matrix-effects typically occurring during the ablation process and in the ion source. Here we demonstrate that matrix-dependent isotope effects in the plasma can be largely suppressed by operating the plasma at cool conditions (900 W) and a laser beam which is focused ~130 µm below the sample surface. At such conditions, precise and accurate measurements of δ^7Li with ~2 ‰ (2 σ) analytical uncertainty have been performed for various glass reference materials and olivine. Depending on the Li concentration of the investigated samples, detector combinations have been optimized in order to achieve the best precision. At Li concentrations ranging from 2 to 10 µg/g a combination of an ion counter for the determination of ^{6}Li and a faraday cup equipped with a 10^{13} Ω amplifier for ^{7}Li has yielded the best precisions. For Li concentrations >10 µg/g a faraday cup equipped with a 10^{13} Ω amplifier for ^{6}Li and a 10^{11} Ω amplifier for ^{7}Li, respectively are recommended. Measurements applying a 10^{13} Ω amplifier require a tau correction due to the slower signal response of the amplifier. The accuracy of the here established LA-MC-ICP-MS method was tested by comparing the results obtained for reference glasses that have been analyzed both, *in situ* and with solution MC-ICP-MS (or other conventional methods, previously applied in other studies), the results are overall in good agreement. The applicability for a zoned olivine phenocryst from Massif Central volcanic region has been tested successfully.

Chapter 1: *In situ* high-precision lithium isotope analyses at low concentration levels with femtosecond-LA-MC-ICP-MS

1.2 Introduction

Metal isotope fractionation at high temperatures is mainly caused by kinetic isotope effects driven by e.g. diffusion (e.g. Richter et al., 2009 and references therein). Diffusion patterns in magmatic crystals are often visible as small-scale chemical and isotopic heterogeneities and isotopic zoning.(Sio et al., 2013; Oeser et al., 2015) Lithium (Li) is of special interest because in many geological materials it diffuses faster than Mg and Fe which have been frequently used to determine cooling rates by modeling diffusion patterns of magmatic crystals in olivine and clinopyroxene (Sio et al., 2013; Oeser et al., 2015). The two stable Li isotopes have a relative mass difference of ~17%, and ^{6}Li diffuses ~5% faster than ^{7}Li (Richter et al., 2009; Dohmen et al., 2010). Thus, potential intra-mineral and inter-mineral variations in the Li isotopic composition generated by diffusion are expected − and have been shown − to be large (Jeffcoate et al., 2007; Pogge von Strandmann et al., 2011). Lithium is present in volcanic rocks with a wide range of abundances, covering 2-13 µg/g for mid-ocean ridge basalts (MORB) (Chan et al., 1992; Elliott et al., 2006), 3-15 µg/g in ocean island basalts (OIB) from different localities (Chan and Frey, 2003; Vlastélic et al., 2009), and 2-140 µg/g in continental igneous rocks with elevated concentrations in alkaline basalts (Liu et al., 2013; Abdelfadil et al., 2014; Ackerman et al., 2015). Olivine is the main carrier of Li with partition coefficients of $D^{ol/cpx}$=1.5-2.02 (Seitz and Woodland, 2000), and behaves moderately incompatible during mantle melting with $D^{ol/melt}$=0.21-0.56 (Taura et al., 1998). A partition coefficient of 1 implies the equal distribution of an element between two phases (e.g. mineral and melt), a partition coefficient <1 implies the incompatibility of an element in the first mentioned phase and vice versa a partition coefficient >1 implies that an element is compatible. The isotopic composition of these rocks shows bulk rock values for δ^7Li between +2.0 ‰ and +4.8 ‰ for MORB (Tomascak et al., 2008), and between +3.0 ‰ and +4.8 ‰ in OIBs (Tomascak et al., 1999b), which is very similar to δ^7Li values of mantle peridotites which range between +3.4 ‰ to +4.5 ‰(Seitz et al., 2004).

In high temperature environments equilibrium Li isotope fractionation, e.g. during crystallization of minerals from a magma, is small (Tomascak et al., 1999b; Jeffcoate et al., 2007). However, kinetic isotope fractionation at magmatic temperatures has been reported to cause large Li isotope variations visible on the bulk rock as well as on the

Chapter 1: *In situ* high-precision lithium isotope analyses at low concentration levels with femtosecond-LA-MC-ICP-MS

mineral scale. For example, δ^7Li varies from +7.6 to -19.9 ‰ due to diffusion-driven fractionation from a pegmatite intrusion into the country rock (Teng et al., 2006). Diffusion-driven isotopic disequilibrium between basaltic melt and xenoliths or pheno- and xenocrysts, respectively, has been shown to result in Li isotope fractionation on the order of 10 to 20‰ (Ionov and Seitz, 2008; Weyer and Seitz, 2012). On the grain scale variations from rim to core have been reported for clinopyroxenes, olivines and orthopyroxenes and are meant to be caused by diffusional uptake of Li into the crystals (Rudnick et al., 2004; Parkinson et al., 2007). Jeffcoate et al. (2007) found isotopic variations of up to 40 ‰ within a single orthopyroxene crystal due to diffusion. According to the high diffusivity of Li, individual crystals, such as phenocrysts or xenolith minerals, frequently show chemical and isotopic zoning which bear the potential to be used as a powerful diffusion-based chronometer for high-temperature processes, also known as geo-speedometry. Such a method has been successfully used to reconstruct the evolution history of magmas (Jeffcoate et al., 2007).

As the grain size of olivines and clinopyroxenes in volcanic rocks are typically in a range of 100-2000 µm and length scales of chemical zonations in these crystals are commonly <200µm, spatially resolved analytical techniques are required, in order to resolve chemical and isotopic zoning. Secondary ion mass spectrometry (SIMS) allows for spatially highly-resolved Li isotope analyses (Kasemann et al., 2005), but commonly suffers from matrix-effects, illustrated by Bell et al. (2009) during the analyses of olivine. As matrix matching is difficult while measuring diffusion profiles in zoned minerals, a method for high precision and matrix-independent Li isotope analyses is required. *In situ* analyses have been performed with nanosecond laser ablation coupled to MC-ICP-MS, but these studies applied laser spot sizes of >150 µm (Xu et al., 2013; Lin et al., 2017), which is unsuitable for the measurement of diffusion profiles as spot sizes <50 µm are required in order to resolve Li diffusion patterns.

Laser ablation-induced isotopic fractionation, an aerosol particle size effect, can occur when laser ablation MC-ICP-MS is applied (Jackson and Günther, 2003; Horn and von Blanckenburg, 2007; Horn, 2008; Lazarov and Horn, 2015). The first source of fractionation is the ablation process. Even though a thermal ablation process, femtosecond LA is, in contrast to nanosecond LA, able to limit these thermal effects to nm-sized areas surrounding the ablation crater (Hergenröder, 2006; Lazarov and

Chapter 1: *In situ* high-precision lithium isotope analyses at low concentration levels with femtosecond-LA-MC-ICP-MS

Horn, 2015), which is due to the limited loss of energy through thermal diffusion at femtosecond time scales. Therefore, laser-induced chemical and isotopic fractionation is minimized in the ablation process resulting in the possibility to perform largely matrix-independent analyses (Poitrasson et al., 2003; Fernández et al., 2007; Horn and von Blanckenburg, 2007). Though the matrix-independence of the ablation process can be achieved with a femtosecond laser ablation system another source of mass discrimination and thus fractionation is the plasma source of the mass spectrometer (Vanhaecke et al., 1993). Plasma load effects have been discussed, resulting in the enhancement of space charge effects in the interface region of the mass spectrometer (Kroslakova and Günther, 2007). Due to low Li concentrations in most natural minerals a proportionally big amount of matrix elements is present in the sample and thus ablated and introduced by the laser ablation process into the plasma. As Li is a light element compared to the matrix elements, a problem rising with this matrix-analyte ratio is the behavior of the ionized elements in the plasma. In the zone model light isotopes are pushed to the outer zones of the plasma due to density differences causing an additional mass bias in the detected ions (Vanhaecke et al., 1993).

The low concentrations of Li in minerals of magmatic origin such as pyroxenes and olivines covering a concentration range from 0.5 to 20 µg/g are analytically challenging. The abundance of Li isotopes is 92.41% for ^{7}Li and 7.56% for ^{6}Li which accounts for the imperative need of a precise measurement despite the fact that only weak signals detected by the MC-ICP-MS. The very critical part is the reliable detection of ^{6}Li at very low concentrations. For this purpose, standard faraday cup configurations with $10^{11}\,\Omega$ amplifiers are unsuitable. In this study a combination of different detectors, including ion counters and faraday cups with $10^{13}\,\Omega$ amplifiers have been tested for their achievable precision at different intensity levels. In a recent study Lloyd et al. (2018) applied $10^{13}\,\Omega$ amplifiers for the detection of B signals down to $1*10^{-13}\,A$ (10 mV on a $10^{11}\,\Omega$ amplifier). The lower detection limit of the detectors is determined by the noise limit of the amplifiers (Bouman et al., 2015). Furthermore, low background levels are essential for a precise and accurate measurement of Li isotope ratios in magmatic minerals, especially when applying ion counters.

In this study, we have developed a method to determine Li isotope ratios *in situ* using UV-femtosecond laser ablation coupled to MC-ICP-MS and to determine the ideal

Chapter 1: *In situ* **high-precision lithium isotope analyses at low concentration levels with femtosecond-LA-MC-ICP-MS**

detector combination for distinct Li concentration levels at minimal standard errors and consequently best precisions achievable to minimize the influence of background signals. The herein developed *in situ* analysis technique was applied to measure the Li isotopic compositions of silicate reference glasses and to show a diffusion profile in a zoned olivine crystal.

1.3   Reference materials and samples

The investigated samples comprise silicate reference glasses with low Li concentrations from 3 to 28.6 µg/g Li. The basaltic USGS reference glasses BIR-1G, BHVO-2G and BCR-2G as well as the MPI-DING glasses KL2-G and ML3B-G (basalts), StHs6/80-G (andesite), ATHO-G (rhyolite), T1-G (diorite) and GOR132-G and GOR128-G (komatiites) were analyzed by femtosecond laser ablation MC-ICP-MS. The concentrations of Li and the δ^7Li-values of the analyzed samples are displayed in Table 1.1.

Table 1.1: Lithium concentrations and isotopic composition of MPI DING and USGS reference materials (Jochum et al., 2006; Jochum and Stoll, 2008).

		Li (µg/g)	δ^7Li (‰)
MPI-DING	KL2-G	5.2	4.1
	ML3B-G	4.4	4.4
	GOR128-G	9.7	14.4
	GOR132-G	8.7	8.9
	ATHO-G	28.0	17.1
	T1-G	19.8	2.1
	StHs6/80-G	20.5	3.6
USGS	BIR-1G	3.0	5.4
	BCR-2G	9.0	4.5
	BHVO-2G	4.4	6.8*

* this value is the calculated mean δ^7Li from several studies (Kasemann et al., 2005; Xu et al., 2013)

As an example for the applicability to natural samples an olivine from Banne D'Ordanche, Massif Central, France with a zoning in Mg# from 80 to 89 was

Dissertation of Lena Steinmann

Chapter 1: *In situ* **high-precision lithium isotope analyses at low concentration levels with femtosecond-LA-MC-ICP-MS**

investigated. Mg# is calculated as follows: Mg# = 100 x [MgO]/[MgO + FeO], where MgO and FeO are concentrations in mol.%. This olivine originates from a basanite that has been sampled at the north-west slope of a former strato-volcano which forms the summit of the Banne D'Ordanche (N45°36.671', E02°46.355') from an eruption ~710,000 years ago (Richet, 2003).

1.4   Experimental

1.4.1   Laser ablation system

In situ Li isotope determinations were performed using a MC-ICP-MS (Thermo-Finnigan Neptune Plus) coupled to a Spectra-Physics Solstice femtosecond laser based ablation system at the Leibniz Universität Hannover, Germany. The Solstice system uses a low energy <100 femtosecond Ti:sapphire seed laser (Spectra Physics MaiTai) and a high energy Nd:YLF pump laser (Spectra Physics Empower-15) pumping at a repetition rate of 500 Hz. In the Spectra Physics Solstice regenerative amplifier with Chirped Pulse Amplification in a Ti:sapphire crystal working at a fundamental wavelength of 775 nm infrared laser pulses are produced. These pulses have energies up to 3.5 mJ/pulse. The output beam is frequency-quadrupled in three BBO crystals (barium beta borate) to achieve a conversion from infrared to UV with a wavelength of 194 nm. The pulse width of the amplifier output is about 100 fs. The laser beam is focused onto the sample surface via a modified New Wave (ESI) stage with an optical microscope (Horn et al., 2006; Horn and von Blanckenburg, 2007). Thermal effects can be caused by the laser beam interacting with the sample surface. These effects can be melting of the ablation crater rim and thus forming larger particles which are transported to the plasma and cannot be fully ionized by the plasma (Jackson and Günther, 2003; Horn and von Blanckenburg, 2007). To avoid these thermal effects and the fracturing of the sample surface the focal point of the laser beam plays an important role. The laser should be focused ~130 µm below the sample surface in order to be able to measure with good accuracy (Schuessler and Von Blanckenburg, 2014). The spot size on the bracketing standard GOR132-G is ~26 µm.

The ablation cell has a volume of 35 cm³ suitable of carrying a thin section and two ½ inch mounts for standard reference materials. The sample aerosol is transported to the

Chapter 1: *In situ* high-precision lithium isotope analyses at low concentration levels with femtosecond-LA-MC-ICP-MS

mass spectrometer by a mixture of Argon and Helium gas. A mixing tube for signal smoothing having a volume of 50 cm³ was implemented directly behind the ablation cell and prior to the addition of the make-up gas Ar to enhance the signal stability (Figure 1.1). This is required when using the slow 10^{13} Ω amplifiers to avoid high tau corrections during analysis and the need of disabling the protection circuit of the ion counting devices in the mass spectrometer.
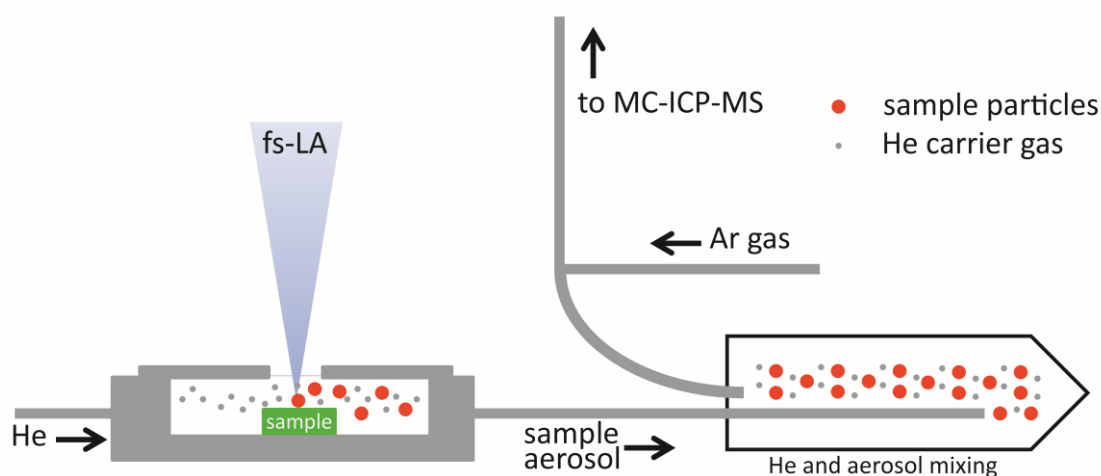
Figure 1.1: Sketch of the ablation cell and homogenization device set-up.

1.4.2 Laser ablation MC-ICP-MS

In the Neptune Plus MC-ICP-MS relatively cool plasma conditions were used to measure Li isotopes which means a decreased RF power of 900 W and an elevated sample gas flow were applied. A sample H cone and a skimmer X cone were used. Overall, the applied conditions decrease the ionization of matrix elements which in turn decreases the degree of space charge effects (see Results and Discussion). Measurement conditions are summarized in the appendix (Table A.1.1). *In situ* Li isotope ratio measurements were performed in static mode at low mass resolution because potential molecular interferences such as doubly charged ^{14}N on mass 7 or doubly charged ^{12}C on mass 6 can be resolved even in low mass resolution mode. The detector array of the Neptune Plus comprises 10 Faraday detectors and three secondary ion multipliers (SEM). Due to the relative mass difference of ^{6}Li and ^{7}Li of 17% it is only possible to measure these two isotopes simultaneously and no further isotopes of other elements for mass bias monitoring can be measured. ^{6}Li is measured on the low mass side of the

Chapter 1: *In situ* high-precision lithium isotope analyses at low concentration levels with femtosecond-LA-MC-ICP-MS

center cup in the non-moveable outermost detector (L5 faraday detector or SEM) whereas ^{7}Li is detected on the high side (H4 faraday detector) of the center cup. Lithium is measured under dry plasma conditions since the addition of water would raise the background on Li drastically. Measuring with wet plasma conditions versus dry plasma conditions yielded a background which was five times higher than during a dry measurement (300 cps vs. 1800 cps on ^{6}Li measured with a SEM) and yielding an even lower signal (128 k cps vs. 110 k cps on ^{6}Li measured with a SEM). We suspect that the wet plasma conditions raise the background due to either mobilization of contaminations in nebulizer, spray chamber etc. or due to higher oxide rates caused by the O ions from the H_2O in the system.

All measurements were performed using standard-sample-bracketing with the komatiitic MPI DING reference glass GOR132-G as bracketing standard with signal intensity-matching between sample and standard of ±10 %. GOR132-G is well-characterized and shows only minor heterogeneities in its Li isotopic composition when compared to the other reference glasses analyzed in this study (Jochum et al., 2011). Measurements of glasses were performed in raster ablation mode with a scan speed of 20 µm/s, the profile in olivine was measured in line ablation mode with lines arranged perpendicular to the crystal rim. Individual measurements consist of 180 cycles with an integration time of 1.049 s. The first ~35 cycles were used for background correction measuring only the gas blank without a laser ablation signal. This was followed by ~130 cycles of sample ablation. Variable repetition rates were used to enlarge the range of achieved signal intensities in order to compare the different detector combinations given below. All reference glasses were measured at least 10 times in at least 2 sessions for each reference glass. δ^7Li-values are reported relative to GOR132-G following Eq. (1.1):

$$\delta\ ^7Li = \left[\frac{\left(\frac{^7Li}{^6Li}\right)_{sample}}{\left(\frac{^7Li}{^6Li}\right)_{GOR132-G}} - 1 \right] \times 1000 \qquad \text{Eq. (1.1)}$$

In situ δ^7Li of all samples was recalculated relative to the commonly used Li isotope standard IRMM-016 with Eq. (1.2). The isotope ratio of IRMM-016 is identical to that of NIST-LSVEC 8545 (Qi et al., 1997).

Chapter 1: *In situ* high-precision lithium isotope analyses at low concentration levels with femtosecond-LA-MC-ICP-MS

$$\delta^7Li_{\frac{sample}{IRMM-016}} = \delta^7Li_{\frac{sample}{GOR132-G}} + \delta^7Li_{\frac{GOR132-G}{IRMM-016}} \qquad \text{Eq. (1.2)}$$

where $\delta^7Li_{sample/GOR132-G}$ is the *in situ* determined δ-value of the sample relative to GOR132-G, and $\delta^7Li_{GOR132-G/IRMM-016}$ is the δ-value of GOR132-G relative to IRMM-016 determined by e.g. Jochum et al. (2006).

Depending on the Li concentration, the laser repetition rate was adjusted which influenced the ablated volume and thereby the signal intensity. However, a higher ablation rate generates deeper craters, resulting in decreasing signal intensities with depth and decreasing precision of the single measurement. For signal intensity matching purposes the repetition rate was adjusted in dependence of the Li concentrations of the sample and the detector combination used. Usually, repetition rates of 8 to 25Hz were used. For very low concentrations (~1 µg/g) repetition rates of up to 100 Hz were applied on glass and olivine samples yielding precisions better than 2‰ (2 RSE), in most cases. Available detectors with varying dynamic measurement ranges are faraday cups equipped with 10^{11} Ω amplifiers ($5*10^{-14}$ A – $5*10^{-10}$ A), faraday cups with 10^{13} Ω amplifiers ($2*10^{-14}$ A – $5*10^{-13}$ A), and secondary electron multipliers (SEM, up to 1 M cps).(Lloyd et al., 2018) SEMs can be applied for the measurement of up to 1 million counts per seconds (cps), in theory, which is equivalent to a ion signal of $1.6*10^{-13}$ A (corresponding to 16 mV on a Faraday detector coupled to a 10^{11} Ω amplifier). The detectability is limited by the dark count rate which is usually in the range of 2-3 counts per minute (cpm). However, precision at low counting rates is largely limited by counting statistics. Lower limits of faraday amplifiers are defined by the amplifier noise and their ideal signal range in a variety of combinations will be evaluated here. Lloyd et al. (2018) determined the baseline variance for a 10^{13} Ω amplifier and a 10^{11} Ω amplifier with 0.9 µV ($9*10^{-18}$ A) and 4.2 µV ($4.2*10^{-17}$ A), respectively. Li isotope ratio measurements have been performed with three different detector combinations depending on Li concentrations and signal intensities (Table 1.2).

Chapter 1: *In situ* **high-precision lithium isotope analyses at low concentration levels with femtosecond-LA-MC-ICP-MS**

Table 1.2: Detector combinations for the measurement of ^{7}Li and ^{6}Li

	^{7}Li	^{6}Li
FC11-FC13	Faraday cup + 10^{11} Ω amplifier	Faraday cup + 10^{13} Ω amplifier
FC11-SEM	Faraday cup + 10^{11} Ω amplifier	SEM
FC13-SEM	Faraday cup + 10^{13} Ω amplifier	SEM

The higher resistance of an amplifier results in a slower signal response which is defined by a decay value. Signals detected on faraday detectors with 10^{13} Ω amplifiers have to be corrected for the disparities in the decay time (tau = decay constant). The tau-correction accounts for the signal time delay of the amplifier and it has to be applied when the detector assembly contains different detector or amplifier types. For this purpose the tau-factor which is individual to each amplifier has to be determined (Craig et al., 2017). The tau-correction is performed according to Kimura et al. (2016).

1.4.3   Solution nebulization MC-ICP-MS

Small amounts of the reference glasses were digested in a mixture of 6 M HNO$_3$ and conc. HF on a hot plate (180 °C) for 2-3 days. Lithium was purified applying an ion exchange chromatography with a cation exchange resin according to Seitz et al. (2004). The sample was diluted in a mixture of methanol and HNO$_3$ for column separation and eluted with an acid volume of 10 ml of a mixture of the same acids. Matrix-purified samples were measured with a Neptune MC-ICP-MS at the Goethe-Universität Frankfurt. Before introduced into the plasma the sample aerosol was dried at 160°C using a CetacAridus® membrane desolvation unit and a pneumatic nebulizer combination fitted with a PFA spray chamber. Sample analysis was carried out sequentially by applying sample-standard-bracketing like for LA measurements with the NIST L-SVEC standard (Flesch et al., 1973). Isotope compositions are expressed as ‰ deviations from the L-SVEC standard, according to the δ-notation given above. Internal precision is typically between 0.2 and 0.5 ‰ (2 SE).

Chapter 1: *In situ* high-precision lithium isotope analyses at low concentration levels with femtosecond-LA-MC-ICP-MS

1.5 Results and discussion

1.5.1 Effect of detector combinations on the precision of Li isotope measurements

Two main factors are limiting the achievable precision of a given detector combination when measuring small ion beam currents. These are the counting statistical error and the electrical noise of the amplifiers/ ion counters (Bouman et al., 2015). The influence of the background variation has been investigated here as well. For all detector combinations a theoretical, purely counting error (CE) can be calculated over a range of ion beam intensities (Figure 1.3 (a), black line). The uncertainty resulting from counting statistics independent of the detector type applied and the precision of a measurement can never get better than the CE. It decreases with increasing signal intensity which means with an increased number of counts. The error for one isotope (^{7}Li or ^{6}Li) and for the ^{7}Li/^{6}Li isotope ratio can thus be calculated with Eq. (1.3) and Eq. (1.4), respectively.

$$CE = \sqrt{counted\ events} \qquad\qquad \text{Eq. (1.3)}$$

$$CE_{\frac{^7Li}{^6Li}} = \sqrt{\left(\frac{CE_{\,^7Li}}{counted\ events}\right)^2 + \left(\frac{CE_{\,^6Li}}{counted\ events}\right)^2} \qquad \text{Eq. (1.4)}$$

The noise level, which is induced by the electric resistance of the amplifiers coupled to faraday cups, limits the precision and also the lowest signal/noise ratio which can still be measured. This type of error is directly linked to the detector type and also to the amplifier type which is applied (Koornneef et al., 2014; Lloyd et al., 2018). The measured noise levels coincide with the theoretical electrical Johnson-Nyquist noise of the resistors. The noise variation of the amplifiers (Figure 1.2 (a)) was determined by measuring the detector noise for 10 blocks of 120 cycles with a cycle integration time of 1.049 s. The duration of a measurement of ~120 s is appropriate for a laser ablation analysis. The integration time of 1.049 s is different to the standard specification for $10^{13}\,\Omega$ amplifiers of 4.149 s but no difference in noise variation was determined between the integration times. Ion counters have practically no noise, the dark noise determined for the applied ion counter is ~2-3 cpm, in our specific case the dark noise

Chapter 1: *In situ* high-precision lithium isotope analyses at low concentration levels with femtosecond-LA-MC-ICP-MS

was determined to be 2.24 cpm and measured over a period of 20 minutes. In practical application the analytical setup is contaminated with a background signal inherent to the system. Background signals occur due to contaminations in the analytical setup. These contaminations can originate from the gas flows, the parts which are placed in the interface (torch, injector, cones) and the tube system connecting the laser ablation system to the MC-ICP-MS. To achieve low background levels it is crucial that these parts are free of Li contaminations and it has been found that the skimmer cone is the most sensitive part in the system to accumulate these Li contaminations. For this reason we suggest to apply an exclusive set of cones only used for low level Li laser ablation measurements. This influence of the background has to be considered as well, when calculating the minimum error of the measurements. The approach for this was similar to the inclusion of the detector noise, the background has been measured for 140 cycles with an integration time of 1.049 s. Background noise and detector noise cannot be measured separately, for that reason the values of the background noise also contain the detector noise values. The measured background standard errors show no difference to the amplifier noise standard errors mentioned above (Figure 1.2 (b)) and will thus be considered as an overall noise and background standard error.

In Figure 1.3 (a) the counting statistical error (black line) and the baseline uncertainties (green, red and blue lines) caused by the noise of the detector combination are displayed. The calculated data shows that precision in the low signal range (up to 20 mV, $2*10^{-13}$ A) is limited to the noise of the detector combination and for higher signals (from 80 mV, $8*10^{-13}$ A) the precision is determined by counting statistics as the signal to noise ratio is increasing. The baseline uncertainty for a 10 mV signal on ^{7}Li (~ 0.8 mV on ^{6}Li) for FC13-SEM and FC11-FC13 is 0.1 ‰ and 1.3 ‰, respectively. In Figure 1.3 (b)-(d) the propagated errors for each detector combination are compared to the measured internal precisions of the ^{7}Li/^{6}Li ratio. For this purpose the above mentioned reference glasses have been measured in more than 20 measurement sessions throughout eight months, precisions at the same signal intensity have been averaged. For FC11-FC13 the calculated error curve coincides very well with the measured curve. For FC11-SEM and FC13-SEM the calculated error is ~50 ppm and ~55 ppm lower, respectively. A reason for this might be inherent to the SEM. When using SEM based detector combinations the precision is also influenced by the dead time of the ion

Chapter 1: *In situ* high-precision lithium isotope analyses at low concentration levels with femtosecond-LA-MC-ICP-MS
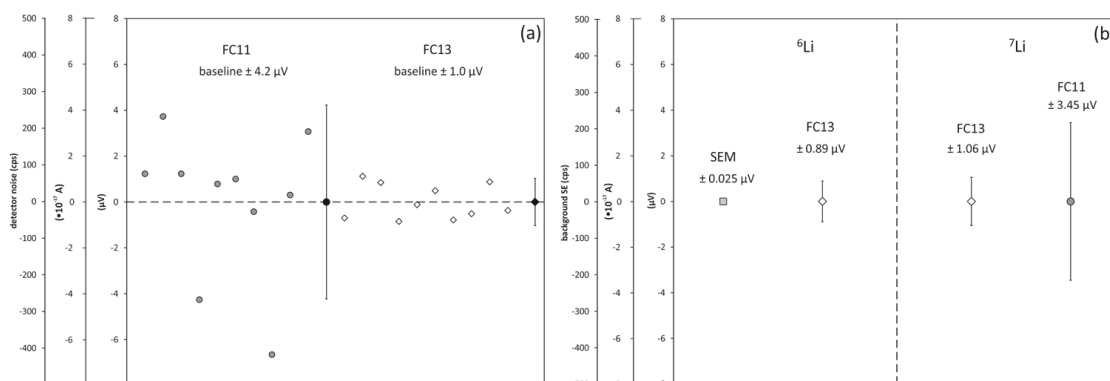
Figure 1.2: (a) Baseline noise (standard error) of 10^{11} and 10^{13} Ω amplifiers (b) background noise (standard error) for SEM and 10^{13} Ω amplifier and 10^{11} and 10^{13} Ω amplifiers deployed for measurement of ^{6}Li and ^{7}Li, respectively.
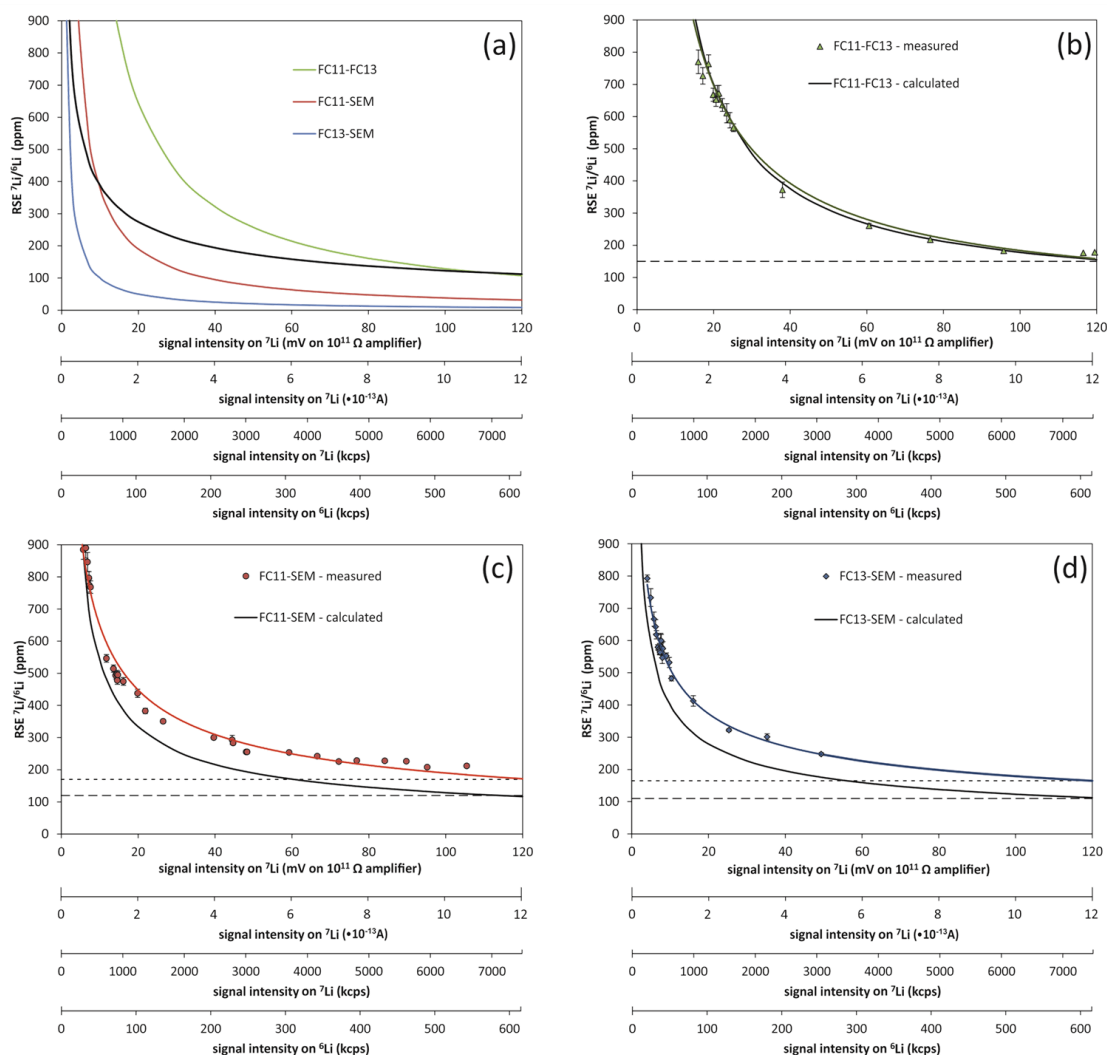
Figure 1.3: (a) Calculated errors (relative standard errors, RSE) for counting statistics and detector noise for the detector combinations FC11-FC13, FC11-SEM and FC13-SEM (b) – (d) Precisions (RSE) of individual analyses of reference glasses for single measurements over a period of 8 months for three detector combinations displayed with error propagation of counting statistics and detector noise for each detector combination ((b) FC11-FC13 (c) FC11-SEM (d) FC13-SEM, dashed lines = calculated error boundaries, error can never become lower than this, dotted lines = lowest measured error), calculations applied for error calculation can be found in Table A.1.2 in the appendix.

19

Chapter 1: *In situ* high-precision lithium isotope analyses at low concentration levels with femtosecond-LA-MC-ICP-MS

counter, its non-linearity behavior, the inter-calibration of SEMs and Faraday cups and the drift in efficiency of the SEM (Koornneef et al., 2014).
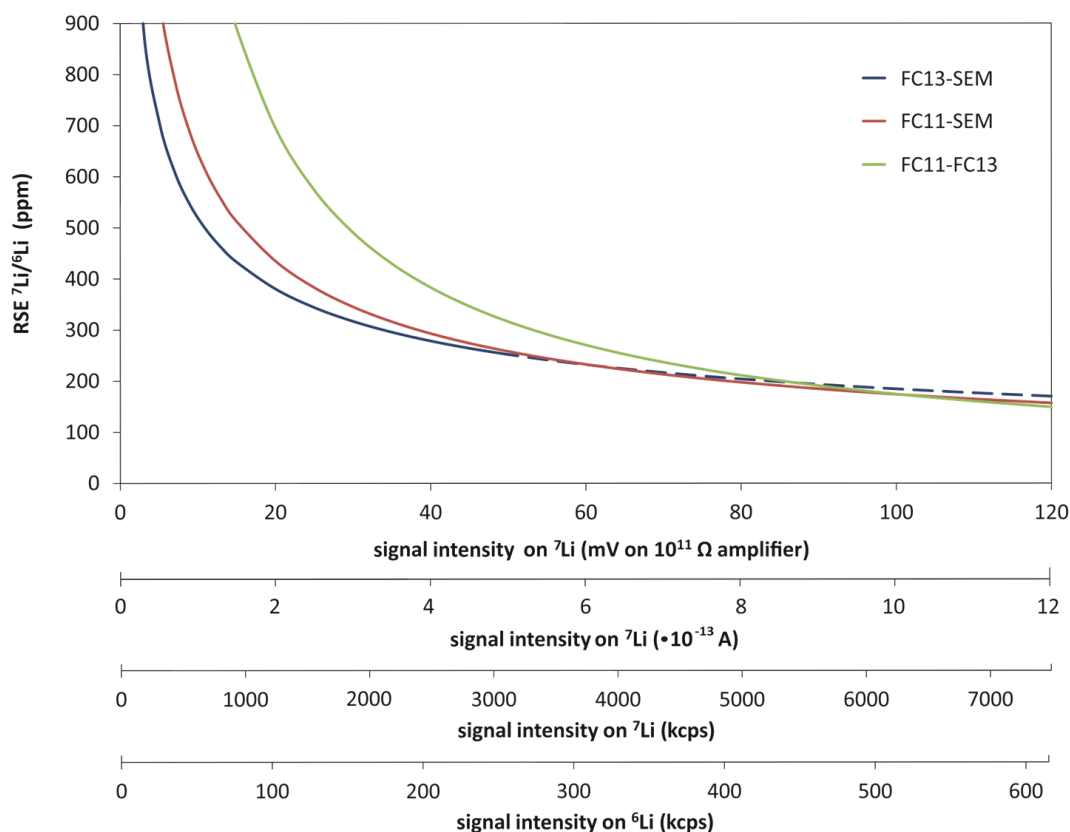
Figure 1.4: Curve progression of achievable precisions modeled from analyses of single measurements with modeled formulas as follows: y=9148•x$^{-0.86}$ (FC11-FC13), y=2400•x$^{-0.52}$ (FC11-SEM), y=1465•x$^{-0.45}$ (FC13-SEM), the regression for FC11-SEM is only applicable up to 90 mV (9*10^{-13} A).

In Figure 1.4 the internal precision of all individual measurements of the investigated MPI-DING reference glasses, analyzed with different detector combinations, as given in Table 1.2, have been combined. At intensities above ~80 mV on ^{7}Li (corresponding to about 7.7 mV on ^{6}Li) FC11-FC13 permits the lowest relative standard errors (RSE), i.e. the highest precision. For the intensity interval from about 50 mV to 80 mV FC11-SEM yields the best precisions and for signal intensities below 50 mV FC13-SEM yields the most precise results. Nevertheless, FC11-FC13 and FC11-SEM yield similarly high precisions in the range of 80 mV and 120 mV (upper limit investigated here) and FC13-SEM and FC11-SEM give similar precisions between 15 mV and 50 mV. Theoretically, FC11-SEM is not needed if the mass spectrometer is equipped with a 10^{13} Ω amplifier

Chapter 1: *In situ* high-precision lithium isotope analyses at low concentration levels with femtosecond-LA-MC-ICP-MS

as the dynamic range of these amplifiers reaches until 500 mV. For signals lower than $5*10^{-14}$ A (5 mV) the noise of the 10^{13} Ω amplifier exceeds the error caused by counting statistics and thus in this signal range SEMs have to be applied (Koornneef et al., 2014). The dead time (15 ns) of the SEM begins to play a role for signal intensities above 100 000 cps which is the dead time base frequency. Both factors are inherent to the SEM and have been determined experimentally by measuring three different concentrations of an isotope ratio and fitting the dead time equation to obtain the same ratio for all dilutions.

For the detector combinations involving 10^{13} Ω amplifier the time delay has to be considered by applying the tau correction as mentioned above. The correction of the time delay of the 10^{13} Ω amplifier in respect to a 10^{11} Ω amplifier or a SEM is usually ruled out by a long integration time of ~4.196 s or ~8.392 s and a stable signal in solution measurements. For laser ablation measurements signals are more unstable und thus time delays between the signal onsets of two detectors are more pronounced. A more stable signal can be achieved by homogenizing the gas flow by adding a mixing cell to the analytical setup as described above. The relative standard error of the signal has been reduced for ^{7}Li/^{6}Li from 467 ppm to 332 ppm at ~60 mV ($6*10^{-12}$ A) which corresponds to an improvement of 28.8 %. The precision improvement was tested for a measurement of 60 cycles with an integration time of 2.1 s. Hence, the precision with the mixing cell is always better than without it. Additionally, the stable signal allows the use of shorter cycle time when using 10^{13} Ω amplifiers. The smoothed signal also generates a smaller difference in the signal between two integration intervals and thus the tau correction is less effective but still necessary to balance for sudden signal variations (Figure 1.5 (a)). For the calculation of δ^7Li the tau correction only yields improvements within the analytical error.

Chapter 1: *In situ* high-precision lithium isotope analyses at low concentration levels with femtosecond-LA-MC-ICP-MS
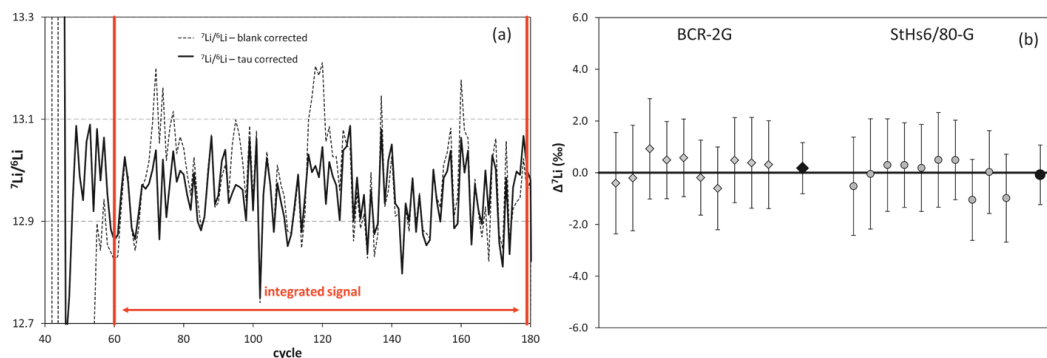
**Figure 1.5: (a) ^{7}Li/^{6}Li signal throughout a measurement (dashed line = only blank corrected, solid line = blank and tau corrected) (b) difference in tau corrected and non-tau corrected δ^7Li values ($\Delta\delta^7$Li=δ^7Li$_{tau\text{-}corrected}$-δ^7Li$_{non\ tau\text{-}corrected}$) for reference materials BCR-2G and StHs6/80-G, error bars show 2 σ of a measurement, black symbols are mean values of these values, error bars are 2 SD for the reference measurements with n=10.**

1.5.2 Effect of cool plasma conditions on accuracy

Large differences in major matrix element composition between bracketing standard and sample may result in a shift of the measured δ-values. We have observed such effects for the major element oxides SiO_2 and MgO (Figure 1.6). The radio frequency (RF) power of the plasma has been found to have a crucial influence on the accuracy of the measurements. At a RF power of 1080 W a clear correlation between Δ^7Li = δ^7Li$_{measured}$-δ^7Li$_{published}$ and the difference in the major element concentrations SiO_2 and MgO between the sample and the standard is observed (Figure 1.6 (a) and (b)). Matrix-effects in the plasma can occur because of the plasma zone model which indicates a zone of maximal density in the plasma for every nuclide depending on its mass. This zone of maximal density can be influenced by the elements in the matrix which is introduced into the plasma (Vanhaecke et al., 1993). Besides matrix effects space charge effects lead to a mass bias in the plasma by light isotopes being rejected more from the center ion beam than the heavy ones, these two effects cannot be distinguished analytically. Both effects would lead to the rejection of light isotopes depending on the matrix analyzed. Another effect influencing the mass discrimination is the so called "nozzle separation effect" which also causes light ions to be pushed to the outer part of the plasma by the down-pumping of light ions in the area between the plasma torch and the skimmer cone. This effect cannot be distinguished from space charge effects on the detector side (Heumann et al., 1998). However, all these effects should result in δ-values, which are too heavy which is opposite to our observations. Consequently, neither the extraction mechanism nor the separation mechanism within the plasma, but

Chapter 1: *In situ* high-precision lithium isotope analyses at low concentration levels with femtosecond-LA-MC-ICP-MS

rather the ionization mechanism itself could be the reason for inaccurate results. Indeed, a decrease of the RF power to 900 W appears to suppress the observed matrix-effect considerably, indicating that it is generated in the plasma by the ionization of the main matrix elements. The relationship of the plasma temperature and RF power has been shown by Longerich (1989), who determined the plasma temperature to decrease about 4000 K when decreasing the RF power from 1500 W to 1200 W. "Cool" plasma conditions applied here allow to ionize elements with a moderately low first ionization potential, such as Li (5.39 eV), while enhancing the formation of oxides for elements with higher ionization potential such as Th (6.30 eV). The occurrence of cooler plasma conditions than usual is supported by an elevated metal oxide/ metal ion rate of Th. Decreasing the temperature of the plasma, by decreasing the Plasma power to 900 W, eliminates the observed matrix effect and results in matrix-independent accurately measured δ^7Li-values (Figure 1.6 (c) and (d)).
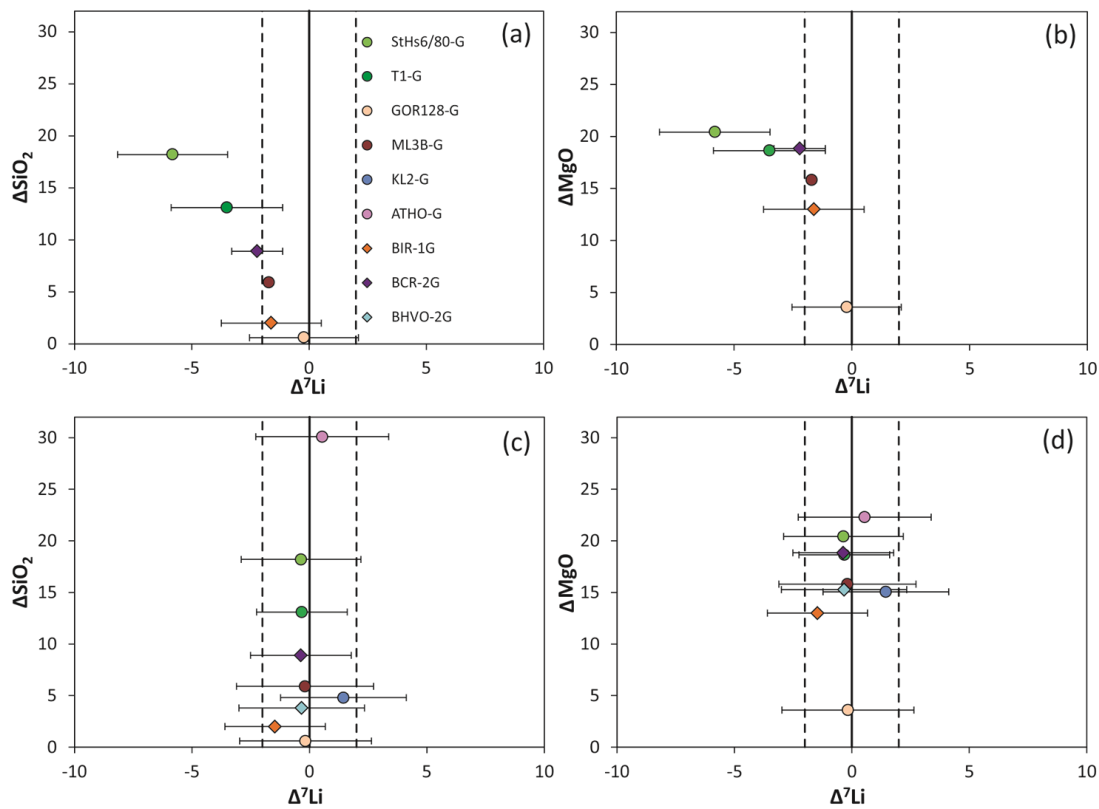
Figure 1.6: (a) + (b) δ^7Li values (Δ^7Li = δ^7Li$_{measured}$ - δ^7Li$_{published}$) showing deviations of up to 8 ‰ from true values at RF power of 1080 W with increasing deviations for increased differences in matrix elements, represented by (a) ΔSiO$_2$ (SiO$_2$ $_{sample}$-SiO$_2$ $_{GOR132-G}$) and (b) ΔMgO (MgO$_{sample}$-MgO$_{GOR132-G}$) (c) + (d) deviations from true values are reduced to 2 ‰ when the RF power is reduced to 900 W.

Chapter 1: *In situ* high-precision lithium isotope analyses at low concentration levels with femtosecond-LA-MC-ICP-MS

Due to lower RF power the ionization efficiency in the plasma is reduced as described by Saha (1920). As a result, several matrix elements with a high first ionization potential, such as Si, are not ionized efficiently. In particular, the proportionately most abundant matrix elements, including Si (8.15 eV), Mg (7.65 eV) and Fe (7.90 eV) are expected to be ionized to a lesser extent at cooler plasma conditions relative to Li, which has a lower ionization potential of 5.39 eV and thus still ionizes effectively at cooler plasma conditions (Tanner, 1995). Boron should also be affected by the above effects and a matrix difference should play a significant role since a reduction in plasma power can only be applied in a limited way for B due to its higher first ionization potential of 6.11 eV (Kramida and Ryabtsev, 2007). However, these effects have not been observed during B isotope analyses even though large differences in matrix between the bracketing standard (SRM NIST-612) and sample (calcite) exist (Lloyd et al., 2018). Potentially, quadruply charged ^{24}Mg and ^{28}Si ions may cause an interfering peak close to that of ^{6}Li and ^{7}Li, respectively. This might have a crucial influence on the peakshape especially in the low mass region and therefore on the accuracy of the measurements. Therefore, we suspect that the formation of multiply charged ions with higher ionization potentials, which are suppressed at cool plasma conditions, are the major cause for the observed matrix effects. In either case, our findings indicate that it is important to avoid the ionization of matrix elements in the plasma, as Li is the lightest element measurable with MC-ICP-MS and will be extracted from the plasma most easily.

1.5.3   Measurements of MPI-DING and USGS reference glasses

Each reference glass has been measured in numerous sessions over a period of 8 month with 10 measurements or more per sample (Figure 1.7). The laser ablation data of this study have been compared with USGS and MPI DING reference glasses which have been measured previously by other authors applying well-established methods. Within the analytical uncertainty of 2 ‰ (2σ) the measured δ^{7}Li values are in agreement with the values determined in previous studies (Figure 1.7; see figure caption for references). The total uncertainty indicated by the error bars may be slightly larger than the analytical uncertainty alone due to small isotopic heterogeneities within the reference materials. Variations in the Li isotope concentration occur in different splits of the

Chapter 1: *In situ* high-precision lithium isotope analyses at low concentration levels with femtosecond-LA-MC-ICP-MS

reference glasses and even small scale heterogeneities can be observed for some glasses (Jochum et al., 2006). Potentially occurring fractionation of Li isotopes might have occurred during the production of the reference glass by diffusion during the quenching process or differing compositions of Li isotopes in the rim areas of the quenched glass. The value for ATHO-G of Jochum et al. (2011) (3.9 ±0.8 ‰ (2 SD)) and this study (4.6 ‰) both measured by solution MC-ICP-MS has been confirmed with the *in situ* method developed here (4.0 ± 2.8 ‰ (2 SD)) but deviates from the values determined at 17.1 ‰ by Jochum et al. (2006) (MC-ICP-MS), and 18.2 ‰ by Le Roux (2010) (LA-MC-ICP-MS). Jochum et al. (2011) assume the deviation to be caused by an analytical problem but potentially the ATHO-G reference glass is affected by large heterogeneities causing this deviation or matrix effects might also play a role. For BIR-1G, our own measurements indicate isotopic heterogeneities between two pieces of the reference material. Measurements displayed in Figure 1.7 and Figure 1.8 are all performed from one piece of BIR-1G and have a mean δ^7Li of 3.6 ± 1.9 ‰ (2 SD). Two measurements of a second piece of this reference material, however, yielded δ^7Li of 0.7 ‰ and 0.5 ‰. These latter measurements have not been taken into account for the cross calibration. These findings indicate that the mean value of the other studies from the literature (5.9 ±1.9 ‰ (2 SD)) might also result from the analyses of different pieces with heterogeneous Li isotope compositions. Nevertheless, the measured values for the other reference glasses are in overall agreement with the published data. The single measurements which are averaged for the cross calibration are shown separately per reference glass in Figure 1.8. Furthermore, the values for the single measurements are available in Table A.1.3 in the appendix.

Chapter 1: *In situ* high-precision lithium isotope analyses at low concentration levels with femtosecond-LA-MC-ICP-MS
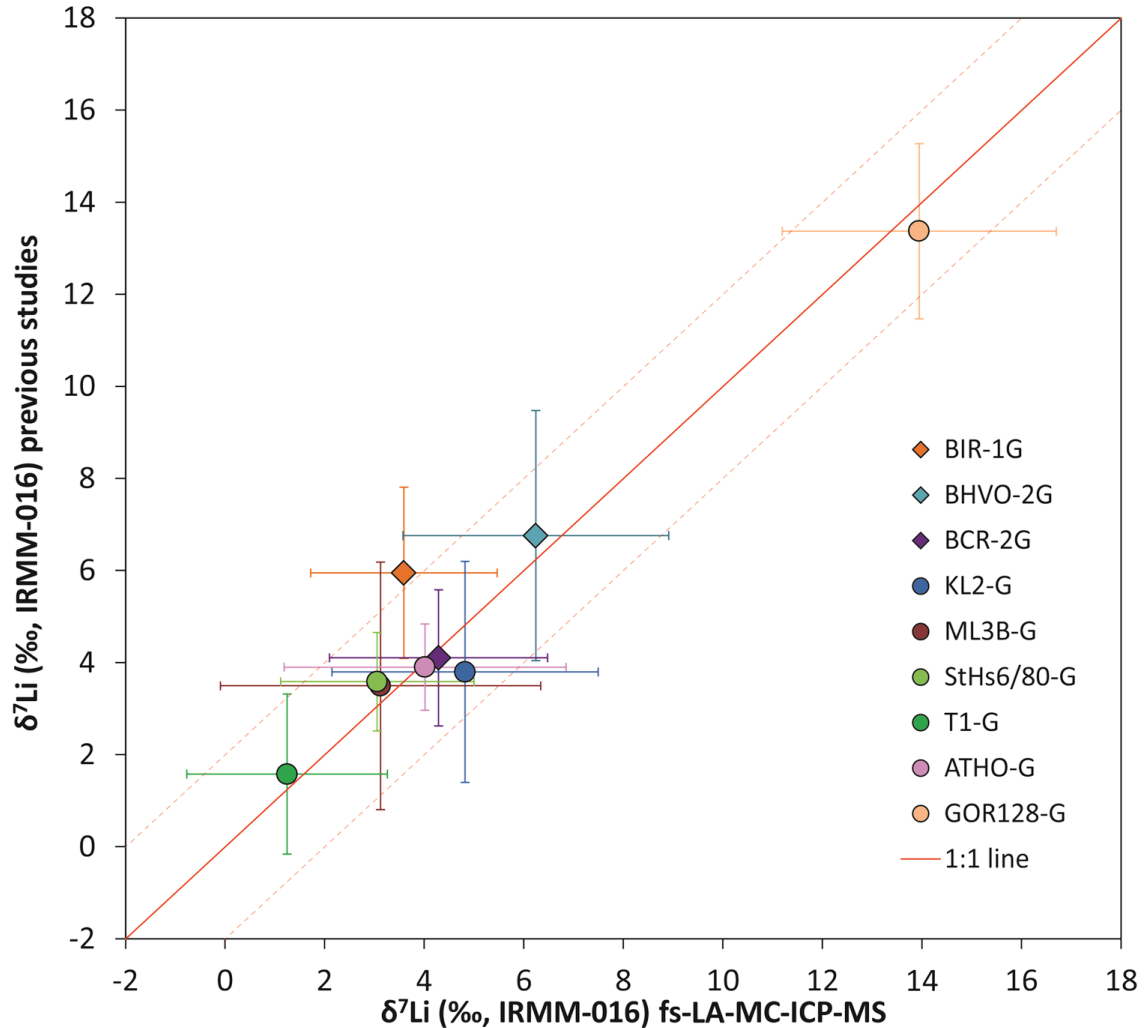
Figure 1.7: Femtosecond-LA-MC-ICP-MS data (this study) plotted against mean values of published data, error bars represent 2 SD of all values taken into account. Dashed lines represent the accepted 2 ‰ deviation from the 1:1 line. BIR-1G was determined by SIMS and MC-ICP-MS (Kasemann et al., 2005) and LA-MC-ICP-MS (Le Roux, 2010; Xu et al., 2013), BHVO-2G by SIMS and MC-ICP-MS (Kasemann et al., 2005) and by LA-MC-ICP-MS (Xu et al., 2013), BCR-2G by SIMS and MC-ICP-MS (Jochum et al., 2006) and SIMS, TIMS and MC-ICP-MS (Kasemann et al., 2005), KL2-G by SIMS (Jochum et al., 2006), LA-MC-ICP-MS (Le Roux, 2010; Xu et al., 2013), ML3B-G, T1-G and GOR128-G by SIMS and MC-ICP-MS (Jochum et al., 2006) and LA-MC-ICP-MS (Le Roux, 2010; Xu et al., 2013), StHs6/80-G by MC-ICP-MS (Jochum et al., 2006) and LA-MC-ICP-MS (Xu et al., 2013), ATHO-G by MC-ICP-MS (Jochum et al., 2011) and LA-MC-ICP-MS (Le Roux, 2010; Xu et al., 2013) and GOR132-G by SIMS and MC-ICP-MS (Jochum et al., 2006) and LA-MC-ICP-MS (Xu et al., 2013). Furthermore, BIR-1G, BCR-2G, BHVO-2G, GOR128-G, T1-G, KL2-G, ML3B-G and ATHO-G have been measured in this study by MC-ICP-MS. GOR132-G was used as bracketing standard for the measurements displayed and calculated with 8.6 ± 1.1 ‰ (2 SD) which has been measured by MC-ICP-MS (Jochum et al., 2006) and in this study, SIMS (Jochum et al., 2006) and LA-MC-ICP-MS (Xu et al., 2013).

Chapter 1: *In situ* high-precision lithium isotope analyses at low concentration levels with femtosecond-LA-MC-ICP-MS
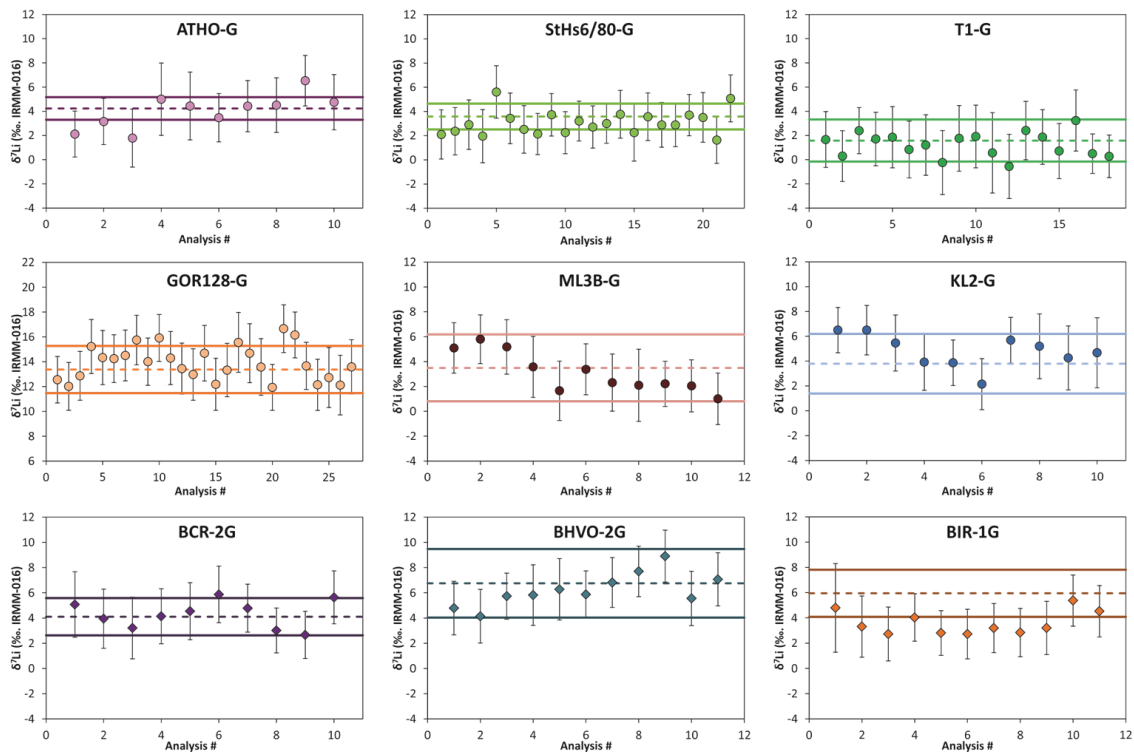
Figure 1.8: δ⁷Li values of MPI-DING and USGS reference glasses measured over a period of 8 months, each reference glass has been measured at least 10 times in at least 3 sessions on different days except for ATHO-G which has been measured in two distinct sessions. Dashed lines are the means of published values and the MC-ICP-MS results in this study, solid lines are 2 standard deviations of these values. Error bars are 2 SD values of standard-bracketing measurement and give the counting statistical error thereof.

1.5.4 Application: Zoned olivine from Banne D'Ordanche

Chemical zoning in magmatic minerals can result from chemical diffusion caused by concentration gradients which develop, e.g. during cooling and evolution of a magma, between minerals and the surrounding melt (Richter et al., 2003; Richter et al., 2009). A number of studies have shown that large isotope fractionation at magmatic temperatures is caused by diffusion (Teng et al., 2006; Weyer and Seitz, 2012). Using *in situ* isotope analyses techniques, e.g. SIMS (Jeffcoate et al., 2007; Sio et al., 2013), or fs-MC-ICP-MS (Oeser et al., 2014), previous studies have shown that chemical and isotopic zoning are frequently coupled and that isotopic zoning can be used to confirm a diffusion origin and elucidate complex evolution of magmatic systems (Sio et al., 2013; Oeser et al., 2015; Oeser et al., 2018). A motivation of this study is to establish the fast-diffusing Li isotope system comparatively to the yet more established Fe-Mg exchange diffusion couple for such applications, with an improved analytical technique.

Chapter 1: *In situ* high-precision lithium isotope analyses at low concentration levels with femtosecond-LA-MC-ICP-MS

In Figure 1.9 an olivine from Banne D'Ordanche (Massif Central, France) was analyzed for its Li isotope composition. The olivine grain is chemically zoned in Mg# and the Li concentration which varies from 8.5 µg/g at the rim to 2 µg/g in the core. Lithium concentration zoning is coupled to the chemical zoning for Fe and Mg shown as Mg#, indicating broadly similar diffusion rates for Li and Fe-Mg exchange diffusion in this case. Lithium isotopes are shown to fractionate as well with a variation from 2.3 ±2.3 ‰ (2 SD) in the rim area to -11.3 ±3.2 ‰ (2 SD) in the core. A fractionation of ~13.6 ‰ from rim to core shows that small scale diffusion profiles (< 150 µm) can be clearly resolved with fs-LA-MC-ICP-MS.
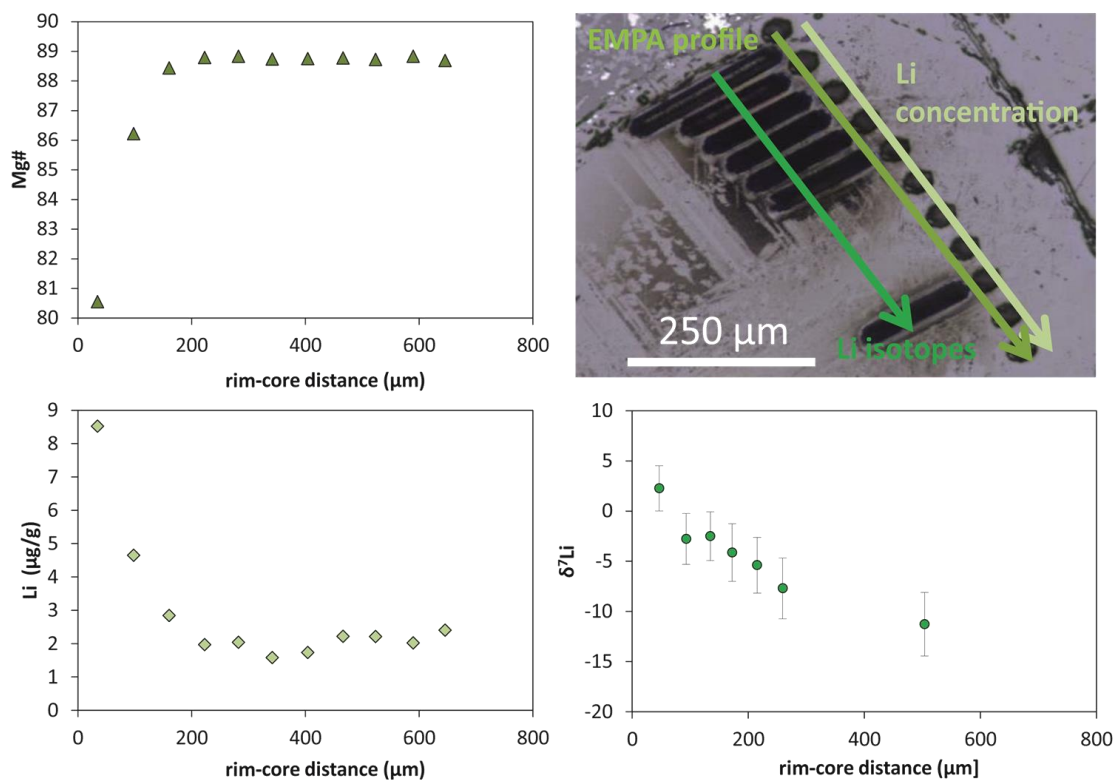
Figure 1.9: Chemical zoning in Mg# (a) and Li (c) in olivine from Banne D'Ordanche. (b) shows the measurement lines parallel to the crystal rim and (d) shows the isotopic variation along the profile.

Chapter 1: *In situ* **high-precision lithium isotope analyses at low concentration levels with femtosecond-LA-MC-ICP-MS**

1.6 Conclusion

Lithium isotope ratios can be determined reliably by fs-LA-MC-ICP-MS, even for glasses and minerals with low Li concentrations (µg/g range), with a precision and accuracy in the order of ~ 2‰. Signal intensities down to ~80 mV can be measured with FC11-FC13 and signals below that should be detected with FC13-SEM corresponding to concentrations >10 µg/g and <10 µg/g, respectively. With the most sensitive detector combination FC13-SEM concentrations down to 1 µg/g can be measured with sufficient spatial resolution (spot size on olivine ~30 µm). The necessity of applying ion counters and high resistance amplifiers (10^{13} Ω) instead of the standard amplifiers (10^{11} Ω) has been proven because for low concentrations the added counting statistical and noise influenced error of a 10^{13} Ω amplifier undermatch that of a 10^{11} Ω amplifier.

It has also been shown that integration times of 1.049 s can be used with 10^{13} Ω amplifiers due to signal stability owing to the mixed gas flows. The tau correction is necessary due to the difference in signal decay time of different detector types. The effect shows in improved precisions for single measurements and according to these adapted δ-values though there is no observable effect regarding accuracy. The application of a very simple mixing cell for gas and aerosol homogenization leads to an increased signal stability and thus limits the impact on accuracy of the tau correction.

Due to low signal intensities three factors are critical for the determination of precise Li isotope ratios: (a) the signal stability and consequently lower internal uncertainty which can be improved by gas homogenization of the sample aerosol and He mixture; (b) the detector combination, in order to optimize uncertainties generated by counting statistics and detector noise and (c) low background levels to prevent influences on the signal-to-noise ratio. The utilization of cooler plasma conditions appears to suppress the ionization of matrix elements in the plasma and results in matrix-independent and more accurate Li isotope measurements.

Chapter 2: Lithium bulk isotope analyses and implications on Roche Sauterre basanite body and Sapat olivine

2.1 Abstract

Bulk isotopic analyses can enlighten the distribution of elements over a larger scale than single crystals but e.g. on an outcrop scale. The lithium isotope analytical procedure has been calibrated by collecting the Li fraction in an 11 ml step to grant for sufficient separation from Na. A strong fractionation from +80 to -30 ‰ has been observed on the column which proves the importance of a zero-loss tolerance of the Li fraction. Measurement of the solution is performed with MC-ICP-MS at concentration levels of 10 ng/g Li yielding 30 to 50 pA signal intensity on ^{7}Li and applying sample-standard bracketing with IRMM-16 used as a reference. Background levels are increasing throughout a measurement period and thus are monitored and corrected.

The investigated samples have been taken from a single outcrop in the Massif Central volcanic region (France) and are distributed over a 60 m long outcrop to test for the hypothesis of diffusive transport of Li isotopes along the outcrop scale. The results, however, show homogenous Li isotope ratios, ranging between +2.1 and +3.3 ±2.0 ‰ except from one sample which yields a δ^7Li-value of 10.5 ±1.8 ‰. The measured δ^7Li-values coincide with the range of unaltered volcanic whole-rock suites worldwide (+2.0 to +5.0 ‰) and the value determined for the bulk silicate Earth (+3.5 to +4.0 ‰). The sample from the top of the lava flow with δ^7Li = 10.5 ‰ is accompanied by a lower Li concentration which suggests a degassing process. The isotopic composition cannot be explained by degassing, hence a procedural error is suspected. For two of the samples a whole rock as well as a matrix sample, free of olivine and pyroxene phenocrysts, have been investigated yielding 0.8 -1 ‰ higher δ^7Li-values (2.1 vs.2.9 ‰ and 2.4 vs. 3.4 ‰) coinciding with the interpretation that light Li diffuses into the phenocrysts during magma evolution due to a chemical gradient with higher Li concentration in the melt compared to the crystals. A large hydrothermally formed olivine single crystal with a diameter of ~1.5 cm from Sapat (Kohistan, Pakistan) has been analyzed with fs-LA-MC-ICP-MS and by solution MC-ICP-MS and yielded a δ^7Li value of 19.2 ± 1.3 ‰ (2SD) and 8.6 ± 1.3 ‰ (2 SD), respectively. Fluid or melt inclusions in the crystal are suspected to account for the deviation in δ^7Li between the two methods.

Chapter 2: Lithium bulk isotope analyses and implications on Roche Sauterre basanite body and Sapat olivine

2.2 Introduction

Bulk lithium isotope analyses have been reported by various studies (e.g. Košler et al., 2001; Seitz et al., 2004) with the aim to investigate high temperature isotope fractionation in mantle peridotites (e.g. Brooker et al., 2004; Seitz et al., 2004; Ionov and Seitz, 2008; Pogge von Strandmann et al., 2011) volcanic rocks such as mid-ocean ridge basalts, ocean-island basalts and intra-plate volcanics (e.g. Chan et al., 1992; Chan and Frey, 2003; Moriguti et al., 2004; Ryan and Kyle, 2004; Marks et al., 2007; Vlastélic et al., 2011; Krienitz et al., 2012) and extraterrestrial material from the Moon, the Mars and chondrites (e.g. Magna et al., 2006; Seitz et al., 2006; Pogge von Strandmann et al., 2011). Isotopic signatures are used to trace geological processes as it has been tried for isotopically heavy fluids escaping from subducted slabs. The mantle wedge is enriched in heavy Li and the isotopic composition of the mantle wedge rocks increases. The dehydrated and depleted slab with a consequently light isotopic composition is transported into the mantle (Zack et al., 2003; Marschall et al., 2007a; Nishio et al., 2007). Abundant suites of magmatic rocks have been analyzed for their Li isotopic composition, and it has been widely found that the mean δ^7Li-value of different rock types (e.g. MORB, OIB, island arc volcanics, middle continental crust) is ~4 ‰ (Figure 1 in Penniston-Dorland et al. (2017) and references therein). In natural peridotites a large range of δ^7Li-values from -9.7 to +9.6 ‰ has been determined by several authors (Brooker et al., 2004; Seitz et al., 2004; Magna et al., 2006; Jeffcoate et al., 2007; Ionov and Seitz, 2008; Magna et al., 2008; Pogge von Strandmann et al., 2011; Ackerman et al., 2013) whereas the isotopic composition of fresh mid-ocean ridge basalts varies between +2 ‰ and +5 ‰ (Chan et al., 1992; Elliott et al., 2006; Tomascak et al., 2008). Altered MORB samples and ocean floor sediments tend to have higher δ^7Li values due to the uptake of heavy Li from seawater over time (Chan et al., 1992). Ocean island basalts range between +2.5 ‰ and +5.7 ‰ (Tomascak et al., 1999b; Chan and Frey, 2003; Kobayashi et al., 2004). Nevertheless, isotopic signatures outside of this global volcanic range are assigned to either shallow-level crustal contamination (Kobayashi et al., 2004), recycling of altered oceanic crust, or parts of metasomatized subarc mantle (Elliott et al., 2006; Marschall et al., 2007b). In non-magmatic systems the range of δ^7Li is wider, due to the preferential dissolution of ^{7}Li under equilibrium conditions due to the preference of partitioning into the site with the highest bond energy (Schauble, 2004) and due to preferential adsorption or

Chapter 2: Lithium bulk isotope analyses and implications on Roche Sauterre basanite body and Sapat olivine

incorporation of [6]Li to secondary minerals (Taylor and Urey, 1938; Chan et al., 1992; Huh et al., 1998; Pistiner and Henderson, 2003). This causes waters to be isotopically heavy (e.g. seawater 31 ‰ (Millot et al., 2004b)) and secondary minerals to be enriched in [6]Li (Kisakurek et al., 2004; Rudnick et al., 2004; Pogge von Strandmann et al., 2006; Teng et al., 2010).

The aims of this study are (i) to investigate the spatial scale of Li diffusion in magmatic systems, and (ii) to evaluate if there is a continuous spatial variation of δ^7Li within a large lava body such as a lava flow or lava lake. The question which should be addressed is, if Li is only redistributed between the minerals and melt in an effectively closed system or if the melt is acting as a larger reservoir as in an open system. In order to answer these questions, the column chromatographic separation method and mass spectrometric measurement of Li isotopes with MC-ICP-MS has to be established at the Institute of Mineralogy at the University Hannover.

2.3 Samples

The chromatographic separation method for Lithium from the rock matrix shall be tested and calibrated for the geochemistry lab at the University Hannover. For the first test run a multi element mixture with 20 µg/g Li has been produced, further constituents of the mixture (Al, Ca, Fe, Mg, Na, Ni, Ti and Mn) had the purpose to mimic a basaltic matrix, the exact composition and chemicals data is summarized in the appendix (Table A.2.1).

The samples investigated in this study were collected by M. Oeser in 2011 from an outcrop in the Massif Central volcanic region. The location of the outcrop is the abandoned quarry of Roche Sauterre (N 45°54.858', E 02°55.674') in the Chaîne de Puys. It comprises olivine-phyric basanites from an eruption during late Miocene to early Pliocene that formed a massive lava flow or even perhaps a small lava lake (Nehlig et al., 2001; Lorand et al., 2003). Eight samples were taken from the outcrop over a horizontal distance of ~50 m, all except one sample have been taken on the base of the lava flow, one sample has been taken at the top of the lava flow ~20 m above the other samples. A photograph of the outcrop can be found in the appendix (Figure A.2.1). The samples were ground to a fine powder and for two samples the

Chapter 2: Lithium bulk isotope analyses and implications on Roche Sauterre basanite body and Sapat olivine

basaltic matrix, after previous separation of olivine phenocrysts, as well as the whole rock (including phenocrysts) was measured.

Additionally, an olivine single crystal with a diameter of ~ 1 cm originating from Sapat, Kohistan in Pakistan has been investigated. The aim of this thesis is to determine the Li isotope composition not only of bulk volcanic rocks but also of the olivines in the volcanic matrix. The Sapat olivine was chosen for analysis because of its size which gives enough material for a solution analysis. The mafic-ultramafic body has been sheared during the emplacement of the Kohistan magmatic arc onto the Indian plate during the early Paleocene and post-tectonically mineralized and partially serpentinized due to hydrothermal activity affecting the dunite body. Gem quality minerals up to 15 cm length have been extracted from pockets and veins of these rocks and yield a Mg# varying from Fo_{89} to Fo_{97} (Jan and Khan, 1996). Parts of the olivine were separated by laser cutting and afterwards cleaned and crushed in an agate mortar.

2.4   Methods

2.4.1   Lithium column chromatography

The lithium column chromatography and sample dissolution procedure has been described in detail in Seitz et al. (2004), the column separation has been modified after the procedures of Tomascak et al. (1999a) and Bouman et al. (2004). Sample dissolution of powdered rock samples in 15 ml teflon beakers was performed with a 3:1 mixture of HF (Merck) and HNO_3 to break the silicate bonds. After drying on the hot plate HCl is used to break fluoride bonds and cast out the fluorides and HNO_3 is used to dissolve sulfides and break organic bonds (Heinrichs, 1989). HNO_3 and HCl are distilled in a quartz glass at sub-boiling conditions from pro analysi grade and checked on a frequent basis for contaminations. A detailed list of the sample dissolution procedure can be found in the appendix (Table A.2.1). In this procedure the separation is conducted on a single column filled with a cation resin (BioRad AG50W-X8, 200-400 mesh) (Seitz et al., 2004). The resin is filled into an in-house built polyethylene column with a diameter of 0.55 cm, a column height of 6.5 cm and a resin volume of 1.4 ml which is produced by inserting a filter into a cut polyethylene one-way pipette (Figure 2.1).

Chapter 2: Lithium bulk isotope analyses and implications on Roche Sauterre basanite body and Sapat olivine
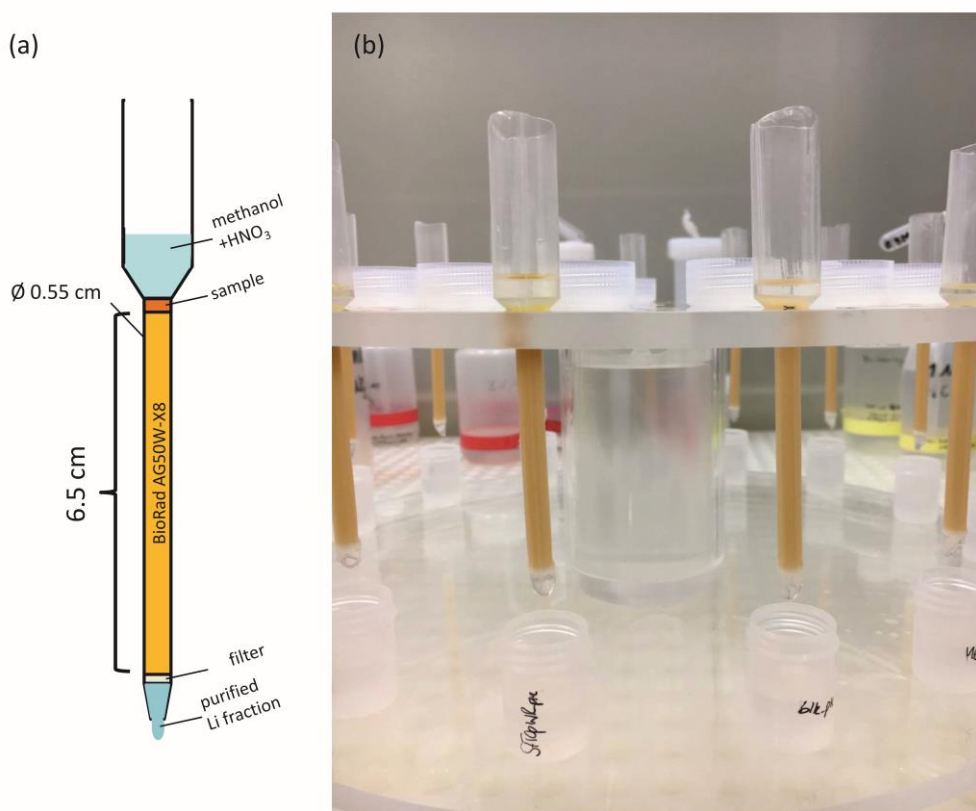
Figure 2.1: (a) Sketch of the polyethylene columns with 1.4 ml resin reservoir and (b) columns filled with BioRadAG50W-X8 resin and loaded sample, the matrix remains on the resin and is visible as darker part at the upper resin part.

The resin consists of an active group which is bound to a sulfonic group $(R\text{-}SO_3)^-$ and H^+ as a mobile counter ion (Chiarizia et al., 1997). During the procedure of column separation the present H^+ cation is successively replaced by the cations of the sample. The relative selectivity for Li^+ (0.85) is smaller than that for the other matrix cations (e.g. Na^+ 1.5 and Mg^{2+} 2.5) which causes that Li is washed off the column at first. The sample is loaded with a mixture of 0.18 ml 5 M HNO_3 and 0.72 ml distilled methanol (Roth, ROTISOLV Ultra LC-MS grade) which was distilled by H.-M. Seitz at the Goethe-Universität Frankfurt. After that an eluent of a mixture of 4:1 methanol and 5 M HNO_3 is put onto the columns. 11 ml of this eluent is collected to make up for the Li fraction starting from ml 3.9 after sample loading. A 4:1 mixture of HNO_3 and methanol has been found to separate the element couple Li and Na best from the used resin (Strelow et al., 1974). The molarity of this mixture has to be 1 M ± 0.05 M, solutions

Chapter 2: Lithium bulk isotope analyses and implications on Roche Sauterre basanite body and Sapat olivine

with deviating molarities cause the Li fraction to be washed off the column earlier (molarity > 1M) or later (molarity < 1M) which results in an incomplete collection of the Li fraction and thus a fractionated isotopic composition. Columns have been loaded with sample concentrations of 29.2 to 49.6 ng/g Li which corresponds to ~5-7 mg of powdered and dissolved rock sample. For the column calibration with multi element solution two columns have been loaded with ~20 µg/g Li. One column was used to determine a procedure blank and for the determination of analytical accuracy the reference material JB-2 was treated as additional unknown in each chromatography run.

2.4.2   Lithium and sodium concentrations analysis

Fractions of 2 ml column eluent were taken for the calibration with the multi-element solution, and Li and Na concentrations were measured with a Varian715-ES inductively coupled plasma optical emission spectrometer (ICP-OES). Multi-element solutions with concentrations of 5, 10, 20 and 40 µg/g Li were prepared for the calibration of the instrument, Na is abundant in the calibration solutions with a factor of 2.5 to Li. Measurements of Li were performed at three wavelengths of which the measured concentrations were averaged (460.289 nm, 610.365 nm and 670.783 nm) and for Na concentrations of two wavelengths were averaged (588.995 nm and 589.592 nm). The concentration measurements of the rock samples were performed with a Thermo-Scientific Element XR sector field inductively coupled plasma mass spectrometer (SF-ICP-MS). For the calibration of the instrument and standardization for the concentration measurements multi-element standard solutions were gravimetrically prepared for Li concentrations from 1 to 500 ng/g. For the measurements all samples were internally standardized with a 5 ng/g Rh solution (Merck, concentration in stock solution 10,000 mg/l). As in-house standard TMDA 51-4 (trace metal fortified water, National Water Research Institute (Canada), 15.1 µg/L Li) and SDO-1 (shale powder, U.S. Geological Survey, 28.6 µg/g Li) were measured and the precision of the concentration analyses were typically better than 10 % (2 SD) and the detection limit for Li was 1 ng/g (determination for 10 measurements with linear regression).

Chapter 2: Lithium bulk isotope analyses and implications on Roche Sauterre basanite body and Sapat olivine

2.4.3 Lithium isotope analysis

Bulk Li isotopic analyses were conducted on a Thermo-Scientific Neptune Plus MC-ICP-MS for simultaneous measurement of ^6Li and ^7Li. Following Seitz et al. (2004), a Cetac Aridus II desolvation unit equipped with a pneumatic nebulizer with an uptake rate of ca. 50 µl/min fitted into a PFA spray chamber was used. The N_2 gas was not used to flush the membrane in order to prevent interferences of doubly charged $^{14}N^{++}$ on ^7Li in the plasma. An ensemble of a sample H cone and a skimmer X cone was used without spacer. For isotope analyses, a 10 ng/g Li solution was introduced into the mass spectrometer which typically yields an ion current of 30 to 50 pA on ^7Li (3 to 5 V on a 10^{11} Ω amplifier). Sample analysis was performed sequentially by applying sample-standard-bracketing with the IRMM-16 Li reference solution($^7Li/^6Li$=12.17730 (Qi et al., 1997)) which is isotopically similar within the uncertainties of the measurements (~ 2 ‰) to the exhausted NIST-LSVEC ($^7Li/^6Li$=12.17285 (Flesch et al., 1973) but several authors measured higher $^7Li/^6Li$ (e.g. Huh et al., 1998; James and Palmer, 2000; Moriguti et al., 2004)). (Jeffcoate et al., 2004) bracketed IRMM-16 with NIST L-SVEC and received a δ^7Li of 0.14 ± 0.04 ‰ (2 SE) and thus conclude that IRMM-16 is slightly heavier than NIST L-SVEC. Due to issues with accumulating background in the analytical setup, acid and procedure blank measurements were performed every 10-15 measurements and the background was monitored carefully. Two measurement periods consisting of 1 to 3 days have been performed and throughout these measurement times the long term δ^7Li of the reference material JB-2 (basalt powder, Geological survey of Japan) relative to IRMM-16 is 3.2 ± 1.2 ‰ (2 SD) which is comparable within the error to the compiled literature values of 3.5-4.9 ‰ (Brant et al., 2012; Dellinger et al., 2014; Coogan et al., 2017) (Figure 2.4).

2.5 Results and discussion

2.5.1 Column calibration

First tests were performed with a multi-element solution to check if there is isotopic fractionation taking place throughout the elution of the Li fraction (Taylor and Urey, 1938). Concentration measurements show that the Li fraction can clearly be distinguished from the Na fraction which is washed off the column later. The complete

Chapter 2: Lithium bulk isotope analyses and implications on Roche Sauterre basanite body and Sapat olivine

Li fraction can be collected with 11 ml of elution volume, and 70-80 % of the fraction is collected within the first 2 ml of the eluent volume. The diagrams show that the fraction with the largest proportion of Li has a δ^7Li close to zero (Figure 2.2, -4.8 ‰ for Column 1 and -0.4 ‰ for Column 2). With increasing amounts of Na in the sample the tailing of the Na elution peak is increasingly interfering with the Li elution peak, which is an issue especially for saline groundwater and seawater. But unlike for SIMS analyses (where the Na abundance may be an issue), MC-ICP-MS analyses can be performed even when small amounts of Na are abundant in the purified sample (Tomascak et al., 1999a). Jeffcoate et al. (2004) doped the Na-free NIST L-SVEC Li-solution with a Li-free Na-solution to achieve Na/Li ratios from 0.2 to 10 and observed that Na/Li ratios > 0.5 cause a significant deviation in δ^7Li to negative values. Tomascak et al. (1999) point out that it is more important to retain the whole Li fraction to prevent isotope fractionation on the column instead of separating Na completely. Furthermore, the fractionation over the column is quite large with variations from ca. +80 ‰ to ca. -30 ‰, indicating the importance of collecting the whole Li fraction in order to obtain correct isotopic values. The investigation of potential column-induced Li isotope fractionation has been repeated with IRMM-16 (Figure A.2.1 in the appendix) and showed the same trend in agreement with (Košler et al., 2001).

Furthermore, elution curves for an olivine (SAP) and two basaltic samples (JB-2 and St7WR) were measured to calibrate the columns. For this purpose sample proportions with Li concentrations of 30 to 50 ng/g were loaded onto the columns. The basaltic samples show a flatter wash out of Li and an elution peak which is somewhat broader than that of the olivine. This might be caused by the matrix elements present in the basalts which are not present in olivine and is similar to the elution curves that (Seitz et al., 2004) observed for an olivine and the basalt JB-2 (Figure 2.3).

Chapter 2: Lithium bulk isotope analyses and implications on Roche Sauterre basanite body and Sapat olivine

Figure 2.2: (a) Elution curves and (b) isotopic composition determined from multi element solution and eluent fractions of 2 ml on two columns, which were run parallelly.

Chapter 2: Lithium bulk isotope analyses and implications on Roche Sauterre basanite body and Sapat olivine
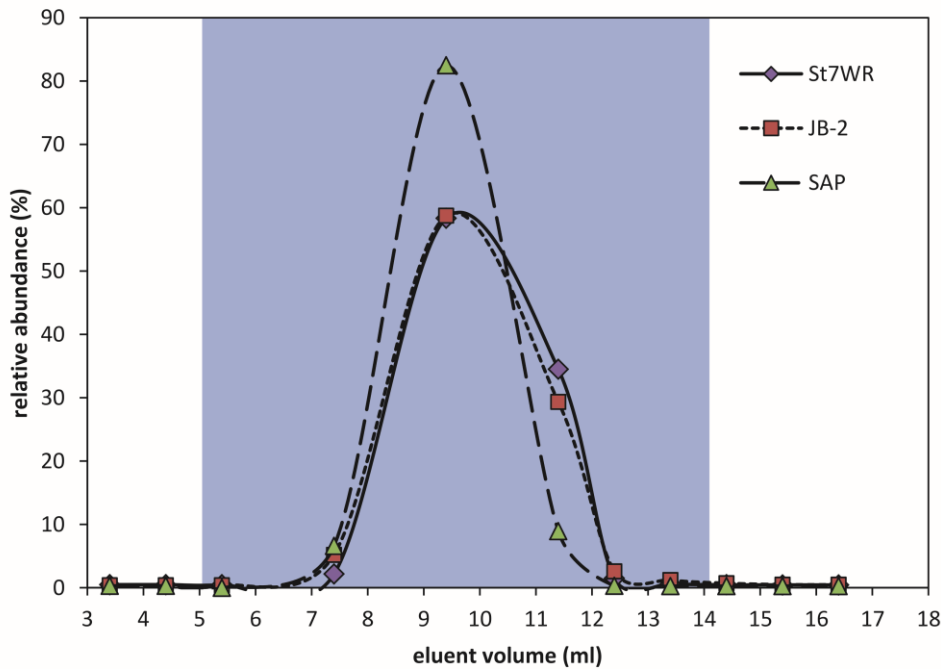
Figure 2.3: Elution curves of basaltic samples (JB-2 and St7-WR) and olivine (SAP). Elution for Li from the basaltic matrix is more distributed amongst 2 ml cuts, and Li is washed off the column ca. 1 ml later when compared to an olivine matrix.

The measured δ^7Li-value of 3.2 ± 1.2 ‰ (2 SD) in this study is, compared to the δ^7Li-reference value of JB-2 as measured by MC-ICP-MS relative to L-SVEC of 3.9 -5.2 ‰ (compiled in Seitz et al. (2004)), in the lower range of the measured values but still in the acceptable range within error. (Teng et al., 2009) measured a δ^7Li value of 3.6 ± 0.9 (2 σ) which is coinciding very well with the result in this study (Figure 2.4). Furthermore, the measurements in this study have been performed with IRMM-16 as bracketing standard for the calculation of δ^7Li because L-SVEC is not available anymore and IRMM-16 has been determined to be equal to L-SVEC (Qi et al., 1997). So far there are only three studies that record δ^7Li-values of JB-2 relative to IRMM-16, they yield δ^7Li-values of 4.2 ± 1.6 ‰ (2SD) (n=4) (Brant et al., 2012), 4.47 ± 0.53 ‰ (2 σ) (Dellinger et al., 2014) and 4.2 ± 0.6 ‰ (2 SE) (Coogan et al., 2017). Errors during column separation are unlikely because two separate column passes in two distinct column separation sessions have been measured and show comparable δ^7Li-values (session August2018, δ^7Li=3.4 ± 1.1 ‰, n=9 and session April2019, δ^7Li=2.7 ± 0.4 ‰, n=4). This proves the reliability of the separation process.

Chapter 2: Lithium bulk isotope analyses and implications on Roche Sauterre basanite body and Sapat olivine
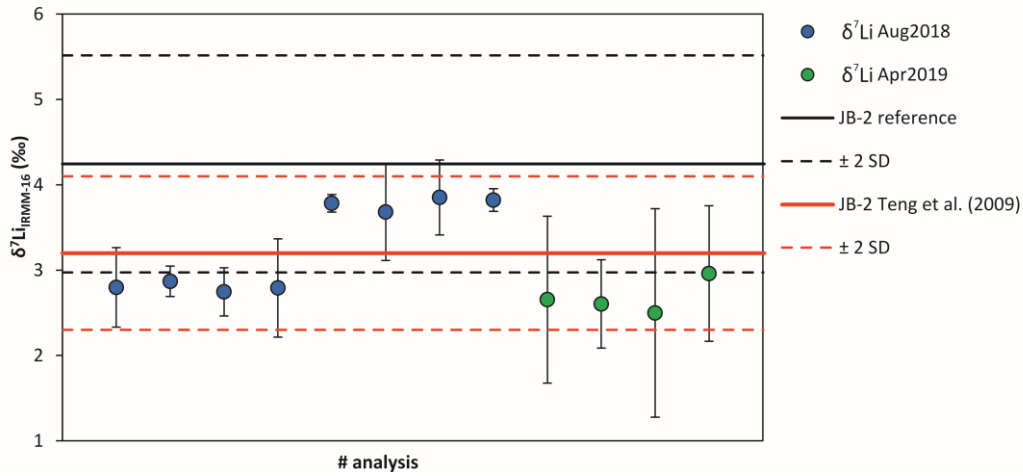
Figure 2.4: Reproducibility of Neptune Plus MC-ICP-MS Li isotope measurements of two sessions April2019 and August2018 with error bars of 2 SD per analysis, "JB-2 reference" is a mean value calculated from Brant et al. (2012); Dellinger et al. (2014) and Coogan et al. (2017) with 2 SD error and n=6, and "JB-2 Teng et al. (2009)" with 2 σ error and n=4.

2.5.2   Roche Sauterre basanite and Sapat olivine

Three batches of the SAP olivine have been measured and yield a mean value of 8.6 ± 1.3 ‰ (n=8). The same SAP grain has been measured with fs-LA-MC-ICP-MS and yielded a δ^7Li value of 19.2 ± 1.3 ‰ (n=7). The analyzed whole rock samples from Roche Sauterre yield δ^7Li values varying from +2.1 to +3.3 ‰ with one sample giving a δ^7Li of 10.5 ‰. The matrix samples are slightly heavier than the whole rock sample from the same location (Table 2.1 and Figure 2.5).

Table 2.1: Bulk Li isotope results for the olivine SAP and Roche Sauterre samples (SAP = Sapat olivine; St = Roche Sauterre; m = matrix without olivine and pyroxene phenocrysts, WR = whole rock)

	JB-2	SAP1	SAP2	SAP3	St7 WR	St6 WR	StTopWR	St4 WR	St3 WR	St2bWR	St1 WR	StR WR	St7 m	St1 m
δ^7Li (‰)	3.2	8.3	9.0	8.5	2.4	3.3	10.5	2.9	2.3	2.2	2.1	3.0	3.4	2.9
2 SD	1.2	2.0	1.2	1.2	1.2	1.2	1.8	1.2	2.0	1.2	1.2	1.2	2.6	2.9
n	13	3	3	2	8	3	4	3	3	4	8	3	9	8

Chapter 2: Lithium bulk isotope analyses and implications on Roche Sauterre basanite body and Sapat olivine
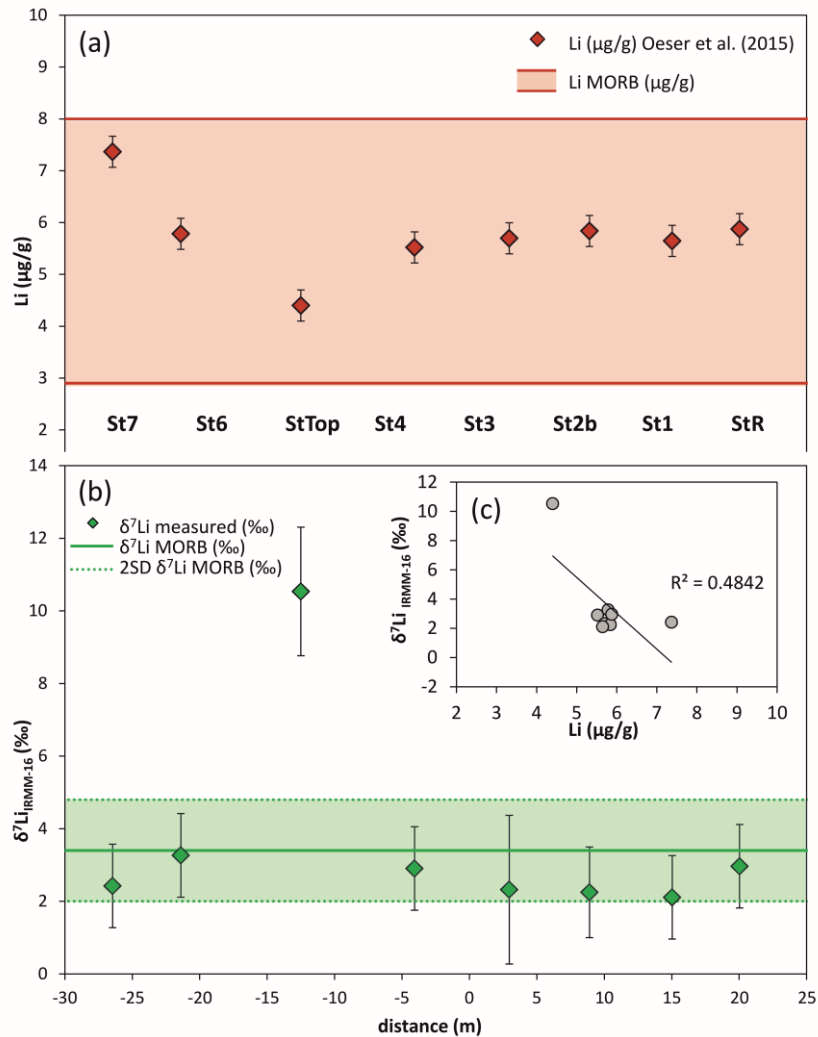
Figure 2.5: (a) Lithium concentrations from (Oeser et al., 2015) with the range of MORB concentrations (Ryan and Langmuir, 1987) and (b) δ⁷Li-values (this study) with MORB isotopic compositions (Tomascak et al., 2008) plotted against distance in the outcrop of Roche Sauterre (c) correlation of δ⁷Li and Li concentration, samples St7 and StTop do not correlate with the other samples.

2.6 Discussion

The difference between LA-MC-ICP-MS and solution MC-ICP MS of the Sapat olivine is significant outside analytical uncertainties (Steinmann et al., 2019). Accordingly, it likely is related to properties of the sample itself. The olivines from Sapat are suspected to have a hydrothermal origin and they occur in paragenesis with serpentinite, magnetite, Mg-rich chlorite and ferritchromite and chromite Inclusions are found to be supposedly magnetite and hairy ludwigite (magnesian-iron borate) (Jan and Khan, 1996), these microscopic inclusions can be observed (Figure 2.6). A lighter Li proportion in the solid inclusions might not be analyzed during laser ablation analysis because the ablation crater is not deep enough to reach the inclusion minerals, or

Chapter 2: Lithium bulk isotope analyses and implications on Roche Sauterre basanite body and Sapat olivine

alternatively during bulk analysis a heavier Li proportion in fluid phase escapes the sample due to volatilization or vaporization in the sample dissolution procedure. For this purpose, analyses of the inclusions would be necessary to determine their Li isotopic composition and Li concentration as well.
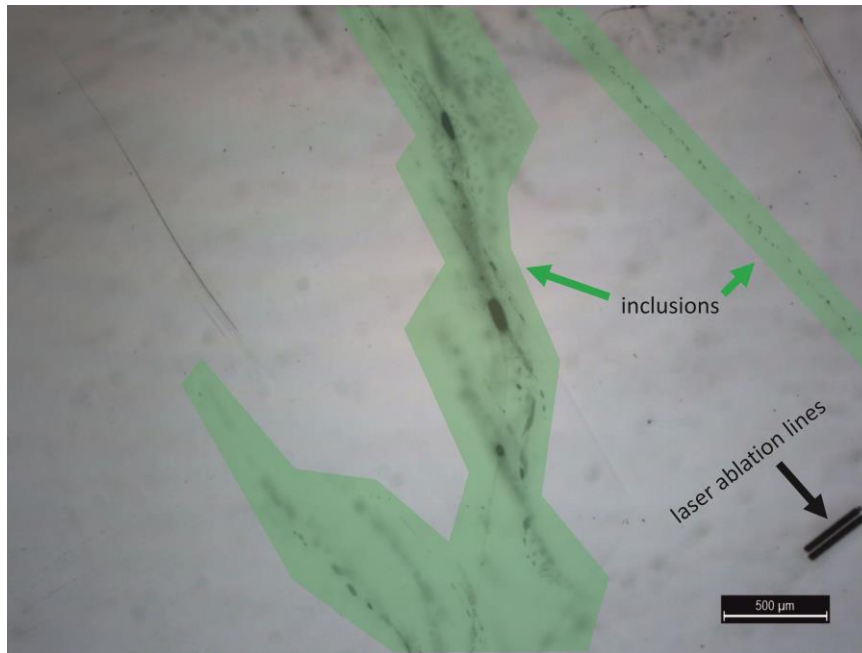
Figure 2.6: Photomicrograph of SAP olivine with visible inclusions (green shaded area) in the olivine matrix. Scale bar in the lower right corner equals 500 μm.

The Roche Sauterre samples have been analyzed in order to address two questions. The first aim is to assess the difference between whole rock and matrix. This has been done for two samples, and both samples show that the matrix shows a tendency towards being isotopically slightly heavier than the whole rock (Figure 2.7). This indicates that the olivines which have been extracted from the matrix contain a larger proportion of ^6Li than the whole rock, resulting in depletion of ^6Li in the matrix, likely driven by diffusion of Li into the olivine grains.
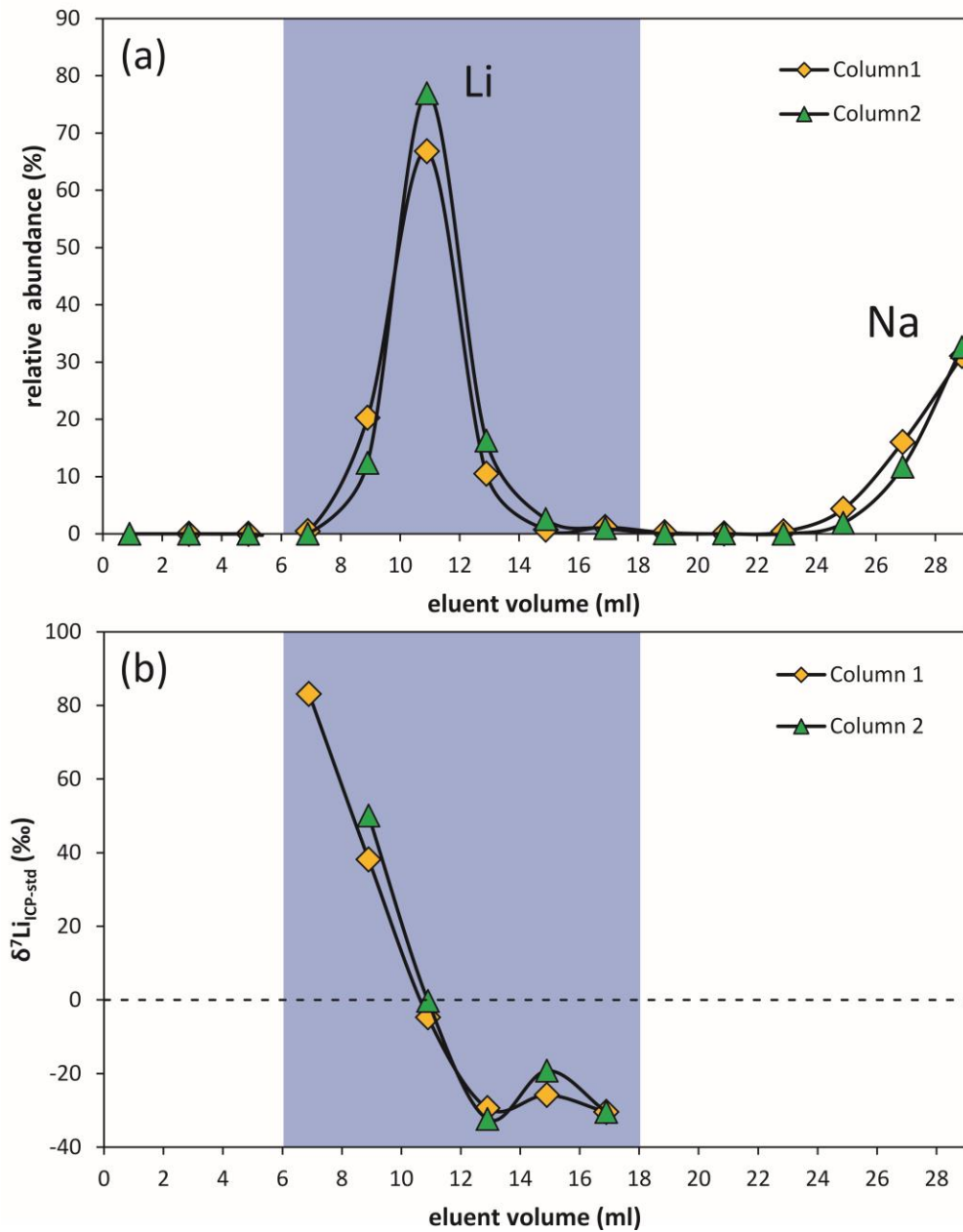
## Chapter 2: Lithium bulk isotope analyses and implications on Roche Sauterre basanite body and Sapat olivine
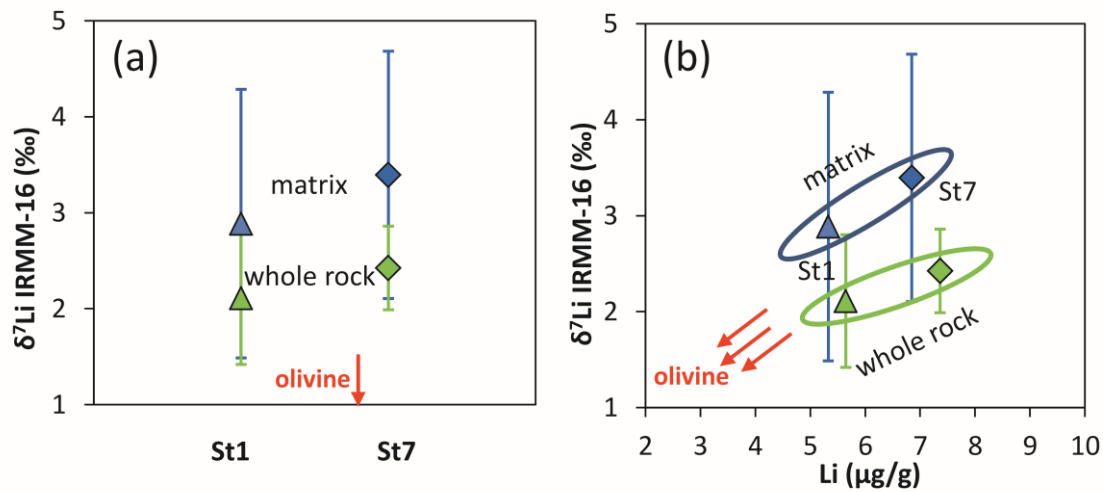
Figure 2.7: Matrix and whole rock data compared of samples St1 and St7 with error bars (1 SD).

The second aim is the analysis of variations of the Li isotope composition on the outcrop scale. Over a distance of 60 m no correlation of Li concentrations and δ^7Li is observed. For sample StTopWR the δ^7Li value is significantly different from the other measured δ^7Li. This sample has been taken at the top of the lava flow about 20 m above the bottom of the outcrop (Figure A.2.2 in the appendix) whereas all other samples have been taken at bottom level. Furthermore this sample has the lowest Li concentration. The exposure of this point of sampling might rather show a post-magmatic metasomatic event, weathering or degassing which changed the isotopic composition of this sample compared to that of the others. These three possible processes of a change in Li concentration and isotopic composition are evaluated here briefly. A metasomatic event with a Li-enriched fluid would increase the Li concentration and presumably modify the isotopic composition towards lower values (Seitz et al., 2004). Sample StTopWR, however, yields a lower Li concentration which is contradictory to the assumption of a metasomatic event. Metamorphism in a contact aureole can decrease Li concentrations with increasing metamorphic grade but they do only show limited variations in δ^7Li (Teng et al., 2007a). During chemical weathering of silicic rocks and the formation of secondary minerals ^{6}Li preferentially partitions into the newly formed minerals and ^{7}Li partitions into the associated water which would produce a regolith with low δ^7Li and not as observed here with a rather high δ^7Li (Wunder et al., 2007; Millot et al., 2010). Rudnick et al. (2004) found that in weathered saprolites from South Carolina decreasing δ^7Li with increasing degree of weathering and Li depletion of the rocks.

Chapter 2: Lithium bulk isotope analyses and implications on Roche Sauterre basanite body and Sapat olivine

Microscopically and as observed in the trace element content of the sample there is no hint for stronger weathering than for the other samples in this suite except from a slight depletion in Li concentrations. Due to the volatility of Li and the position of the sample StTopWR on the top of the lava flow a degassing process can be suspected. During degassing the melt is depleted in Li (Kuritani and Nakamura, 2006; Vlastélic et al., 2011; Cabato et al., 2013), consistent with the low Li concentration observed for StTopWR. There is currently no experimental data available regarding the Li fractionation between vapor and melt but it is known that ^{7}Li preferentially fractionates into the fluid phase (Webster et al., 1989; Wunder et al., 2006; Wunder et al., 2007), accordingly it is probable that with segregation of fluids from the melt Li is transferred to the fluid and during degassing to the vapor phase (Schiavi et al., 2010). Hence, the δ^7Li values would be expected to decrease because of the preferential partitioning of ^{7}Li into the vapor phase and leave a light vapor-differentiated rock, which is only the case for low-temperature degassing (Vlastélic et al., 2011). High-temperature leaching of Li does not significantly fractionate Li isotopes (Beck et al., 2004), an obvious fractionation of Li isotopes in the residual melt would only be the case if Li was almost completely removed into the vapor phase which is not even the case for highly evolved melts (Schiavi et al., 2010). As the isotopic composition is behaving contradictory to what would be expected from the processes described above a slight Li loss in column chemistry is suspected. Due to the large fractionation in the column a small amount of eluent lost can result in a relatively large underestimation in δ^7Li.

2.7   Conclusion

The column separation method has been established successfully, and Li can be separated from Na in a basaltic, basanitic and olivine matrix with a recovery rate of 93.8 %, 99.4 % and 96.9 %, respectively. Bulk Li isotope ratios and δ^7Li values for eleven samples have been determined. The Roche Sauterre samples overlap the range of measured continental volcanic rocks measured by other authors, and no spatial change of δ^7Li in the unweathered values on the outcrop scale has been determined. Matrix δ^7Li values without phenocrysts of olivine and pyroxene tend to be slightly lighter than the whole rock measurements, thus suggesting diffusion of light Li into the phenocrysts. The result of the sample StTopWR with higher δ^7Li and lower Li concentration

Chapter 2: Lithium bulk isotope analyses and implications on Roche Sauterre basanite body and Sapat olivine

compared to the other samples in combination with the location of the sample at the top of the lava flow and on the landscape surface points to a post-magmatic change in δ^7Li or lost fraction in the chromatographic separation procedure and not a magmatic Li isotope signature in the lava flow.

Dissertation of Lena Steinmann

Chapter 3: Indications of the eruptive history of volcanoes in zoned olivine crystals with respect to Fe-Mg, Li and other trace element concentrations and Li isotopes

Chapter 3: Indications of the eruptive history of volcanoes in zoned olivine crystals with respect to Fe-Mg, Li and other trace element concentrations and Li isotopes

~ 30 % of the olivine EMPA analyses in Chapter 3 have been performed by M. Oeser-Rabe

3.1 Abstract

Major element concentration profiles across 137 chemically zoned olivine crystals from two geotectonic settings (ocean island and island arc) have been acquired. Thereof, 63 crystals showing chemical zoning regarding Mg# have been investigated for 22 trace and minor elements. Four zoning types from normally to complexly zoned regarding Mg# have been found in both sample sets and a systems analysis of the forsterite reservoirs shows that several melt reservoirs in a volcanic plumbing system can be interconnected and that the passage way of crystals can be retraced. In the systems analysis Li concentrations have been considered as well. They do widely mirror the forsterite reservoirs, however, the differences are less clear due to the lower concentrations of Li (1.7 µg/g to 7 µg/g) compared to Mg and Fe in the wt% range. Comparative diffusivity modeling showed that Li diffuses 1.4 – 2.5 times faster than the diffusion couple Mg-Fe which is significantly less than that determined in most experimental determinations. In addition to the relative determination of Li diffusivities Li isotope profiles have been determined. These profiles also mirror the complex zoning which can be observed in Mg# and trace elements. Modeling with the beforehand determined diffusivities from chemical zoning is in good agreement with the measured Li isotope profiles.

Chapter 3: Indications of the eruptive history of volcanoes in zoned olivine crystals with respect to Fe-Mg, Li and other trace element concentrations and Li isotopes

3.2 Introduction

Chemical zoning in magmatic minerals may develop due to two end-member processes: differentiation and subsequent crystal growth or diffusive re-equilibration of initially homogeneous minerals. Processes such as crystallization of magmas, mantle melting and metasomatism can be deducted from the minor and trace element content in igneously developed olivine and conclusions on the parental magmas can be drawn (e.g. Foley et al., 2011; Foley et al., 2013; Ammannati et al., 2016). Olivines are formed in a mantle domain or in a magma chamber in a plumbing system under conditions (pressure, temperature, oxygen fugacity etc.) which cannot be observed directly. On Earth's surface the preserved zoning only can give clues to the original conditions in which a crystal has formed. Olivines might have passed through numerous magmatic environments and multistage processes might have occurred and changed their composition. This is observed in fluid-inclusions (e.g. Hansteen et al., 1998) and zoning in crystals regarding Mg# (e.g. Kahl et al., 2011; Kahl et al., 2013; Albert et al., 2014; Kahl et al., 2015) and furthermore also in trace elements such as Ni (e.g. Oeser et al., 2018). Plateau regions with constant composition within one crystal are hence deducted as the representation of a melt reservoir with a constant composition and conditions. The region between the plateaus where concentrations are adjusting and gradients are smoothing out is identified as diffusive exchange between two compositions (e.g. Costa et al., 2008).

The conception of a single magma chamber beneath a volcano is being more and more replaced by the perception of a dynamic plumbing system which consists of several melt reservoirs that might contain varying melt compositions and crystals might record signals of these magma lenses during their migration through the plumbing system (Kahl et al., 2011). During the process of migration the surrounding conditions in which the crystals are located might not be in equilibrium with them and hence, diffusive mass transport of elements in and out of crystals is triggered. Melt inclusions as well as intra-mineral chemical differences may re-equilibrate by lattice diffusion of trace elements during the timespan over which the host mineral is situated in environmental circumstances which allow for diffusive exchange (Spandler et al., 2007; Spandler and O'Neill, 2010). Presumably, the diffusion rates of some of the trace elements investigated here are differing by some orders of magnitude from each other indicating

Chapter 3: Indications of the eruptive history of volcanoes in zoned olivine crystals with respect to Fe-Mg, Li and other trace element concentrations and Li isotopes

the possibility to reveal processes of different durations in olivines (Lynn et al., 2018). Elements with high diffusion velocities such as Li may display short-lived magmatic processes from hours to days (Dohmen et al., 2010; Richter et al., 2017). Elements with moderately quick diffusion velocities such as the diffusion couple Mg-Fe or minor elements like Ni, Mn, Ca can unravel processes with durations of weeks to years, e.g. magma storage or mixing (Petry et al., 2004; L. A. Coogan et al., 2005; Dohmen et al., 2007; Dohmen and Chakraborty, 2007; Holzapfel et al., 2007). Chromium has experimentally been determined to be moderately quick, comparable to Mg-Fe (Jollands et al., 2018) but under natural conditions the diffusivity has been found to be slower (Ito and Ganguly, 2006). In their study determining diffusion coefficients in an experiment with a synthetic silicate melt introduced into San Carlos olivine Spandler and O'Neill (2010) deducted diffusion coefficients for the divalent cations Ca, Ni, Co and Mn which can substitute for Mg^{2+} and Fe^{2+} in the olivine structure and find their results in good agreement with the publications mentioned before. As Li diffuses through olivine influenced by different mechanisms depending on the concentrations induced at the crystal surface (Dohmen et al., 2010) the diffusivity of Li has to be distinguished carefully. Dohmen et al. (2010) estimated Li diffusion to be one order of magnitude faster than Fe-Mg inter-diffusion at a surface concentration of 10 µg/g, but in natural studies this rate appears to be lower with 1.6 to 2.6 relative to D_{Mg-Fe} depending on the crystallographic axis (Qian et al., 2010). The dependence on crystallographic orientation is not that clearly distinguished in other studies (Dohmen et al., 2010; Richter et al., 2017). A comparison to Li isotope diffusion and Mg# chemical zoning might complete the picture to reveal multi-stage magmatic processes. Not only Li as a trace element but also its isotopes can give valuable information on diffusive processes. As described in Chapter 1 of this dissertation Li has two stable isotopes (^{6}Li and ^{7}Li) with the light isotope diffusing faster and hence, at a diffusive flux into a crystal ^{6}Li will be enriched in the diffusion affected area of the crystal relative to ^{7}Li (Richter et al., 2003; Dohmen et al., 2010; Richter et al., 2017).

In this study the conception of trace element and minor element distribution in chemically zoned crystals regarding Mg# shall be broadened and olivines from two natural locations will be compared. These two sample locations, an arc-magmatic and an oceanic intra-plate setting, have been investigated in order to reveal if they are similar in processes despite their diverse geotectonic setting. For this purpose the Mg-Fe

Chapter 3: Indications of the eruptive history of volcanoes in zoned olivine crystals with respect to Fe-Mg, Li and other trace element concentrations and Li isotopes

zoning in the crystals will be modeled and thereon relative diffusivities for other trace elements, with a special focus on Li will be calculated on the base of (Qian et al., 2010) and (Oeser-Rabe, 2015). Furthermore, Li isotopes will be measured and the hypothesis of the calculated diffusivities will be checked, if they coincide with the Li isotope profiles.

3.3 Samples

Klyuchevskoy volcano is a subduction-related island arc volcano at the western shore of the Kamchatka peninsula (Russia). The composition corresponds to a high Mg-basalt in the more primitive and a basalt enriched in Al in the more differentiated stages (Kersting and Arculus, 1994; Ariskin et al., 1995). Eighty-six olivine crystals in samples of five vents have been investigated (F-cone, E-cone, Bulochka, Bilyukai and Levashova) for their Mg# zonation, thereof 29 crystals in three sets have been investigated for trace elements (F-cone, E-cone and Bilyukai). Furthermore, one sample from F-cone has been investigated for its Li isotopic composition.

Samples from the volcanic island Tenerife in the Canary volcanic island range (Spain) have been investigated, they originate from a fissure eruption in the north-east rift zone and will be addressed as SFA sample suite here. The fissure eruption consists of three cones which have been sampled (Siete Fuentes, Fasnia, Arafo) and 51 olivine crystals have been investigated regarding Mg# zonation. Thirtyfour crystals from Siete Fuentes and Arafo cone have been investigated regarding trace and minor element concentrations and two crystals from Arafo have been investigated for Li isotope composition. The three monogenetic basanitic eruptions took place sequentially in the above-listed order from December 1704 until February 1705 (Albert et al., 2014), so they are an example for relatively recent intra-ocean plate volcanism. Albert et al. (2014) revealed a mixing history of several magmas as they found olivine populations with various core compositions (Fo =79-80. Fo =81-82, Fo = 83-84 and Fo = 85-87 with Fo = Mg/(Mg+Fe)*100). These olivines were transported within the plumbing system and an early mixing of two relatively evolved magmas occurred at shallow depths one year prior to eruption according to their modeling results regarding Mg-Fe diffusion. Two more primitive magmas mixed in a deeper level two months prior to eruption, and

finally two weeks prior to eruption a mixing event occurred between the deeper and the shallower magmas in the course of magma upwards migration (Albert et al., 2014).

3.4 Methods

3.4.1 Major elements

The determination of major elements (Al, Mg, Si, Ca, Mn, Fe, Ni, Na) has been performed by electron microprobe analysis (EMPA) with a Cameca SX-100 at the Institut für Mineralogie, Leibniz University Hannover, in order to be able to distinguish chemically zoned olivine crystals with respect to Mg#. All analyses have been performed with an acceleration voltage of 15 kV, a beam current of 20 nA and a focused beam. The reference materials applied were Kyanite MAC for Al, Wollastonice MAC for Si and Ca, Fe_2O_3 for Fe, Mn_3O_4 for Mn, MgO for Mg, NiO for Ni and Jadeite MAC for Na. As internal standards MongOL (new reference material for *in situ* micro analysis from mantle peridotite xenolith in a basaltic breccia from Shavaryn-Tsaram, Tariat region, Central Mongolia) (Batanova et al., 2019) and San Carlos olivine (Jarosewich et al., 1980) have been measured. Matrix corrections were performed using the PAP method (Pouchou and Pichoir, 1991). Profiles from rim to core of suitable olivine crystals have been measured with measurement spot lines perpendicular to the crystal rim in order to avoid 3D effects and measure only one growth zone of the crystals at a time.

3.4.2 Trace elements

Trace element compositions have been analyzed by fs-LA-SF-ICP-MS where samples were introduced to the mass spectrometers *in situ* by laser ablation. A femtosecond laser based ablation system (Spectra-Physics Solstice) is coupled to a multi collector-ICP-MS (Thermo-Scientific Neptune Plus) at the Leibniz Universität Hannover, Germany (a more detailed description can be found in Chapter I). The ablation beam has a pulse duration of ~100 fs and wavelength of 194 nm which is generated via frequency conversion from an infrared beam with 775 nm wavelength in an in-house built mirror and lens system and focused on the sample surface via a modified New Wave (ESI)

Chapter 3: Indications of the eruptive history of volcanoes in zoned olivine crystals with respect to Fe-Mg, Li and other trace element concentrations and Li isotopes

stage combined with an optical microscope (Horn et al., 2006; Horn and von Blanckenburg, 2007). For trace element analysis the laser system is coupled to a Thermo Fisher Scientific Element XR. The laser spot size for sample ablation was ~30 µm on olivine and the laser repetition rate was 25-29 Hz. For each measurement the background has to be accounted for, this happens by measuring a 40 s background acquisition before starting the ablation for sample acquisition with an ablation interval varying with the length of the profile to be measured. The profile lines measured beforehand by electron microprobe have been consequently followed by the laser ablation line again to grant for the measurement of the exact same spot on the sample. Constant profiles in lines arranged perpendicularly to the rim have been measured with a laser scan speed of 2 µm/s in order to gain a time resolved profile which is later processes by data evaluation with LAMTrace (Jackson, 2008). For external standardization the SiO_2 (wt%) values measured by electron microprobe have been utilized because they are constant over the profile length. The basaltic glass BCR-2G was measured as internal reference and BIR-1G was measured as "unknown" sample to check if intensities are measured correctly. The line scan mode of a constant line and integration over time allows to save time and space on the sample likewise which is important regarding the analysis of isotope profiles (Figure 3.1).

The Element XR ICP-MS was equipped with Ni "Jet" sample cone and a Ni "X" skimmer cone as this combination was found to yield the best signal-to-noise-ratio for Li. The system was tuned to maintain low oxide production levels (<0.5 % ThO). Lithium background levels were monitored additionally and constantly below 3000 cps with the applied system setup. The limit of detection (LLD) for each analysis is automatically calculated by LAMTRACE applying the algorithm developed by Longerich et al. (1996). During the analytical session (1 day) the reproducibility of the measured element concentrations in BIR-1G (measured as "unknown") which was calibrated with BCR-2G (internal reference) is typically below 5 % (RSD) for Li and most other trace element measured except from P (<19 %, RSD), Cr (13 %, RSD), REE (<10 %, RSD) and Na (<6 %, RSD). A list of all measured trace elements and their analytical uncertainties can be found in the appendix (Table A.3.1).

Chapter 3: Indications of the eruptive history of volcanoes in zoned olivine crystals with respect to Fe-Mg, Li and other trace element concentrations and Li isotopes
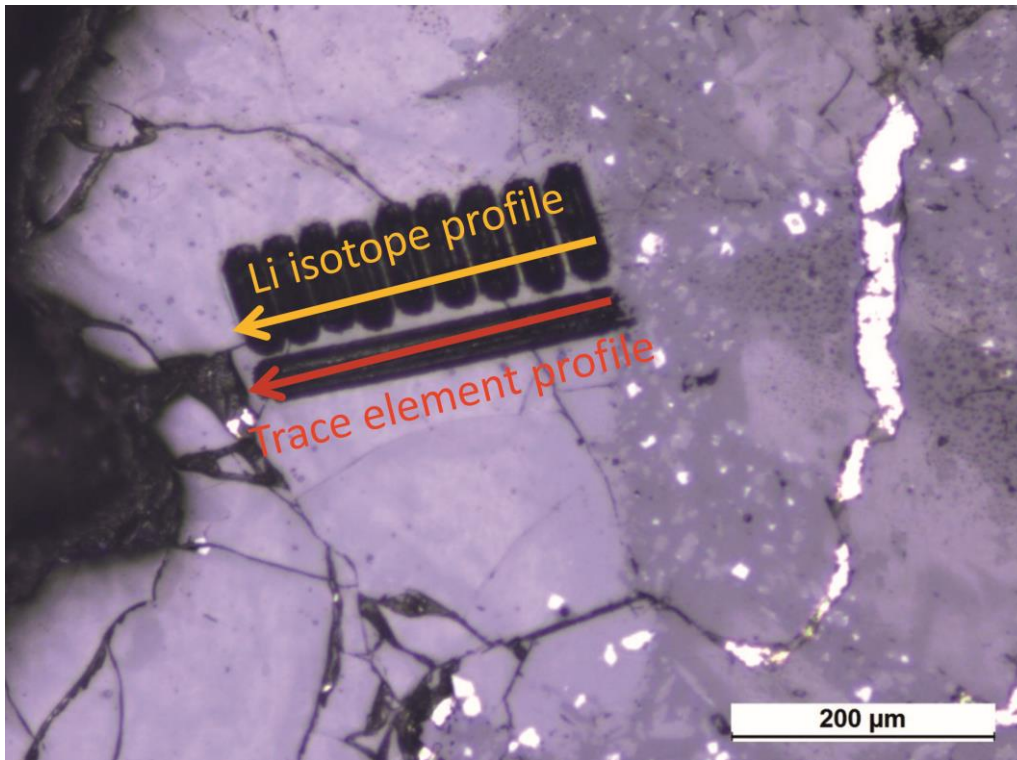
Figure 3.1: Laser ablation profiles for trace element measurements and Li isotope analysis on olivine crystal MP-KL-4-3_ol8.

3.4.3 Lithium isotopes

Lithium isotope measurement procedure was applied according to Steinmann et al. (2019) with relatively cool plasma conditions (900 W) in order to avoid matrix ionization in the plasma. *In situ* Li isotope ratio measurements were performed in static mode at low mass resolution which is sufficient to resolve atomic interferences. In order to keep background Li signals low the measurements were performed under dry plasma conditions. The sample aerosol mixture is homogenized to increase signal stability and for the detection of ^{7}Li a slow response 10^{13} Ω amplifiers coupled to a faraday cup is deployed in combination with a secondary ion multiplier for the detection of the less abundant ^{6}Li and. Due to the slower signal response a so-called *tau* correction (Kimura et al., 2016) is applied during data evaluation. All measurements were performed using standard-sample-bracketing to account for instrumental mass bias drift using the komatiitic MPI DING reference glass GOR132-G as bracketing standard according to Eq. (3.1) and recalculated to IRMM-16 (see also Chapter 1 of this dissertation and Steinmann et al. (2019)).

Chapter 3: Indications of the eruptive history of volcanoes in zoned olivine crystals with respect to Fe-Mg, Li and other trace element concentrations and Li isotopes

$$\delta\ ^{7}Li = \left[\frac{\left(\frac{^{7}Li}{^{6}Li} \right)_{sample}}{\left(\frac{^{7}Li}{^{6}Li} \right)_{GOR132-G}} - 1 \right] \times 1000 \qquad\qquad \text{Eq. (3.1)}$$

Measurements of the bracketing standard were performed in raster ablation mode, while the olivine profiles were measured in line ablation mode with lines arranged parallelly to the crystal rim (Figure 3.1). Individual measurements consist of 180 cycles with an integration time of 1.049 s. The first ~35 cycles were used for background correction measuring only the gas blank without a laser ablation signal. This was followed by ~130 cycles of sample ablation. The MPI DING reference glass T1-G ($\delta^{7}Li$ = 1.6-2.4 ‰, (Jochum et al., 2006; Le Roux, 2010; Xu et al., 2013)) has been measured over a period of 22 month with $\delta^{7}Li$ = 0.4 ‰ with a long term reproducibility of 2.1 ‰ (2 SD for n=64 in 16 sessions)(Steinmann et al., 2019).The measurement profile has been placed as lines of ~100 µm length parallel to the crystal rim like the electron microprobe and trace element analyses but in order to get a sufficiently good signal it is necessary to measure a number of lines parallel to the crystal rim which are stacked. This is necessary due to the low concentration of Li in the samples in order to achieve a stable signal over the duration of a measurement. Data evaluation is performed with a modified sheet of the LAMTool by Jan Kosler.

3.4.4   Systems analysis approach

In their studies (Kahl et al. (2011; 2013; 2015) applied a systems analysis approach to identify magma reservoirs with the aim of understanding the complexity of the plumbing system of Mt. Etna which shall be transferred to the Klyuchevskoy and Tenerife's SFA eruptions here. A system is defined as a combination of elements that act together in order to accomplish an objective. The aim of analyzing a system is to understand how the elements in a system are interconnected and how they are influencing the overall behavior of the system (Palm, 2005). Transferring this information derived from electro-mechanical systems to a geochemical system, namely a magma plumbing system, melt reservoirs have to be identified as elements of the

Chapter 3: Indications of the eruptive history of volcanoes in zoned olivine crystals with respect to Fe-Mg, Li and other trace element concentrations and Li isotopes

system and interconnections between those elements have to be defined to visualize the interaction between the reservoirs. Various compositional plateaus from the core to the rim of the crystals analyzed here are not produced by simple fractionation during crystal growth (e.g. Costa et al., 2008), but each plateau composition represents a growth episode in a chemically distinct magmatic environment (Kahl et al., 2011). Hence, neighboring plateaus display the transfer of the crystals from one compositional environment to another in case that growth rates are faster than the passage of the crystals through the environments (Ruprecht et al., 2008). In order to receive a time chain of events the assumption is made, that the rim composition mirrors the youngest growth episode (latest event, e.g. preceding eruption) and progressingly from rim to core the growth episodes are older, mirroring preceding events (Kahl et al., 2011). In the systems analysis diagrams the interaction of the magmatic environments and pathways from one magma reservoir to another are displayed, no special software was used for this but logical summarization of the melt reservoirs/plateau compositions.

3.5   Results

3.5.1   Mg-Fe zoning

Olivines from Klyuchevskoy volcano (Kamchatka) comprise olivines which show multiple zoning with respect to Mg#. This might indicate the transport of olivine crystals between magma chambers (Kahl et al., 2011). The classification of olivine crystals has been performed regarding the zonation in Mg# and four types of zoning have been identified. Normally zoned crystals (A) are characterized by a Mg-rich core and a Fe-rich rim, complexly zoned crystals with a mantle region (B) are characterized by a mantle which is more Fe-rich than the core and a rim which is more Fe-rich than the mantle. Complexly zoned crystals (C) have a more Mg-rich mantle and a more Fe-rich rim than the core and reversely zoned crystals (D) have a Fe-rich core and Mg-rich rim (Figure 3.2). The distribution of the zonation patterns is (A) 36.0 %, (B) 47.7 %, (C) 11.6 % and (D) 2.3 %. There are only two profiles which are classified as D, both have been ejected by the E cone. The F-cone yields the most primitive core compositions with Fo_{91} to Fo_{87}. Bulochka olivines display similar core compositions whereas some crystals have a core composition around Fo_{85}. The E-cone and Bilyukai comprise

Chapter 3: Indications of the eruptive history of volcanoes in zoned olivine crystals with respect to Fe-Mg, Li and other trace element concentrations and Li isotopes

mostly Fo_{79-82} and some Fo_{89} crystals. Levashova shows the lowest core compositions in this sample suite with Fo_{79-81}.
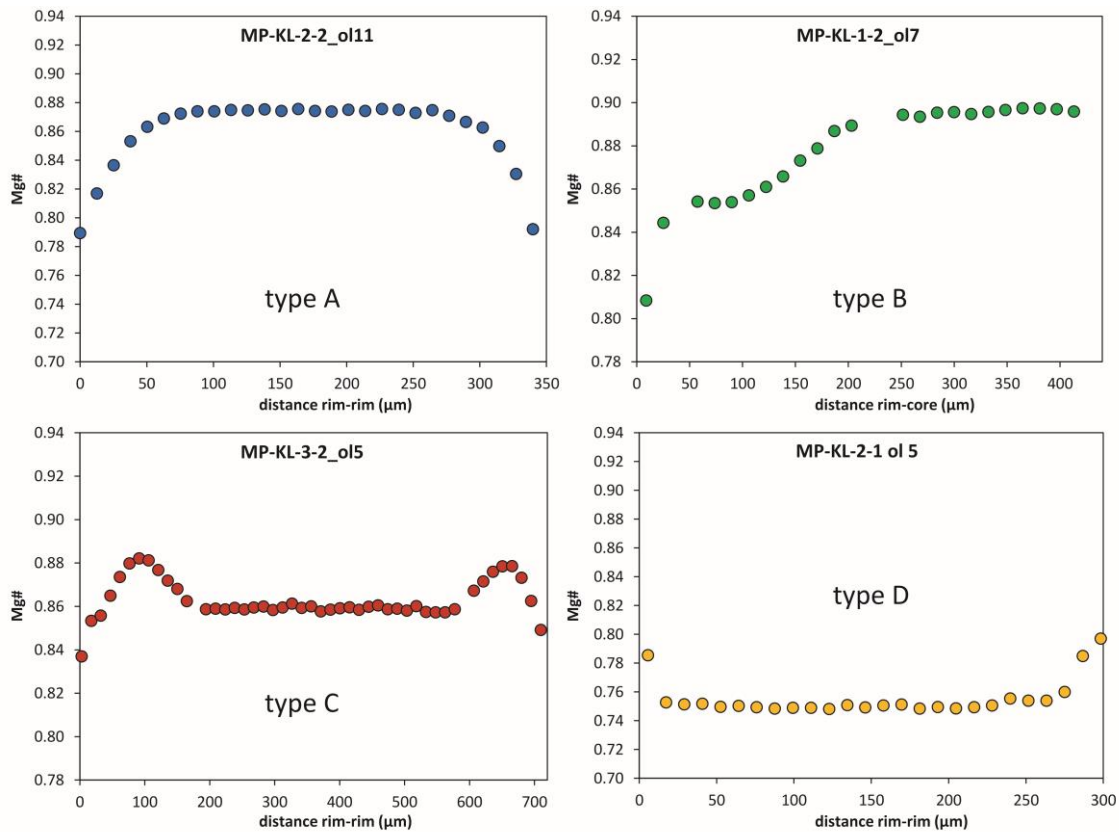
Figure 3.2: Exemplary profiles for the zoning types found in olivines from Klyuchevskoy (A) normally zoned (from rim to rim) (B) complexly zoned (Mg rich core) (from rim to core) (C) complexly zoned (Fe-rich core) (from rim to rim) and (D) reversely zoned (from rim to rim).

Olivines from the Arafo volcano (Tenerife) consist of three populations in general (Albert et al., 2014) which has been widely reproduced here with 16 olivines, whereas the two populations with the core composition Fo_{79-80} and Fo_{81-82} could not be distinguished that clearly and olivines with Fo_{80-81} have been found as well. The population with Fo_{85-87} could clearly be distinguished though and a rare proportion of Fo^{83-84} has been found. Fo_{83-84} is more frequently found as mantle zone of the olivines. The above described zoning patterns (types A through D) can be found in the SFA olivines as well, even if not that strongly pronounced (Figure 3.3). The complexity of the Mg-Fe zoning has also been observed by Albert et al. (2014). Abundances are as follows (A) 19.6 %, (B) 11.8 %, (C) 60.8 % and (D) 3.9 %. Compared to the olivines crystals from the Klyuchevskoy suite the SFA olivines are less variable regarding their

Chapter 3: Indications of the eruptive history of volcanoes in zoned olivine crystals with respect to Fe-Mg, Li and other trace element concentrations and Li isotopes

core Mg#. Most crystals fall into the populations mentioned above. Furthermore, the variability within the profiles is smaller than for the Kluychevskoy samples.
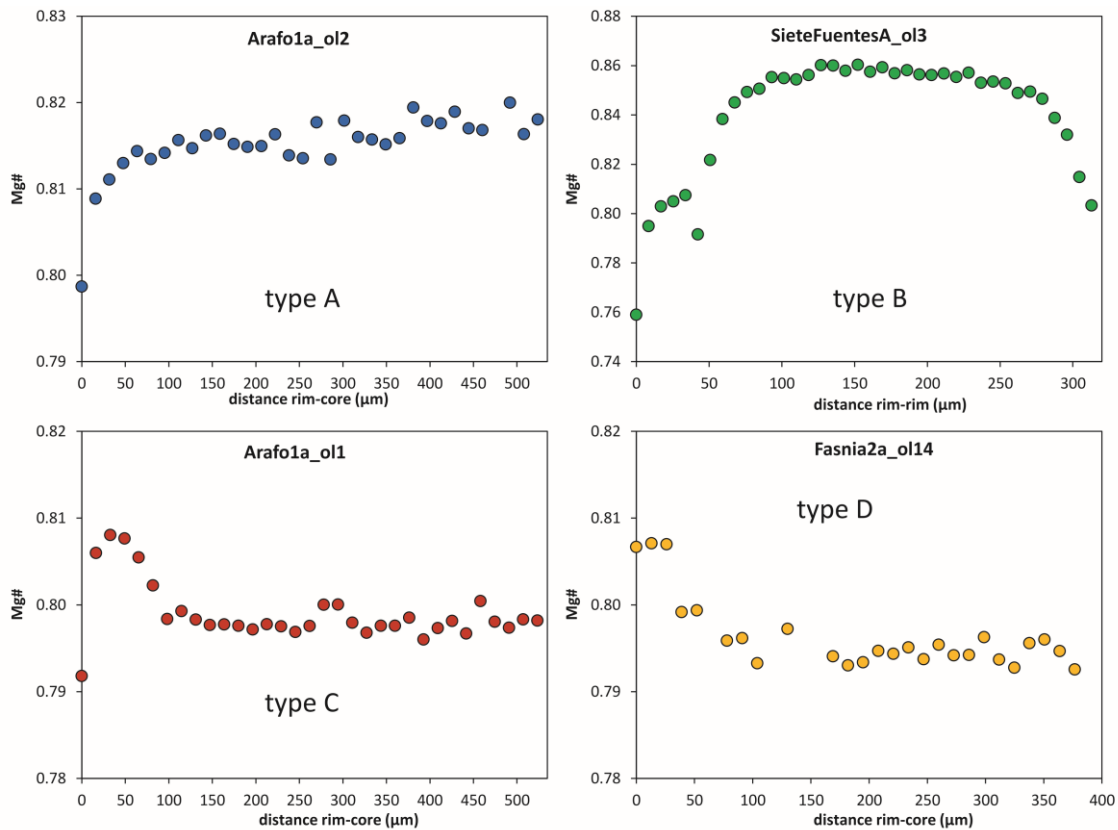
Figure 3.3: Exemplary profiles for the zoning types found in olivines from Tenerife (A) normally zoned (from rim to core) (B) complexly zoned (Mg rich core) (from rim to rim) (C) complexly zoned (Fe-rich core) (from rim to core) and (D) reversely zoned (from rim to core). Except from type B the concentration variations throughout the profiles are not as pronounced as in the Klyuchevskoy olivines.

3.5.2 Minor and trace element patterns

25 trace and major elements have been measured in 29 Klyuchevskoy and 34 SFA olivines. In the trace element patterns the complexly zoned profiles, as indicated by Mg#, cannot be observed in some cases due to the insufficient spatial resolution of the laser spot and due to too low concentration differences in the trace element profiles to resolve variations. An indication of the complexity of the zoning can be suspected by partially irregular variations in concentration.

In the Klyuchevskoy samples a clear trend of diffusion of Li into the olivine crystals is observed with rim concentrations varying from mainly 3 µg/g to close to 2 µg/g in E-cone and F-cone samples. In Bilyukai the rim concentrations of the olivine crystals

Chapter 3: Indications of the eruptive history of volcanoes in zoned olivine crystals with respect to Fe-Mg, Li and other trace element concentrations and Li isotopes

range from 5 to 8 µg/g and the core concentrations are lower with ~3 µg/g. Manganese, Co and Sc appear to diffuse into olivine with higher concentrations in the rims than in the cores whereas Cr and Ni display reverse trends of diffusion out of olivine. Lithium patterns from Arafo and Siete Fuentes olivines look different to Klyuchevskoy Li patterns, the majority displays elevated concentrations in the rim areas with decreasing Li concentrations in the Mg# mantle area and in the core with no clear distinction between mantle and core area. Klyuchevskoy olivines also display the mantle region of complexly zoned olivines but always with lower concentrations in the cores than in the mantles (Figure 3.4).
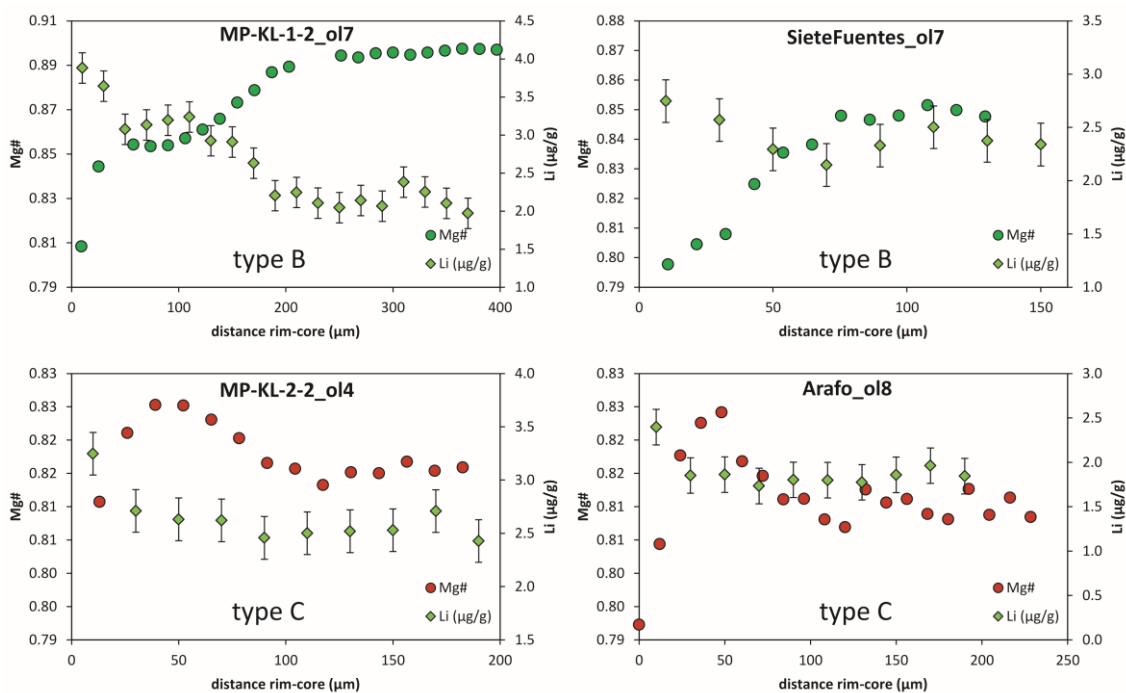
Figure 3.4: Lithium trace element zoning in relation to complex Mg# zoning in type B and type C olivines from Klyuchevskoy and SFA, error bars of Li measurements are 0.2 µg/g (2SD).

Lithium, Fe, Mn, Ca, Co, Sc, V and Y yield higher concentrations in the rims compared to the cores in most samples and hence diffusion into the crystal can be assumed. Chromium as well as Mg, Ni, Ti, and Co appear to diffuse out of the olivine (Figure 3.5). Aluminum in most cases does not show any clear indication of diffusion into or out of the crystals, variations in concentration can also be connected to inclusions in the crystals or cracks. Phosphorous profiles are very variable, in some

Chapter 3: Indications of the eruptive history of volcanoes in zoned olivine crystals with respect to Fe-Mg, Li and other trace element concentrations and Li isotopes

cases there is no variation throughout the profile, in some cases an enrichment in the rims is observed but with no clear linking to other element profiles.
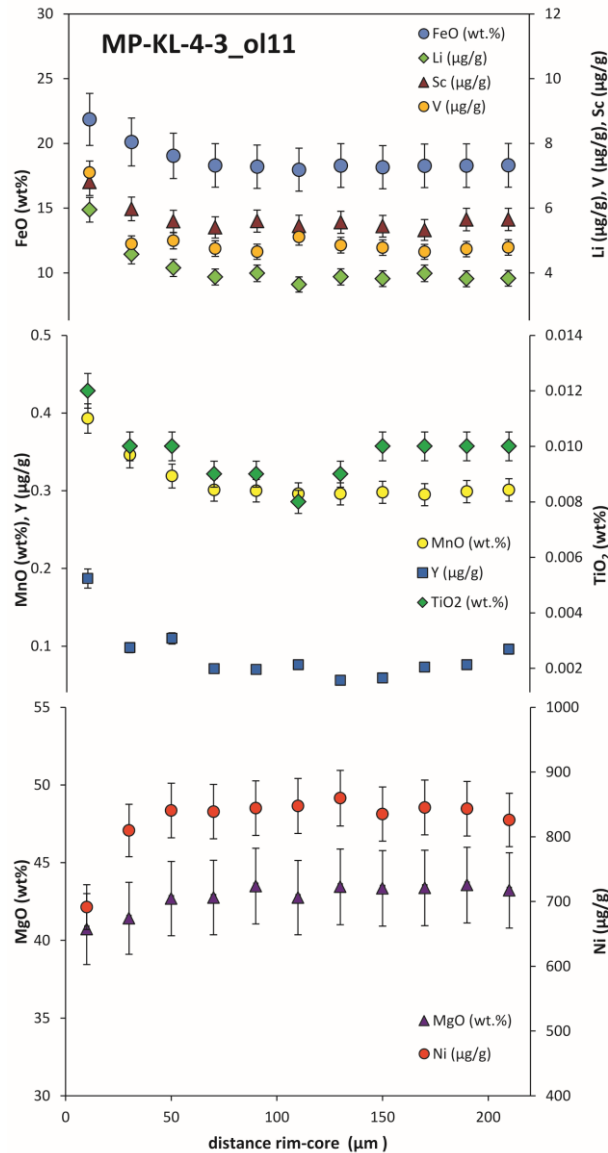
Figure 3.5: Typical trace element patterns in a normally zoned olivine from Klyuchevskoy Bilyukai, elevated concentrations of FeO, Li, Sc, V, MnO, Y and TiO₂, decreasing concentrations of MgO and Ni compared to the core.

3.5.3   Li isotopes

Lithium isotope profiles have been acquired for MP-KL-1-2 from the F-cone, for MP-KL-4-3 (Bilyukai) and Arafo volcano. Two profiles from Arafo have been measured with a δ^7Li from 6.8 ‰ to 12.5 ‰ ± 2.8 ‰ and 6.9 ‰ to 11.7 ‰ ±2.7 ‰. Results for the F-cone isotope profiles are similar with a δ^7Li value varying from 5.6 ‰ ± 3.1 ‰ to

Chapter 3: Indications of the eruptive history of volcanoes in zoned olivine crystals with respect to Fe-Mg, Li and other trace element concentrations and Li isotopes

12.1 ‰ ± 2.6 ‰. Lithium isotope profiles measured from Bilyukai have minimum δ7Li values of 3.0 ‰ ± 2.2 ‰ and maximum values of 8.4 ‰ ± 2.1 ‰. In most cases the δ^7Li value in the rim area of the crystals is lower than a point further in direction of the core for the Klyuchevskoy olivines (Figure 3.6).
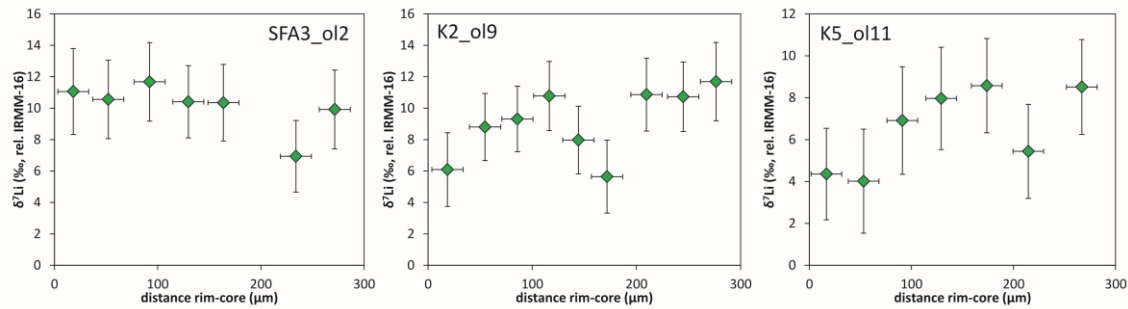
Figure 3.6: Lithium isotope profiles of Arafo olivine 2 (SFA3), Klyuchevskoy F-cone olivine 9 (K2) and Bilyukai olvine 11 (K5), horizontal error bars display the spot size of ~30 µm and vertical error bars display 2 σ of the sample-standard-bracketing of the isotope analysis.

3.6 Discussion

3.6.1 Systems analysis approach of Mg-Fe zoning to decipher magmatic evolution

Chemical zoning regarding the forsterite-content has long been thought to be a product of fractional crystallization in a larger magma chamber. This idea has been revised by many authors (e.g. Marsh 2006) and developed to a complex plumbing system with dynamically interconnected melt reservoirs in a molten region or a "crystal mush zone". Zoned minerals hence are a product of the transport of crystallizing minerals within a magma plumbing system and each plateau in the zoning pattern likely represents a distinct reservoir. This model assumes that the chemical composition did not gradually change within one large magma chamber during differentiation but rather as the result of residence and growth of the olivine crystals in different reservoirs with distinct compositions and boundary conditions. Due to the chemical gradient which develops between the original crystal and the newly overgrowing rim diffusion occurs in order to achieve equilibrium between these two crystal areas (Costa et al., 2008). The interplay of olivine growth and diffusion opens the opportunity to determine the development of a crystal through differently composited reservoirs and also the determination of timescales due to the diffusive exchange of elements. Another hint for the occurrence of

Chapter 3: Indications of the eruptive history of volcanoes in zoned olivine crystals with respect to Fe-Mg, Li and other trace element concentrations and Li isotopes

diffusive exchange between the layers of the crystals is the isotopic variation in δ^{56}Fe which is caused by Fe-Mg exchange diffusion; crystal growth and differentiation cause only negligible isotope effects on the order of 0.1 ‰ (Weyer (2008)). In the case of diffusive equilibration isotope profiles are developing which helps to determine the diffusive origin of a zoning from a growth zoning (Sio et al., 2013). Hence, Fe-Mg, and also Li isotopic zoning may be seen as evidence for diffusive exchange of a crystal with a melt or between two crystal layers with differing composition. For Klyuchevykoy's F-cone δ^{56}Fe profiles have been measured by M. Oeser-Rabe. These profiles show variations in the isotopic composition which evidence a diffusive episode during the evolution of the crystals (Figure A.3.1).

Following the systems analysis approach of Kahl et al. (2011, 2013 and 2015) possible melt reservoirs in the two sample suites are identified by grouping the zones of the olivines regarding their Fo-contents. Afterwards neighboring zones are considered reservoirs between which the olivines have been migrating and hence the melt reservoirs can be interconnected by displaying the migration paths. For both sample suites a development of the plumbing system over time can be observed from crystal migration from more primitive reservoirs (Fo_{90-91}) to more fertile reservoirs (Fo_{65-70}). The five sampled cones from Kluchevskoy volcano show a development from olivines with partly very primitive, nearly mantle-like forsterite content with Fo_{91} (Foley et al., 2013), to more Fe-rich compositions with Fo_{65}. The main reservoir appears to be Fo_{87-90} as most olivines have resided in this reservoir (Figure 3.7). The abundance of olivines with plateau regions of Fo87-90 decreases from K2 (F-cone) to K5 (Bilyukai) indicating the exhaustion of this reservoir in the advancing differentiation process in the plumbing system. Another indication for differentiation in progress is the rim compositions which are becoming more and more fertile up to Fo_{65} in K5. The reservoir Fo83-86 which is strongly interconnected with the other reservoirs from K1 to K3 is probably more exhausted and less interconnected in K4 and K5. The Klyuchevskoy lavas fractionate from high Mg to high Al basalts in decompression from high-pressure conditions and in the presence of water with increasing fayalite component in the olivines of the high Al basalts (Kersting and Arculus, 1994; Ariskin et al., 1995).

Chapter 3: Indications of the eruptive history of volcanoes in zoned olivine crystals with respect to Fe-Mg, Li and other trace element concentrations and Li isotopes
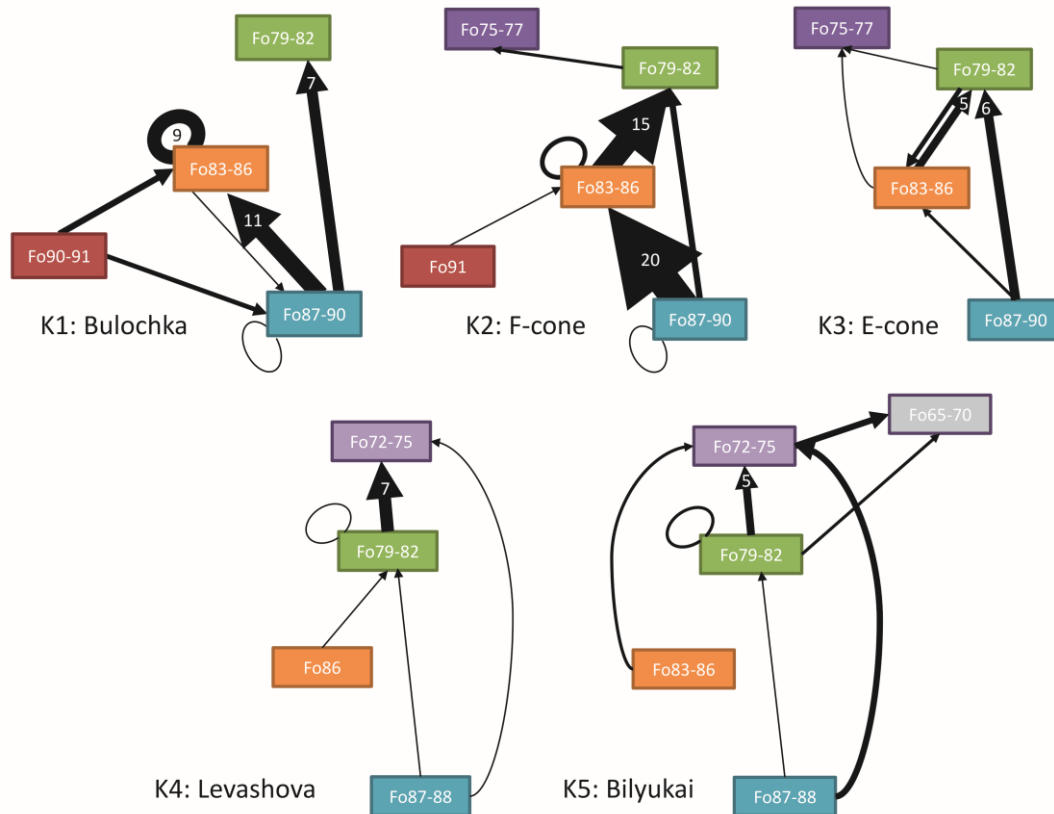
Figure 3.7: Systems analysis with migration pathways between melt reservoirs for Klyuchevskoy volcano, K1 Bulochka, K2 F-cone, K3 E-cone, K4 Levashova, K5 Bilyukai. The arrow thickness refers to the number of crystals moving between the melt reservoirs, number of crystals ≥ 5 is denoted in the figure. Oval symbols on the boxes indicate migration of crystals within one reservoir with zones that are slightly different in Fo but are still classified as the same reservoir.

The SFA fissure eruption shows a development from the first (Siete Fuentes) to the second (Fasnia) and third eruption (Arafo). Five melt reservoirs can be distinguished with interconnections between them (Figure 3.8). The interconnections of the reservoirs from the first eruption are more complex than for the last eruption. Furthermore, the abundance of the most primitive composition (Fo_{85-86}) decreases from 6 cores in SFA1 to 2 cores in SFA3. The most fractionated fraction (Fo_{76-78}) is always the terminal fraction, meaning the rim composition of the olivines. This indicates that the transport of crystals to a more fractionated magma chamber might have triggered the eruption as in general the rim compositions are more fractionated than the core compositions in most cases. The reservoir Fo_{83-84} appears to have no connection to the most mafic Fo_{85-86}, which is connected to all three other reservoirs. The transport of olivines from Fo_{85-86} to the other reservoirs decreases from SFA1 to SFA3 which points to an exhaustion of this most mafic reservoir. The pathway from Fo_{85-86} to Fo_{75-78} is not recognized in SFA2

Chapter 3: Indications of the eruptive history of volcanoes in zoned olivine crystals with respect to Fe-Mg, Li and other trace element concentrations and Li isotopes

which might indicate the temporal closure of this passage or simply the fact, that no olivines were found in this sample. Fo_{83-84} is connected to Fo_{75-78} (exhausted in SFA1), Fo_{81-82} (exhausted in SFA2), and Fo_{79-80}. The most common pathway with increasing abundance from SFA1 to SFA3 is the connection of Fo_{81-82} and Fo_{79-80}, in all three eruptions there is a reciprocal exchange of olivines between both reservoirs.
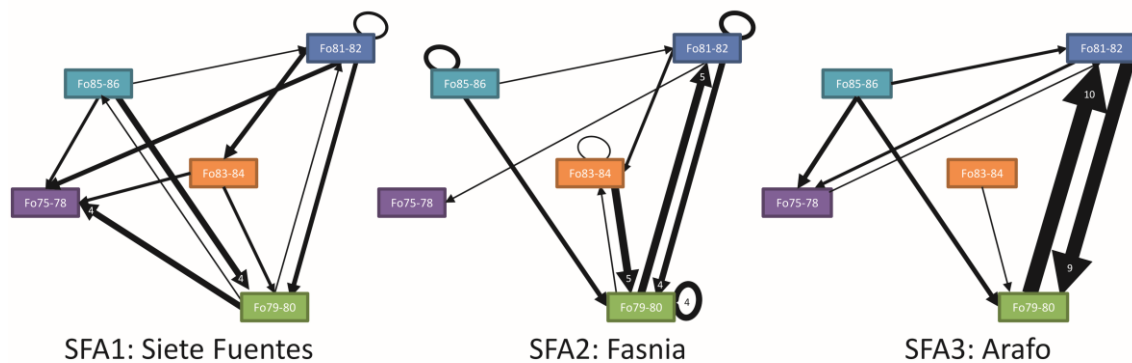
Figure 3.8: Systems analysis with migration pathways between melt reservoirs for the SFA fissure eruption from 1704/1705 in the North-East rift zone on Tenerife, SFA1: Siete Fuentes, SFA2: Fasnia, SFA3: Arafo. The arrow thickness refers to the number of crystals moving between the melt reservoirs, number of crystals ≥ 4 is denoted in the figure. Oval symbols on the boxes indicate migration of crystals within one reservoir with zones that are slightly different in Fo but are still classified as the same reservoir.

Compared to Albert et al., (2014) the mantle compositions have been taken into account and hence the transport history of the olivines occurs to be more complex. The data set of this chapter might broaden the data base for SFA olivines and might also help to further elucidate the timing of magmatic events investigated by Albert et al. (2014).

The occurrence of the zoning types mentioned above can be explained by the transport of crystals between the reservoirs which takes place not only as upward migration from more to less primitive but exchange between the melt reservoirs. This suggests the existence of various interconnected melt pockets or at least areas with a constant composition in the plumbing system of a volcano. Furthermore, Li concentrations have been compared with the forsterite content of the reservoirs. In Table 3.1 and Table 3.2 Li concentrations have been assigned to the Fo-reservoirs and show that the Li concentrations widely correspond to the trend of increasing Li concentrations with advancing fractionation due to the moderately incompatible character of Li in basaltic melts (Seitz and Woodland, 2000; Ottolini et al., 2009). A complete list of Fo and Li concentrations can be found in the appendix in Table A.3.2 and Table A.3.3. It shows

Chapter 3: Indications of the eruptive history of volcanoes in zoned olivine crystals with respect to Fe-Mg, Li and other trace element concentrations and Li isotopes

that a more primitive Fo-reservoir is concomitant with a lower Li concentration. In Klyuchevskoy, the highest Li concentrations are 7.2 µg/g in Fo_{65-70}, while in SFA the highest Li concentration is 2.7 µg/g in Fo_{75-78}. In comparison of both settings it is noteworthy that the Li concentrations in Klyuchevskoy are higher than in SFA and the spectrum of Fo-reservoirs is as well more primitive and more fertile than in SFA. The lower Li concentrations in the oceanic intra-plate setting of SFA compared to the higher Li concentrations in the island-arc setting Klyuchevskoy might be a product of the source rock from which the material is molten. In oceanic intra-plate settings the material originates directly from the mantle which is relatively primitive, unless it is influenced by metasomatism (Chan and Frey, 2003). In subduction zones volcanism is influenced by the fluid-release of the subducted plate which is enriched in Li due to the alteration of MORBs and the sedimentary cover on the oceanic plate (Elliott et al., 2006; Marschall et al., 2007a).

Table 3.1: Lithium concentrations in the zones in olivine from Klyuchevskoy F-cone, E-cone and Bilyukai measured by fs-LA-ICP-MS

µg/g	K2: F-cone			K3: E-cone			K5: Bilyukai		
	Li rim	Li mantle	Li core	Li rim	Li mantle	Li core	Li rim	Li mantle	Li core
Fo_{90-91}	-	-	1.8-2.1	-	-	-	-	-	-
Fo_{87-90}	-	2.3	2.2-2.9	-	-	2.3-2.7	-	-	-
Fo_{83-86}	-	2.7-3.5	2.7-2.9	-	2.6-3.3	-	-	-	3.4
Fo_{79-82}	2.6-3.9	-	-	2.7-4.5	2.7	2.7-2.8	-	3.7	3.4-3.8
Fo_{72-75}	-	-	-	5.9	-	5.8	-	4.3-6.7	6.1
Fo_{65-70}	-	-	-	-	-	-	4.9-7.2	-	-

Table 3.2: Lithium concentrations in the melt reservoirs in SFA1 Siete Fuentes and SFA3 Arafo measured by fs-LA-ICP-MS

µg/g	SFA1: Siete Fuentes			SFA3: Arafo		
	Li rim	Li mantle	Li core	Li rim	Li mantle	Li core
Fo_{85-86}	-	-	1.8-2.1	-	-	2.1-2.4
Fo_{83-84}	-	2	2.2	-	2.0	-
Fo_{81-82}	-	1.9-2.3	2.1-2.3	1.9	1.9-2.1	1.8-2.1
Fo_{79-80}	2.0-2.8	1.9-2.6	2.1	2.0-2.4	-	2.0-2.6
Fo_{75-78}	2.2-2.7	-	-	2.3-2.5	-	-

Chapter 3: Indications of the eruptive history of volcanoes in zoned olivine crystals with respect to Fe-Mg, Li and other trace element concentrations and Li isotopes

3.6.2 Determination of relative diffusion coefficients

The relative diffusion coefficients of various minor and trace elements and Fe-Mg in natural olivines can be estimated by applying the approach of Qian et al. (2010) and Chapter IV in Oeser-Rabe (2015). The Mg# calculated from EPMA measurements was calculated based on MgO and FeO (Mg#=Mg/(Mg+Fe)) and the concentrations of Li and other minor and trace elements was measured by fs-LA-ICP-MS. The calculation is carried out assuming one-dimensional diffusive exchange with a semi-infinite medium in the case of olivine equilibrating with a melt at a fixed surface concentration and an initially homogeneous composition (Eq. 3.2) which is based on Eqn. 3.13 in (Crank, 1975):

$$C_{semi-infinite} = C_1 + (C_2 - C_1) \times \mathrm{erf}\left(\frac{x}{2 \times \sqrt{\Gamma}}\right) \qquad \text{Eq. (3.2)}$$

For the diffusive equilibration of two layers of olivine calculations are performed with an infinite medium approach assuming the same conditions as for the semi-infinite approach (Eq. 3):

$$C_{infinite} = C_1 + \left(\frac{1}{2}(C_2 - C_1) \times \mathrm{erf}\left(\frac{x}{2 \times \sqrt{\Gamma}}\right)\right) \qquad \text{Eq. (3.3)}$$

Where C_1 represents the concentration or Mg# at the olivine surface or in the infinite rim, C_2 represents the concentration or Mg# at the olivine core, x is the distance from the rim in m and Γ represents the product of diffusion coefficient and time (D·t; e.g. Ganguly, (2002)).

Relative diffusion coefficients of trace elements can be modeled in a two-step scheme. At first the diffusion profiles of Mg# can be fitted by adjusting C_1, C_2 and Γ in Eq. (3.2) or Eq. (3.3) to receive an individual diffusion profile with adjacent characteristic Γ_{Mg-Fe}-values (Figure 3.9). In the second step the Li concentration profiles are fitted accordingly by adjusting C_1, C_2 and depending on Γ_{Mg-Fe}-values for Γ_{TE} following Eq. (3.4) assuming that the duration of the diffusive flux t is the same or very similar for all elements:

$$\frac{\Gamma_{TE}}{\Gamma_{Mg-Fe}} \cong \frac{D_{TE}}{D_{Mg-Fe}} \qquad \text{Eq. (3.4)}$$

Chapter 3: Indications of the eruptive history of volcanoes in zoned olivine crystals with respect to Fe-Mg, Li and other trace element concentrations and Li isotopes

To calculate relative diffusivities for Li D_{Li} is inserted in the equation for D_{TE} here. For Klyuchevskoy, the D_{Li}/D_{Mg-Fe}-ratios for our sample suites range between 1.4 to 1.8 and for the SFA olivines, the D_{Li}/D_{Mg-Fe}-ratios are slightly higher with 1.7 to 2.5. The mean values for all samples are listed in Table 3.3 and the complete set of results is listed in Table A.3.4 in the appendix. The application of the infinite model indicates that the process which is modeled is not the last event that has taken place because the concentration at the rim is not fitted with this model. For this purpose a semi-infinite calculation has to be applied. Both modeling stages yield the same D_{Li}/D_{Mg-Fe} (Figure 3.9).
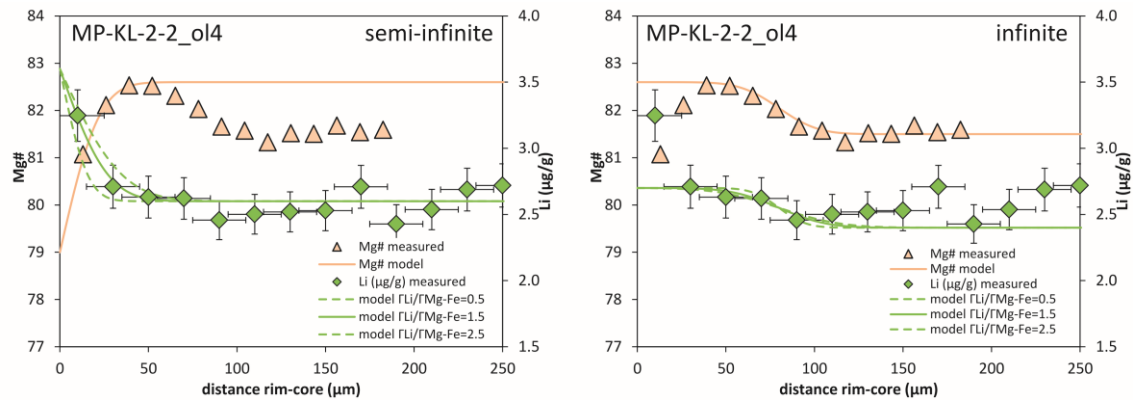
Figure 3.9: Two possible modeling scenarios, the semi-infinite approach is applied when the diffusive exchange supposedly took place between a crystal and the melt surrounding it. The infinite approach is applied for the diffusive equilibration of two subsequently formed crystal layers. Both scenarios can be applied in the same crystal and display different stages of diffusive re-equilibration but yield the same D_{Li}/D_{Mg-Fe}.

Table 3.3: Mean values and standard deviations for modeled D_{Li}/D_{Mg-Fe}, Γ_{Mg-Fe} and Γ_{Li} for the Klyuchevskoy and SFA sample suites

Sample		D_{Li}/D_{Mg-Fe}	Γ_{Mg-Fe} (m²)	Γ_{Li} (m²)
Klyuchevskoy	**MP-KL-1-2**	1.7 ± 0.7 (SD)	$6.9*10^{-10} \pm 4.1*10^{-10}$ (SD)	$1.0*10^{-9} \pm 5.1*10^{-10}$ (SD)
	MP-KL-2-2	1.4 ± 0.3 (SD)	$4.9*10^{-10} \pm 5.1*10^{-10}$ (SD)	$6.5*10^{-10} \pm 6.4*10^{-10}$ (SD)
	MP-KL-4-3	1.7 ± 1.0 (SD)	$4.0*10^{-10} \pm 2.8*10^{-10}$ (SD)	$5.6*10^{-10} \pm 2.9*10^{-10}$ (SD)
SFA	**Arafo**	1.7 ± 0.5 (SD)	$3.7*10^{-10} \pm 2.5*10^{-10}$ (SD)	$6.0*10^{-10} \pm 3.8*10^{-10}$ (SD)
	S. Fuentes	2.5 ± 1.2 (SD)	$1.5*10^{-10} \pm 1.0*10^{-10}$ (SD)	$3.3*10^{-10} \pm 2.1*10^{-10}$ (SD)

Experimental studies revealed that Li is a fast diffusing element and diffuses via vacancies on the octahedral positions ("slow" diffusion mechanism) and via interstitials in the crystal lattice ("fast" diffusion mechanism) (Dohmen et al., 2010). The authors

Chapter 3: Indications of the eruptive history of volcanoes in zoned olivine crystals with respect to Fe-Mg, Li and other trace element concentrations and Li isotopes

note that the fast diffusion mechanism is assumed not to be activated in natural systems. The diffusion coefficient for the vacancy controlled diffusion mechanism is depending on the temperature prevailing in the magma chamber (Dohmen et al., 2010). The results here show a discrepancy between such experimentally determined diffusivities and diffusivities determined in natural samples, comparatively to Mg-Fe exchange diffusion. The diffusivity of Li relative to that of Fe-Mg is reduced from one order of magnitude faster for the slow diffusion mechanism from Dohmen et al. (2010) to ~1.7 times faster (this study). The choice of diffusion coefficient will strongly change the time scales which can be modeled. This will be addressed in more detail in Chapter 4 of this dissertation.

For olivine 11 from Bilyukai cone some minor and trace elements have been modeled according to the same scheme as Li. The diffusivities relative to Mg-Fe (D_{TE}/D_{Mg-Fe} with TE as the corresponding element) are: Ni ~0.6; V ~0.8; MnO and Co ~1; Li, Sc and TiO$_2$ ~1.2; Cr and Y ~1.5. These values widely correspond to the values modeled in the studies of Qian et al. (2010) and Oeser-Rabe (2015). The modeled profiles are displayed in Figure 3.10.
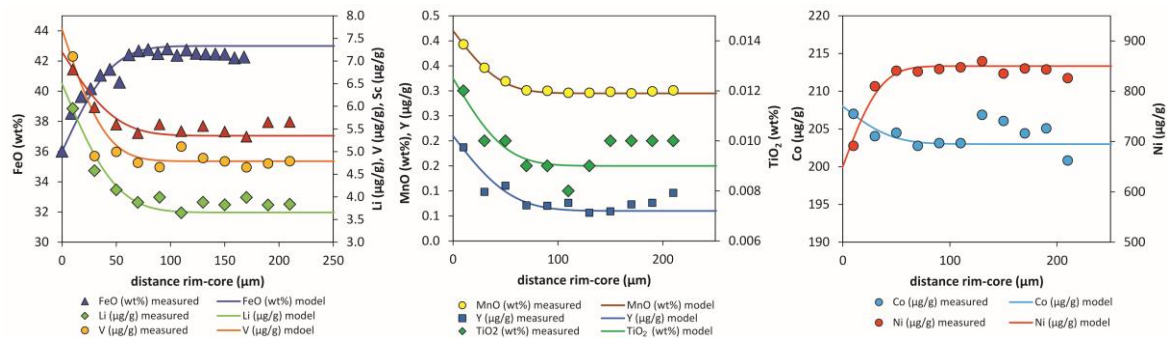
Figure 3.10: Fit of the measured and modeled diffusion profiles for FeO, Li, V, Sc, MnO, Y, TiO$_2$, Co and Ni in K5_ol11, for better visualization error bars are not shown.

3.6.3 Lithium isotope diffusion

Lithium isotope profiles have been modeled with the calculated relative diffusion coefficients. To be able to calculate the relative abundance of the isotopes ^{6}Li and ^{7}Li it has been considered that ^{6}Li diffuses faster than ^{7}Li (e.g. Richter et al., 1999; Richter et al., 2003). In the paragraph above Γ_{Li} (for the slower but more abundant ^{7}Li) was calculated on the base of Γ_{Mg-Fe}. With the relation of the dependence of the diffusivities

Chapter 3: Indications of the eruptive history of volcanoes in zoned olivine crystals with respect to Fe-Mg, Li and other trace element concentrations and Li isotopes

on the masses of isotopes Γ_{Li} can be adjusted for the faster isotope ^6Li. For this purpose a β-value in Eq. (3.5) indicates the relation of the relative diffusivities of the isotopes (Richter et al., 1999):

$$\frac{\Gamma_{7_{Li}}}{\Gamma_{6_{Li}}} \cong \frac{D_{7_{Li}}}{D_{6_{Li}}} = \left(\frac{m_{7_{Li}}}{m_{6_{Li}}}\right)^{\beta} \qquad\qquad \text{Eq. (3.5)}$$

The modeled Li concentrations calculated with Γ for ^6Li and ^7Li can be inserted into the δ-notation for Li given in Eq. (3.1). The modeled δ^7Li-values fit the measured δ^7Li-values for olivines from Klyuchevskoy F-cone and Bilyukai (Figure 3.11) and SFA Arafo (Figure 3.12). With the empirical expression from Eq. (3.5) β-values used for modeling were adjusted to increase or decrease the amplitude of the Li isotope profile. For Li in olivine a β-factor of 0.4±0.1 has been experimentally determined (Richter et al., 2017) indicating the diffusivity of ^6Li to be faster than that of ^7Li by 4.7 % to 8.0 %, whereas a β-factor of 0.5 describes diffusion in monoatomic gases (Chapman and Cowling, 1953). (Richter et al., 2017) applied β-factors of 0.3 -0.36 to model natural olivines, in an older study they determined β-factors in pyroxene with β = 0.27 and modeled natural pyroxenes with β = 0.25-0.3 (Richter et al., 2014). The β-factors applied for modeling the Klyuchevskoy and SFA olivines are β=0.25 for K2 and β=0.3 for K5 (Figure 3.11) and β=0.35 for Arafo (Figure 3.12). The β-factors for K5 and Arafo fall well into the range determined by (Richter et al., 2017). The β-factors for K2 are slightly lower, but still close to the values from (Richter et al., 2017).

From the profiles modeled in Figure 3.11 it is evident, that especially in the cases where the profiles have been modeled with the infinite approach the rim δ^7Li-values cannot be matched. The process modeled by the infinite approach is not the last one in the time series of events and there has to be a subsequent process which is displayed by a semi-infinite model. The infinite approach is used mostly for olivines with a complex zoning type and a visible other process straight at the rim. This process was not modeled because the concentration differences between the equilibrating crystal zones are too low or the plateau areas are too small to achieve reasonable values for the model. Nevertheless, this should be kept in mind when considering the fit of the model and the measured values explaining the misfit.

Chapter 3: Indications of the eruptive history of volcanoes in zoned olivine crystals with respect to Fe-Mg, Li and other trace element concentrations and Li isotopes
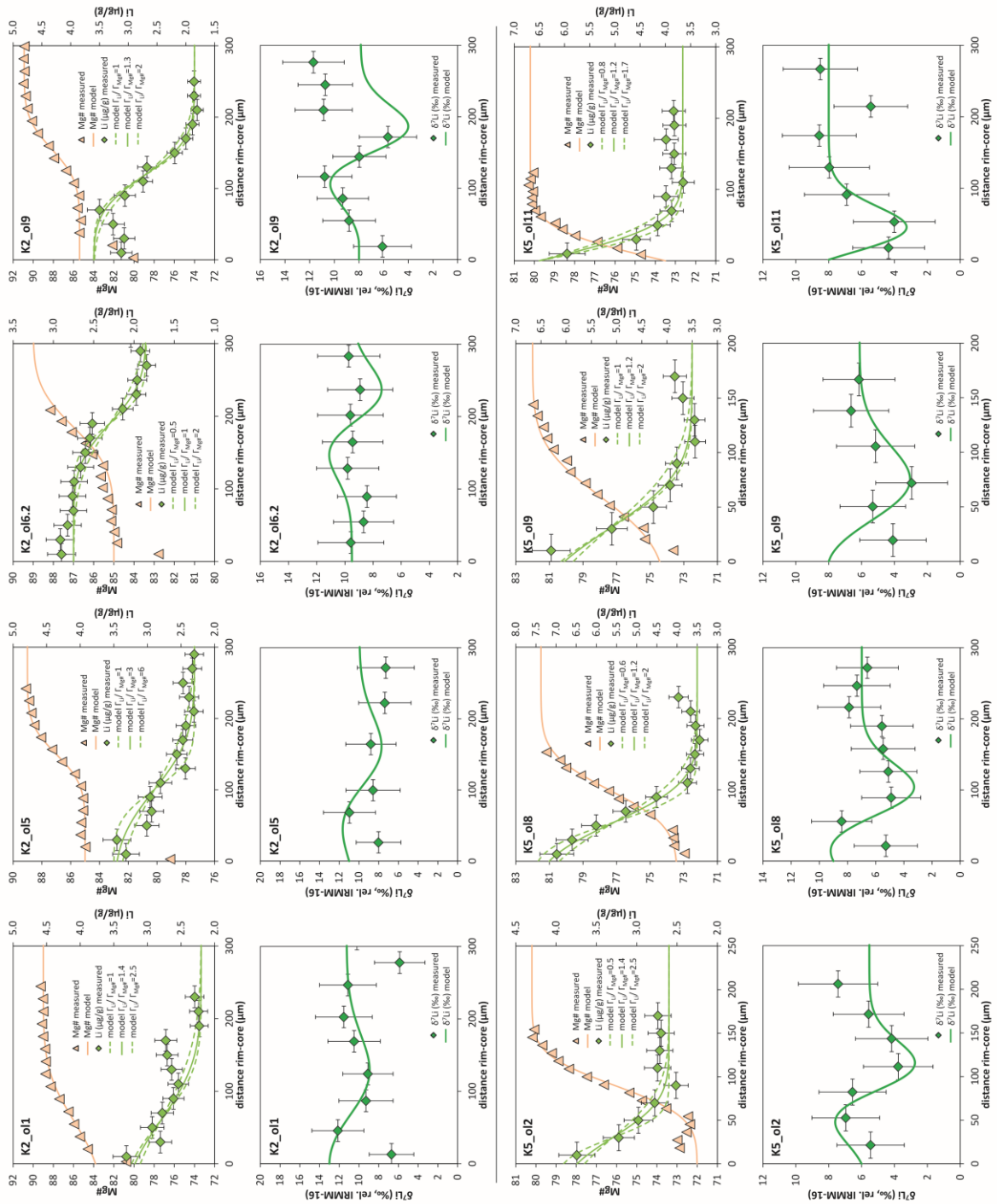
Figure 3.11: Modeling of relative diffusion coefficients and Li isotope modeling for Klyuchevskoy F-cone (K2) olivine 1, 5, 6.2 and 9 and Bilyukai (K5) olivine 2, 8, 9 and 11. Mg# = Mg/(Mg+Fe), measured with EMPA, Li concentrations were measured with fs-LA-SF-ICP-MS, vertical error bars display the relative standard deviation of 6 %, Li isotopes were measured with fs-LA-MC-ICP-MS vertical error bars display 2 σ of the standard-bracketing, horizontal error bars for Li concentrations and Li isotopes display the spatial resolution of 30 µm. β-factor applied for modeling were β=0.25 for K2 and β=0.3 for K5.

Chapter 3: Indications of the eruptive history of volcanoes in zoned olivine crystals with respect to Fe-Mg, Li and other trace element concentrations and Li isotopes
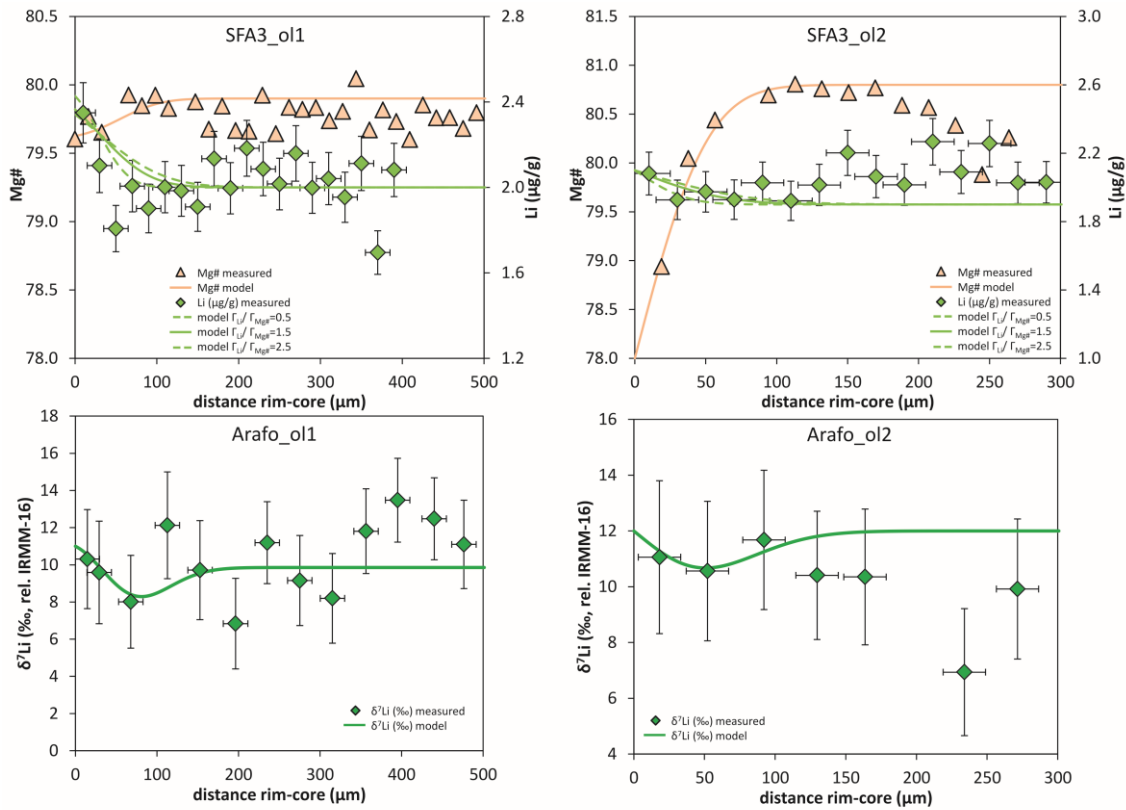
Figure 3.12: Modeling of relative diffusion coefficients and Li isotope diffusion profiles for SFA Arafo (SFA3) olivine 1 and 2. Mg# = Mg/(Mg+Fe), measured with EMPA, Li concentrations were measured with fs-LA-SF-ICP-MS, vertical error bars display the relative standard deviation of 6 %, Li isotopes were measured with fs-LA-MC-ICP-MS vertical error bars display 2 σ of the standard-bracketing, horizontal error bars for Li concentrations and Li isotopes display the spatial resolution of 30 μm. The β-factor applied for modeling was β=0.35.

3.7 Comparison of olivines from different geotectonic settings

Comparing the two settings of Klyuchevskoy (island arc) and SFA (ocean island) it is evident, that the absolute number of Fo-reservoirs, as well as Li-reservoirs, is more limited in SFA and the Li concentrations in SFA are in general lower than in Kluchevskoy sample suite. The most primitive Fo-reservoir in Klyuchevskoy (Fo_{90-91}) is accompanied by Li = 1.8-2.1 µg/g whereas the same Li concentration occurs at a less primitive reservoir in SFA (Fo_{85-86}, Li 1.8-2.1 µg/g). The spread in Li rim concentration is larger in Klyuchevskoy (2.6 to 7.0 µg/g) than in SFA (1.9 to 2.8 µg/g). This might be a combined consequence of the Li concentration in the source material and hence lower chemical gradient between olivine and melt in SFA compared to Klyuchevskoy and the duration of the differentiation process before eruption. Furthermore, wall rock

Chapter 3: Indications of the eruptive history of volcanoes in zoned olivine crystals with respect to Fe-Mg, Li and other trace element concentrations and Li isotopes

assimilation of e.g. sedimentary material getting in contact with the magma chamber can influence the Li abundance in the melt (DePaolo, 1981). For the SFA ocean island setting there is oceanic crust overlying and surrounding the magma chamber, which is (except from hydrothermally affected areas) not very much influencing the Li content in the magma chamber. For the Klyuchevskoy arc setting subduction derived fluids could be incorporated in the melt reservoirs at a higher crustal level causing elevated Li concentrations.

3.8 Conclusion

Several olivines of the investigated localities have experienced a multi stage growth and transport between different magma chambers where several reservoirs have been determined according to major element composition (Mg#). This relationship has also been found in some minor and trace elements, especially Li has been considered here. Diffusion coefficients of Li relative to Mg-Fe exchange diffusion have been determined and show that Li in natural olivines diffuses ~1.2-4.0 times faster than Mg-Fe yielding similar rates as previously observed by (Qian et al., 2010; Oeser-Rabe, 2015). These rates of Li diffusivities are lower than those that have been determined in experimental studies (Dohmen et al., 2010), which may be related to the concentration differences between natural olivines and those used for the experiments. It is evident that results between natural and experimental studies of Li diffusion coefficients are varying and further thorough studies have to be conducted to constrain the parameters which influence Li diffusion. For this purpose experimental studies at low concentrations and closer to natural conditions could be performed. Lithium isotope profiles and modeling of these show, that with the calculated relative diffusivities Li chemical and isotope profiles can be matched and the measured profiles of Mg-Fe and Li might display the same magmatic process. Furthermore, the history of crystals which have experienced several stages of crystal growth and diffusive re-equilibration can be resolved.

Dissertation of Lena Steinmann

Chapter 4: Multi-stage magma evolution in intra-plate volcanoes: Insights from combined *in situ* Li and Mg-Fe chemical and isotopic diffusion profiles in olivine

Chapter 4: Multi-stage magma evolution in intra-plate volcanoes: Insights from combined *in situ* Li and Mg-Fe chemical and isotopic diffusion profiles in olivine

4.1 Abstract

Olivine pheno- and xenocrysts from two locations in the Massif Central volcanic region (France) have been investigated and lithium chemical and isotopic profiles have been determined. The shape and orientation of both the chemical and isotopic profiles indicate that they were dominantly generated by Li diffusion into and within the olivine grains during magmatic evolution and could be modeled in combination with existing Mg and Fe isotope inter-diffusion profiles. Extremely low δ^7Li-values down to -30.7 ‰ (relative to IRMM-16) in the crystal core region and elevated values at the crystal rims (δ^7Li ~8 to 10 ‰), along with increasing concentrations from cores (~3 to 1 µg/g) towards the rim (12 to 6 µg/g) have been found. While Mg-Fe isotope and chemical profiles have been modeled by a single diffusive event (Oeser M., Dohmen, R., Horn, I., Schuth, S., Weyer, S. (2015) GCA **154,** 130-150), concentration and isotope profiles of the fast-diffusing Li indicate a second diffusive event, which is not detectable by the slower Mg-Fe exchange diffusion couple. Accordingly, Li profiles record diffusion events that are invisible by Fe-Mg diffusion profiles alone. The Li concentration and isotope profiles can be modeled in a two-step diffusion model. Time scales of the first diffusion event were taken from Oeser et al. (2015) based on Mg-Fe isotopic exchange diffusion modeling with well-determined diffusion coefficients. Such modeling provided time scales of ~250 days (Banne D'Ordanche) and ~3.3 years (Roche Sauterre) which have been interpreted as the residence time of the olivine crystals in a magma chamber. This first event also generated the low δ^7Li observed in olivine cores. Comparison of the length of the Fe-Mg and Li profiles could thus be used to determine the less well known diffusion coefficients of Li in the studied olivine crystals. Applying these Li diffusion coefficients in a Li diffusion model, the second diffusion step yields shorter diffusion times (20 days to 200 days). This latter event might represent a degassing process, related to the ascent of the magma prior to eruption. Such a process would only affect Li, which behaves volatilely during degassing, but not the refractory elements Fe and Mg. The findings of this study show that the combined use of isotopic diffusion systems with different diffusion rates, i.e. of spatially resolved δ^7Li and Mg-Fe isotope diffusion

Chapter 4: Multi-stage magma evolution in intra-plate volcanoes: Insights from combined *in situ* Li and Mg-Fe chemical and isotopic diffusion profiles in olivine

profiles, is a powerful tool to model even multi-stage evolution processes in a magmatic system. Furthermore, they show that experimentally determined diffusion rates for Li (concentrations and isotopes) are frequently overestimated, as compared to the observed Li diffusivities determined relative to the well-known diffusion rates of the Mg-Fe diffusion couple. Potentially, Li diffusion, at typically low Li concentration levels in natural olivine, is coupled to that of other slower-diffusing elements, which is not the case at higher concentration levels in laboratory experiments.

4.2 Introduction

In principle, chemically zoned crystals can be the result of crystal growth in an evolving melt (growth zoning) or of chemical diffusion due to compositional contrasts between minerals and the surrounding melt (diffusion zoning) (Costa et al., 2008). Chemical diffusion of Li is caused by a chemical disequilibrium which develops due to compositional contrasts in the melt. This can be caused either by an increase in Li concentration in the magma, typically either due to magma mixing or crystal fractionation, or, due to a decrease in Li concentration in the melt, e.g. during a degassing process (Vlastélic et al., 2011; Lynn et al., 2018). The so developed zoning can unravel the migration of crystals through a dynamic plumbing systems with several reservoirs of differently composed melts (Kahl et al., 2013; Kahl et al., 2015). Olivine and clinopyroxene as early forming crystals are the most likely minerals to accept Li in their structure due to similar ionic radii of Mg and Fe in the octahedrally coordinated sites (Shannon, 1976). Though, during magma differentiation, Li behaves as incompatible with typical concentrations of 3 to 8 µg/g in basalts and of ~20 µg/g in rhyolites (Ryan and Langmuir, 1987; Ryan and Kyle, 2004) with olivine/melt distribution coefficients of 0.2-0.35 (Ryan and Langmuir, 1987; Brenan et al., 1998). As olivine is a very abundant mineral in primitive basalts and chemical diffusion in olivine is well characterized (e.g. for Fe-Mg exchange or for Li (Dohmen et al., 2007; Dohmen and Chakraborty, 2007; Dohmen et al., 2010; Richter et al., 2017)), it frequently serves for diffusions studies (e.g. Lynn et al., 2018; Oeser et al., 2018). However, growth and diffusive origin of zoning cannot easily be distinguished by the investigation of the chemical zoning alone and, notably, only the latter bears information on time.

Chapter 4: Multi-stage magma evolution in intra-plate volcanoes: Insights from combined *in situ* Li and Mg-Fe chemical and isotopic diffusion profiles in olivine

At magmatic temperatures, diffusion results in large isotope fractionation, e.g. of Li, Fe and Mg, which may be recorded as isotopic zoning (e.g. Richter et al., 2003). Isotopic zoning coupled with chemical zoning is a strong indicator for a diffusive origin of the zoning because high-temperature equilibrium isotope fractionation is very limited, e.g. for Li (Tomascak et al., 1999a; Jeffcoate et al., 2007; Parkinson et al., 2007), Fe (Weyer and Ionov, 2007) and Mg (Teng et al., 2007b; Liu et al., 2011). The combined information of chemical and isotopic zoning of Fe and Mg have been successfully used in a number of recent studies in order to investigate the complex magmatic evolution of a variety of different settings and to evaluate the effect of the end member processes of crystal growth and pure diffusion-driven zoning (Teng et al., 2011; Sio et al., 2013; Oeser et al., 2015 and 2018; Collinet et al., 2017). Lithium is the lightest alkali metal and has two stable isotopes with a relative mass difference of ~17%. Accordingly, large isotopic variations have been observed between geochemical reservoirs (see compilation in Penniston-Dorland et al. (2017) and references therein). Large Li isotope fractionation has also been observed on the mineral scale, up to 29 ‰ in a clinopyroxene from the Solomon Islands volcanic rocks (Parkinson et al., 2007), also 29 ‰ in San Carlos olivine and 38 ‰ for an orthopyroxene crystal (Jeffcoate et al., 2007), which is thought to be mainly caused by chemical diffusion. It is highly debated whether low δ^7Li-values in olivines can be either caused by subduction-derived metasomatized material (Hamelin et al., 2009; Gu et al., 2016) or if the enrichment of light isotopic material is caused by diffusion in the mantle or during magmatic processes (Marschall et al., 2007a; Marschall et al., 2007b; Magna et al., 2008).

Lithium isotope profiles for chemically zoned magmatic olivines from the Massif Central continental intra-plate volcanic system shall be analyzed by a newly developed matrix independent measurement method by femtosecond-laser ablation-MC-ICP-MS (Steinmann et al., 2019). This sample suite has already been investigated in a previous study, regarding Fe-Mg inter-diffusion processes and diffusion-driven Fe-Mg isotopic zoning of olivine (Oeser et al., 2015) which provides a framework for the *in situ* investigation of Li concentrations and isotope ratios of olivine on the same samples. The aim of this study is to investigate if isotope fractionation of the fast-diffusing Li isotope system is coupled to the more established Mg-Fe exchange diffusion couple as previously observed by Weyer and Seitz (2012) based on the investigation of bulk olivine. Potential decoupling of Fe-Mg and Li isotope systematics may unravel

Chapter 4: Multi-stage magma evolution in intra-plate volcanoes: Insights from combined *in situ* Li and Mg-Fe chemical and isotopic diffusion profiles in olivine

processes which remain hidden when looking at only one of the isotope systems, and thus may help to reveal more complex scenarios of magmatic evolution, including e.g. cooling, magma mixing and degassing.

4.3   Samples and geological setting

In this study samples from two locations (Roche Sauterre (N45°54.858', E02°55.674') and Banne D'Ordanche (N45°36.671', E02°46.355')) in the continental intra-plate volcanic setting Massif Central (France) have been investigated. Olivine-phyric basanites from Roche Sauterre may originate from a large lava flow that merged into a small lava lake in a paleo-topographic low during the late Miocene to early Pliocene (Nehlig et al., 2001; Lorand et al., 2003; Richet, 2003). At the summit of the Banne D'Ordanche, an olivine- and clinopyroxene-bearing ~710,000 year old basanite from the north-west slope of a former strato-volcano was sampled (Richet, 2003). The samples have been characterized regarding their major and trace element composition by (Oeser et al., 2015). All investigated olivines are normally zoned regarding Mg# (Mg#=[Mg]/([Mg]+[Fe])) and display values from 0.76 to 0.8 in the rim and 0.86 to 0.88 in the core. Nickel concentrations follow this trend. The width of Mg# zoning reaches up to 400 µm into the up to 2 mm big olivine crystals. The Mg# in the rims varies from ~0.74 for the Roche Sauterre samples to 0.8 for Banne D'Ordanche. The cores of the Banne D'Ordanche olivines have Mg# around 89-90 and the olivines from Roche Sauterre dominantly have Mg# around 86-87. The Mg# zoning is accompanied by inversely correlated Mg and Fe isotopic signatures underlining a diffusive origin of the zoning. The inter-correlation indicates an inter-diffusive process with Mg diffusing out of the olivine and Fe diffusing into the olivine (Oeser et al., 2015). Lithium concentrations and Mg# are summarized in Table A.4.2 in the appendix.

4.4   Methods

4.4.1   Lithium isotopes with fs-LA-MC-ICP-MS

A femtosecond laser based ablation system (Spectra-Physics Solstice) was coupled to a multi collector inductively coupled plasma mass spectrometer (MC-ICP-MS, Thermo-

Chapter 4: Multi-stage magma evolution in intra-plate volcanoes: Insights from combined *in situ* Li and Mg-Fe chemical and isotopic diffusion profiles in olivine

Finnigan Neptune Plus). The ablation beam has a pulse duration of ~100 fs and wavelength of 194 nm which is generated via frequency conversion from an infrared beam with 775 nm wavelength in a mirror and lens system and focused on the sample surface via a modified in-house built New Wave (ESI) stage combined with an optical microscope (Horn et al., 2006; Horn and von Blanckenburg, 2007). The laser spot size of ~26 µm on the bracketing standard GOR132-G (Gorgona Island komatiite) allows for sufficient spatial resolution. The protocol for Li isotope measurement was applied as described in detail in (Steinmann et al., 2019). In brief, measurements were performed at relatively cool plasma conditions (900 W) in order to avoid matrix ionization in the plasma. *In situ* Li isotope ratio measurements were performed in static mode at low mass resolution which is sufficient to resolve atomic interferences. In order to keep background Li signals low the measurements were performed under dry plasma conditions. The sample was mixed in a homogenization device to increase signal stability (Chapter 1 of this dissertation, Steinmann et al., 2019). For the detection of ^{7}Li a $10^{13}\,\Omega$ amplifiers coupled to a faraday cup was deployed, while a secondary ion multiplier was used for the detection of the less abundant ^{6}Li. Due to the slower signal response of the $10^{13}\,\Omega$ amplifiers (as compared to $10^{11}\,\Omega$ amplifiers) a tau correction (Kimura et al., 2016) is applied in data evaluation. All measurements were performed using standard-sample-bracketing with the komatiitic MPI DING reference glass GOR132-G as bracketing standard according to Eq. (4.1) and recalculated to IRMM-16 (Steinmann et al., 2019).

$$\delta\ ^7Li = \left[\frac{\left(\frac{^7Li}{^6Li}\right)_{sample}}{\left(\frac{^7Li}{^6Li}\right)_{GOR132-G}} - 1 \right] \times 1000 \qquad \text{Eq. (4.1)}$$

Measurements of the bracketing standard GOR132-G were performed in raster ablation mode with a scan speed of 20 µm/s, the olivine profiles were measured in line ablation mode with lines arranged parallel to the crystal rim so that each line accounts for one measured δ^7Li-value. Individual measurements consist of 180 cycles, each with an integration time of 1.049 s. The first ~35 cycles were used for background correction,

Chapter 4: Multi-stage magma evolution in intra-plate volcanoes: Insights from combined *in situ* Li and Mg-Fe chemical and isotopic diffusion profiles in olivine

measuring only the gas blank without a laser ablation signal. This was followed by ~130 cycles of sample ablation. As internal control for the accuracy of the method, the MPI DING reference glass T1-G (δ^7Li = 1.6-2.4 ‰, (Jochum et al., 2006; Le Roux, 2010; Xu et al., 2013)) has been measured yielding a long term reproducibility of 2.1 ‰ (δ^7Li = 0.4 ‰, 2 SD for n=64 in 16 sessions throughout 22 months) in agreement with Steinmann et al. (2019). The measurement profiles have been placed as ~100 µm long lines parallel to the crystal rim like the electron microprobe and trace element analyses but in order to detect a sufficient number of Li ions to satisfy counting statistics, it is necessary to measure several lines stacked parallelly to the crystal rim (Figure 4.1). This is necessary due to the low concentration of Li in the samples in order to achieve a stable signal over the duration of the measurement.
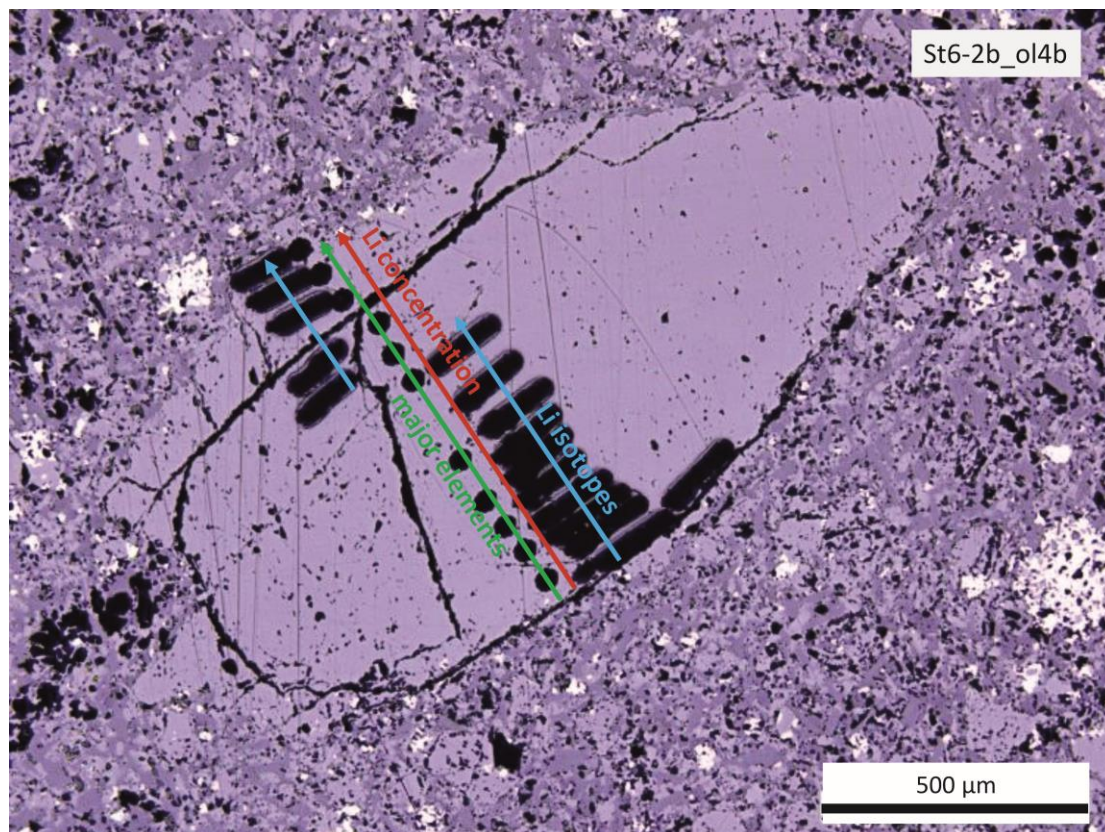
Figure 4.1: Measurement lines on BdOr1-ol2, Li concentration and Li isotope profiles measured by laser ablation with visible consumption of the sample, major elements measured with EMPA and no visible consumption of the sample.

Chapter 4: Multi-stage magma evolution in intra-plate volcanoes: Insights from combined *in situ* Li and Mg-Fe chemical and isotopic diffusion profiles in olivine

4.4.2   Diffusion models

Diffusive processes have been modeled in several studies by applying an analytical or numerical approach to resolve Fick's second law of diffusion with the aim of equilibrating an initially homogeneous olivine with new boundary conditions e.g. by changing the environment conditions and concentration in the surrounding melt (Costa et al., 2008). For this purpose the one-dimensional expression for the diffusion equation in a plane sheet geometry in Eq. (4.2) has been solved for diffusion modeling with an analytical and a numerical calculation, the formulas are listed in Figure A.4.1 in the appendix.

$$\frac{\partial C_i(x,t)}{\partial t} = \frac{\partial}{\partial x}\left[D_i\,\frac{\partial C_i(x,t)}{\partial x}\right] \qquad\qquad \text{Eq. (4.2)}$$

The determination of the diffusion coefficient of Li has been approached either by analyzing natural samples or by performing experiments at defined conditions in the literature. Three approaches regarding the diffusivity of Li are compared in this study.

(1) Several studies have observed an interdependence of the diffusivities of e.g. Fe, Mg, Ni, Mn, Li and other trace elements (Qian et al., 2010; Spandler and O'Neill, 2010; Oeser-Rabe, 2015, Chapter 3 of this dissertation) and determined diffusivities of Li relative to Mg-Fe with the relation in Eq. (4.3). The factor Γ is denoted the product of diffusion coefficient and duration of the diffusive flux ($\Gamma = D \cdot t$; e.g. Ganguly, (2002)). Eq. (4.3) is valid under the assumption that the diffusion time t is the same or very similar for all elements.

$$\frac{\Gamma_{Li}}{\Gamma_{Mg-Fe}} \cong \frac{D_{Li}}{D_{Mg-Fe}} \qquad\qquad \text{Eq. (4.3)}$$

(2) In the study of (Oeser et al., 2015) Mg and Fe inter-diffusion have been modeled, in order to acquire time scales for diffusion-driven Fe-Mg exchange and to infer the residence of the olivine crystals in a magma. In approach (2) based on these time scales

Chapter 4: Multi-stage magma evolution in intra-plate volcanoes: Insights from combined *in situ* Li and Mg-Fe chemical and isotopic diffusion profiles in olivine

(fixed parameter of t) the profile is fitted by adjusting D_{Li} in order to determine the matching Li diffusivity.

(3) An experimental study performed by Dohmen et al. (2010) found the existence of two diffusion mechanisms in olivine. One "fast" diffusion mechanism, which is occurring on the interstitial sites in the olivine structure and one "slow", metal vacancy-controlled diffusion mechanism, which is occurring on the octahedral sites. Presumably, in natural systems interstitial diffusion is not activated and Li diffuses via the octahedral sites (Dohmen et al., 2010). From experimental studies at 800 to 1200 °C at a pressure of 100 kPa and at fO$_2$ ≈ WM buffer Dohmen et al. (2010) have developed an equation from an approximated Arrhenius relation to determine the diffusivity of the "slow" diffusion mechanism in dependence of temperature in olivine:

$$\log(D_{Li}) = -5.92(\pm 1.0) - 1.2847 \times 10^4 / T(K) \qquad \text{Eq. (4.4)}$$

Finally, the results of the three approaches are compared in order to understand which one is most fitting to determine diffusivities in natural systems, more precisely for the investigated olivines. From the samples described above, olivine crystals with high Li concentrations and with the largest variations in Li concentrations from rim to core have been selected for Li isotope analysis and modeling of profiles. For approach (1) an analytical solution (Eq. (A.4.1) and Eq. (A.4.2) in Table A.4.1) of Eq. (4.2) is applied and for approach (2) a numerical solution by the method of finite differences of the diffusion equation in Eq. (4.2) (Eq. (A.4.3) in Table A.4.1) is applied. For approach (3) the diffusivity is calculated according to Eq. (4.4), the diffusivity depends on the temperature T.

The relation between the diffusion coefficients of the two isotopes of Li can be described by the empirical formula of (Richter et al., 1999):

$$\frac{D_{^6Li}}{D_{^7Li}} = \left(\frac{m_{^7Li}}{m_{^6Li}}\right)^{\beta} \qquad \text{Eq. (4.5)}$$

Chapter 4: Multi-stage magma evolution in intra-plate volcanoes: Insights from combined *in situ* Li and Mg-Fe chemical and isotopic diffusion profiles in olivine

Where D is the diffusion coefficient of ^{6}Li and ^{7}Li, *m* are the atomic masses of ^{6}Li and ^{7}Li in Dalton and the β-value which describes the diffusion-driven isotope fractionation. β is an empirical constant which depends on the diffusion medium and is smaller than 0.5 (Richter et al., 1999). A β-value of 0.5 is actually the factor for a non-uniform gas (Chapman and Cowling, 1953) and maximum value achievable. The β-value has been determined experimentally and can be fitted by values of β = 0.4±0.1 for the crystallographic a- and c-axis whereas the fractionation along the b-axis appears to be slightly lower (Richter et al., 2017). Recalculating the percental difference in the diffusivities of the two Li isotopes determined by (Dohmen et al., 2010) a β-value of 0.19 (^{6}Li is 3 % faster than ^{7}Li) may be assumed for the slow diffusion mechanism and of 0.32 (^{6}Li is 5 % faster than ^{7}Li) for the fast diffusion mechanism. Compared to Richter et al. (2017) these values are slightly lower but comparable to Li diffusivity in molten oxides (Richter et al., 2003).

4.5 Results

Four olivines from Banne D'Ordanche (BdOr-1_ol1, BdOr-1_ol2, BdOr-1_olxen1 and BdOr-1_olxen2) have been analyzed regarding their isotopic composition. Concentration data has been acquired by Oeser-Rabe (2015), the olivines display Li concentrations varying from ~8-9 µg/g in the rim to 1-2 µg/g in the core with the lowest Li concentration in the core for all samples. The lava lake of Roche Sauterre has been sampled at two positions, two olivines of one sample (St6-2b_ol4b and St6-2b_ol5) display concentrations varying from 7 µg/g at the rim to 3 µg/g in the core, two olivines of the other sample (St3-3a_ol1 and St3_3a_ol2) have somewhat lower Li concentrations from 4 µg/g at the rim to 1 µg/g in the core. The Li concentration profiles show different shapes with some of them showing a slight increase starting from the rim before concentration decreases towards the core, (Figure 4.2 (a)-(c)). Lithium concentrations and isotope compositions for all investigated samples are compiled Table 4.1.

Chapter 4: Multi-stage magma evolution in intra-plate volcanoes: Insights from combined *in situ* Li and Mg-Fe chemical and isotopic diffusion profiles in olivine

Table 4.1: Lithium rim and core compositions of investigated olivines

	Li_{rim} ($\mu g/g$)*	Li_{core} ($\mu g/g$)*	$Li_{bulk\ rock}$ ($\mu g/g$)*	$\Delta^7Li^{max-min}$ (‰)	δ^7Li_{max} (‰)	δ^7Li_{min} (‰)	δ^7Li_{bulk} (‰)[#]
BdOr-1_ol1	8.5	1.7	6.14	13.5	2.3	-11.3	-
BdOr-1_ol2	6.3	1.2	6.14	38.0	7.4	-30.7	-
BdOr-1_olxen1	12.5	8.7	6.14	18.2	5.1	-13.1	-
BdOr-1_olxen2	8.1	2.0	6.14	17.1	7.5	-9.6	-
St3-3a_ol1	3.9	1.8	5.70	21.5	7.0	-14.5	2.3±2.0
St3-3a_ol2	2.3	1.1	5.70	23.1	9.0	-14.1	2.3±2.0
St6-2b_ol4b	5.5	3.9	5.78	22.2	11.4	-10.7	3.3±1.2
St6-2b_ol5	5.9	3.1	5.78	22.9	13.2	-14.2	3.3±1.2

* published in Oeser et al. (2015) and Oeser-Rabe (2015)

[#] from Chapter 2 of this dissertation

Lithium isotope profiles of all measured olivines display elevated δ^7Li-values at the crystal rims and decreasing values towards the cores (Figure 4.2) with a $\Delta^7Li^{rim\text{-}core}$ = 21.5 ‰ to 27.3 ‰ for Roche Sauterre and $\Delta^7Li^{rim\text{-}core}$ = 13.5 ‰ to 18.2 ‰ and one crystal with $\Delta^7Li^{rim\text{-}core}$ = 38 ‰ for Banne D'Ordanche. In most cases $\Delta^7Li^{rim\text{-}core}$ is equal to $\Delta^7Li^{min\text{-}max}$ which indicates that the cores are influenced by a diffusive process and have not preserved their original Li isotopic composition. The δ^7Li-values in the cores (-9.6 to -14.5 ‰, one crystal with -30.7 ‰) are clearly lower than δ^7Li-values of ~4 ‰ of volcanic bulk rock (Seitz et al., 2004; Magna et al., 2006; Jeffcoate et al., 2007) but such low δ^7Li-values in Li isotope profiles in natural olivines have been observed for Massif Central olivines (Gu et al., 2016) and in San Carlos xenolith olivine (Jeffcoate et al., 2007). Lithium concentration and isotope profiles are correlated, with high Li concentration and high δ^7Li-values at the rim and decreasing Li concentrations and lower δ^7Li-values towards the core (Figure 4.2). The shape of the Li isotope profiles is consistent with the shape which would be expected from diffusion-driven isotope fractionation (Parkinson et al., 2007). Iron and magnesium isotope profiles which have been acquired by Oeser et al. (2015) are plotted for comparison in Figure 4.2 (d)-(f). The width of Li isotopic zoning is either similar or exceeds that of Fe and Mg isotopic zoning. All measured Li concentration and isotope ratios (this study) are listed in the appendix (Table A.4.3 and Table A.4.4) together with the Mg and Fe isotope compositions determined by Oeser et al. (2015).

Chapter 4: Multi-stage magma evolution in intra-plate volcanoes: Insights from combined *in situ* Li and Mg-Fe chemical and isotopic diffusion profiles in olivine
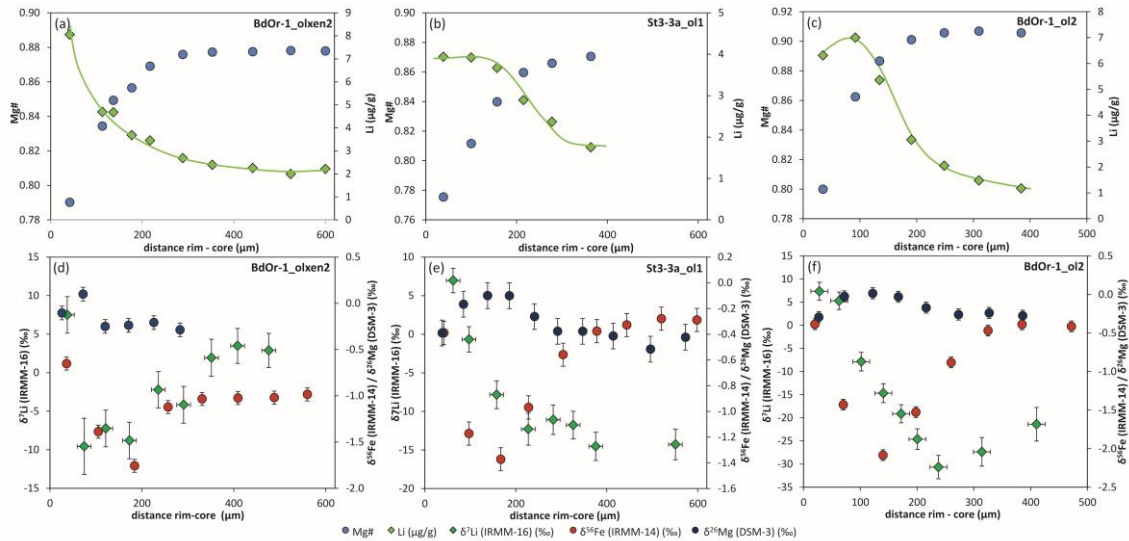
Figure 4.2: Mg-Fe and Li concentration zoning for (a) BdOr1_olxen2, (b) St3-3a_ol1 and (c) BdOr-1_ol2. Li concentration zoning with redrawn shape of the concentration profile (green lines) and Mg# are reversely correlated. Mg, Fe and Li isotope profiles from for (d) BdOr1_olxen2, (e) St3-3a_ol1 and (f) BdOr-1_ol2. The isotope profiles are indicating a coupling between Li and Mg-Fe diffusion. Horizontal error bars display the spot size for laser ablation (~30 µm) and vertical error bars represent the analytical uncertainty (2σ) during one sample-standard-bracketing for Li and 2SD during one analytical session for Mg and Fe (values for Mg and Fe isotopes from Oeser et al. (2015)).

4.6 Discussion

4.6.1 Initial conditions of the system

Coupled Li concentration and isotope profiles from the rim of the crystal towards the core, and the extremely light isotopic composition of the olivine cores (δ^7Li_{min}-values down to -30.7 ‰, Table 4.1) strongly indicate a diffusive origin of the zoning caused by faster diffusion of ^6Li into the crystal as compared to ^7Li. A diffusive origin is also indicated by the crudely correlated Li and Fe-Mg concentration and isotope diffusion profiles (Figure 4.2). The chemical profile shapes observed for olivine from the Massif Central can be distinguished into three types (green lines in Figure 4.2 (a)-(c)), with always higher Li concentrations in the rims and lower concentrations in the cores. Type I (Figure 4.2 (a)) shows decreasing Li concentrations towards the core which is a typical profile for diffusion into the crystal. Type II (Figure 4.2 (b)) consists of two compositional plateaus with constant Li concentrations and a gradually decreasing Li concentration in the transition zone. Type III (Figure 4.2 (c)) exhibits maximum Li

Chapter 4: Multi-stage magma evolution in intra-plate volcanoes: Insights from combined *in situ* Li and Mg-Fe chemical and isotopic diffusion profiles in olivine

concentration at some distance from the rim (~100 µm) and then a decrease of Li concentration towards the core, these profiles might contain information on a first event of Li diffusion into the crystals and a second event causing Li diffusion out of the crystals. Nevertheless, the differences which are abundant in the concentration profiles cannot be clearly distinguished in the isotope profiles.

Before diffusion models can be established the initial and boundary conditions constraining the system have to be evaluated. The initial condition is described as the starting point of the model, which is the Li concentration (profile) before diffusion started (Costa et al., 2008) and here also the initial isotope composition (or isotope profile). Here we assume that the crystals were initially homogeneously growing in equilibrium with the melt. Assuming that the melt had initially a similar Li concentration as that analysed for whole rock samples (BdOr1 = 6.14 µg/g, St3-3a =5.7 µg/g and St6-2b = 5.78 µg/g (Oeser et al., 2015)) and applying the Li olivine/melt partition coefficient determined by Brenen et al. (1998) for olivine with high Mg# (of ~ 0.2), this results in equilibrium concentrations between 1.16 and 1.47 µg/g. Further information on the calculation can be found in the appendix (Figure A.4.1). Lithium concentrations in the olivine cores range from 1 to 2 µg/g for the two olivine crystals from sample St3a from Roche Sauterre, as well as for three out of four Banne D'Ordanche olivines. The other two Roche Sauterre crystals (from St6) exhibit higher Li concentrations of 3.1 µg/g and 3.9 µg/g (Table 4.1). Only one crystal from Banne D'Ordanche displays a Li_{core} concentration of 8.7 µg/g, likely indicating significant Li diffusion into the core. Two of the crystals have been found in a glomerocryst and hence are described as xenocrysts by (Oeser et al., 2015). The initial concentration of such crystals is difficult to constrain. Notably, the rim Li concentration of most olivine grains is on the order of 4 to 8 µg/g and difficult to explain with olivine/melt partition coefficient on the order of 0.2 (Brenan et al., 1998), as this would indicate extremely high Li concentrations (on the order of 20 to 40 µg/g) in the basalts at the time when diffusion ceased, i.e. at the end of fractional crystallization. Such high Li concentrations have not been observed for any of the investigated basalts (Oeser et al., 2015). However, although Brenan et al. (1998) suggested low olivine/melt partition coefficient on the order of ~0.2, those have essentially been determined for extremely forsterite-rich olivine, while a higher olivine/melt partition coefficient (of ~0.35) was observed for an olivine with a slightly lower Mg# (of 92). Other authors have observed higher

Chapter 4: Multi-stage magma evolution in intra-plate volcanoes: Insights from combined *in situ* Li and Mg-Fe chemical and isotopic diffusion profiles in olivine

partitioning coefficients, between 0.21 and 0.56 (Taura et al., 1998; McDade et al., 2003; Ottolini et al., 2009), which are always in combination with lower Mg# than the forsterite-rich olivines form Brenan et al. (1998). Ottolini et al. (2009) have interpreted, that there might be an influence of the rock composition on the partitioning coefficient; Taura et al. (1998) concluded a pressure dependence. Potentially, Li partitioning into olivine further increase with decreasing Mg#. If so, the high Li contents, observed in the olivine rims, may primarily be driven by increasing Li partitioning into olivine with decreasing Mg# during fractional crystallization, rather than by increasing Li contents in the melt, though Li concentrations in the melt at the end of fractional crystallization may have been slightly higher than those observed in the sampled basalts.

Similar to the Li concentrations, the measured δ^7Li_{bulk} of the basalts may be assumed as the initial Li isotope composition of the olivine crystals before diffusion started. The isotopic composition of fresh basalts varies from +2 ‰ to +5 ‰ and seems not to change significantly during fractional crystallization (Chan et al., 1992; Elliott et al., 2006; Tomascak et al., 2008). For Roche Sauterre St6 a δ^7Li_{bulk} of 3.3 ± 1.3 ‰ and for St3 2.3 ± 2.0 ‰ have been determined (Chapter 2 of this dissertation). For Banne D'Ordanche no δ^7Li_{bulk} is available but as a mean basaltic value 3.5 ‰ is proposed as initial for the modeling. The initial isotopic composition of the crystals is assumed to be homogeneous and the isotopic composition of the melt to be constant during fractional crystallization (e.g. Tomascak et al., 1999b). Notably, as the origin of some of the crystals cannot be clearly located the initial Li isotope composition of the potential xenocrysts is uncertain and may as well be different from that of basalts. Notably, mantle olivine may have heterogeneous heterogeneously δ^7Li, which is ascribed to metasomatic overprinting (e.g. Nishio et al., 2004; Tang et al., 2012; Ackerman et al., 2013; Su et al., 2016).

4.6.2 Two diffusive events and boundary conditions

First diffusive event: The boundary conditions of diffusion in system are described as the concentrations or flux at the crystal surface (Costa et al., 2008). Furthermore, the system characteristic (open or closed system) has to be considered (Costa et al., 2008). For the model applied here an open system is assumed due to the quasi-endless supply of Li from the surrounding melt. In order to estimate the diffusivity of Li in olivine,

Chapter 4: Multi-stage magma evolution in intra-plate volcanoes: Insights from combined *in situ* Li and Mg-Fe chemical and isotopic diffusion profiles in olivine

which is less well known than that of Mg-Fe (Dohmen et al., 2007), the Li concentration and Li isotope profiles were modeled by taking the timescales as outlined in (Oeser et al., 2015) for Mg-Fe exchange diffusion. These timescales (BdOr1_ol2 239 days, BdOr1_olxen2 252 days, St3-3a_ol1 3.26 years) are suspected to display the residence time of the crystals in a magma reservoir. As Li core concentration (C_{core}) the initial concentration calculated above is applied and in some cases it is adapted to fit the measured profile, which is justified by the uncertainty of the origin of the crystals. The Li rim concentration (C_{rim1}) of 3.5 to 21 µg/g is applied in the same way to fit the measured profile (Table 4.2). With this fixed time information the diffusion coefficient D_{Li} and the β-value are fitted to receive congruent modeled and measured Li diffusion profiles. The here applied model widely reproduces the low Li isotope compositions observed for the olivine cores (Figure 4.4). However, the modeled Li concentrations are not matching the rim area of the olivines and the Li isotope composition is not matching the measured values yet. The change in slope of the Li concentration profile in Figure 4.2 (c) indicates that the flux of Li into the crystal (assumed in the first diffusive event) changed at some point of time to a flux of Li out of the crystal (second diffusive event) (Figure 4.3). The latter is not visible in all Li concentration profiles but due to the small spatial scales of the samples it may have affected all olivine crystals to some extent. Due to these findings a second diffusive event likely has affected the Massif Central olivines investigated in this study.

Second diffusive event: In order to fit the rim concentration along with the rim isotopic composition a second diffusive step is proposed with the same diffusivity, as determined by modeling of the first diffusion event, but changing rim concentration (C_{rim2}) (Figure 4.3). C_{rim2} is presumed on the basis of the bulk rock Li concentration of the samples (5.78 µg/g for St6-2b, 5.7 µg/g for St3-3a and 6.14 µg/g for BdOr-1; Oeser et al. (2015)) and slightly adapted to fit the model (Table 4.2). The duration of this second diffusive event (now unknown) can be modeled by fitting the Li isotope profile and yields durations of 20 to 80 days for Banne D'Ordanche and 100 to 200 days for St3-3a from Roche Sauterre and 30 to 120 days for St6-2b from Roche Sauterre (Figure 4.4).

Chapter 4: Multi-stage magma evolution in intra-plate volcanoes: Insights from combined *in situ* Li and Mg-Fe chemical and isotopic diffusion profiles in olivine
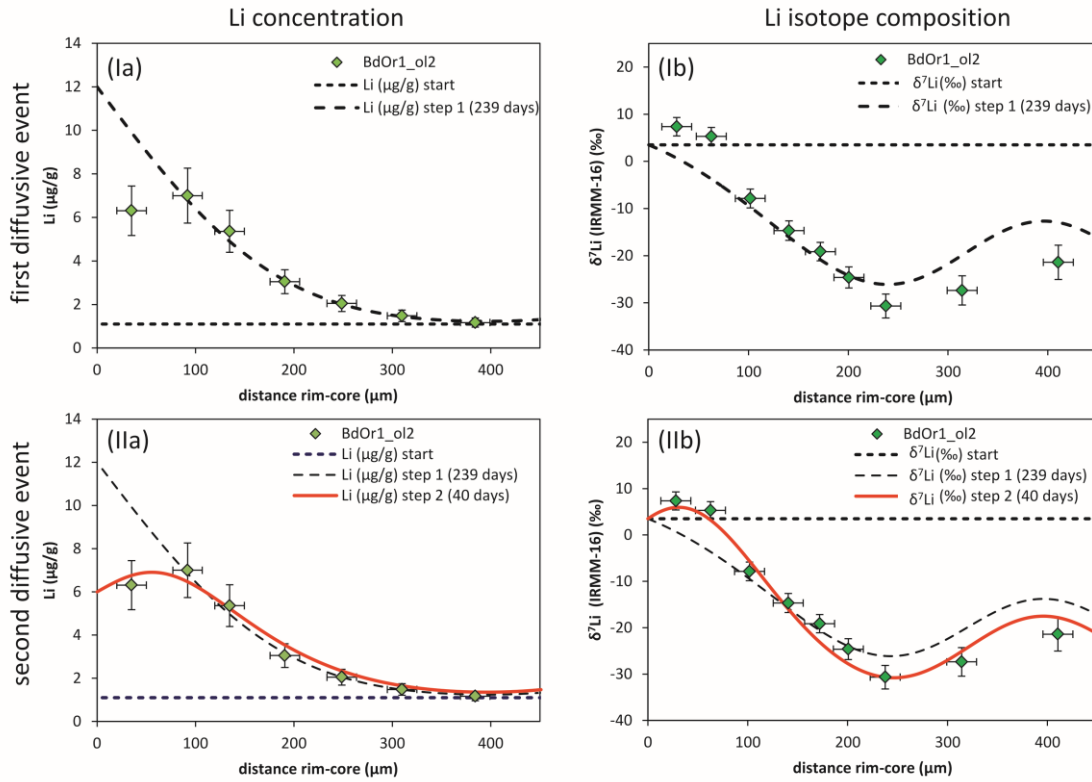
Figure 4.3: (Ia) and (Ib) show the Li concentration and isotopic composition of the first diffusive event for BdOr1_ol2 with a duration of t=239 days, C_{core}=1.1 µg/g, C_{rim1}=12 µg/g and β=0.25 (IIa) and (IIb) show the model for the second diffusive event (which is based on the first diffusive event) with t=40 days, C_{rim2}=6 µg/g and β=0.2, the diffusion coefficient is fit to $5.5*10^{-16}$ m²/s.

As a result of Li diffusion out of the crystals, C_{rim2} for the second diffusive event is lower than C_{rim1} of the first diffusive event, likely caused by a decrease of Li concentration in the melt. During the exsolution of H_2O-rich vapor in the course of decompression Li is largely mobilized in magmatic systems (Sakuyama and Kushiro, 1979). Neukampf et al. (2019) discovered the fractionation of Li isotopes in plagioclases due to degassing of the magma accompanied by lighter δ^7Li-values in the cores than in the rims of their plagioclase crystals and decreasing Li concentrations towards the cores. Due to the mobile character of Li in the vapor phase the Li concentration in the melt decreases which causes Li-depletion around the olivine crystals and a chemical gradient develops. This conducts diffusion to act in the opposite way to that of the first diffusive event, i.e. a flux of Li out of the olivine crystals. Furthermore, the second event with lower concentration is not visible in the Mg-Fe zonation. In the course of the eruption or movement to a shallower level in a dynamic plumbing system degassing might have caused this trend which would be visible for Li

Chapter 4: Multi-stage magma evolution in intra-plate volcanoes: Insights from combined *in situ* Li and Mg-Fe chemical and isotopic diffusion profiles in olivine

but not so for non-fluid-mobile elements, such as Fe and Mg. Hence, in Li isotopes a process might be revealed which cannot be seen in Mg-Fe isotopes and concentrations due to the different chemical properties and the duration of the events. Some profiles are not matched perfectly by the modeled curve. In this case effects from cutting the olivine crystals possibly play a role (Weyrauch et al., 2019), this seems to be indicated by the complete transection of St6-2b_ol5, which is not symmetrical (Figure 4.4).

The time scales of the second diffusive event determined by diffusion modeling in this study are longer (20-80 days for Banne D'Ordanche and 30-200 days for Roche Sauterre) compared to the time scales obtained by Lynn et al. (2018) for the Keanakāko'i Tephra. The authors conclude a similar process of syneruptive degassing in their study with time scales of only hours to days from Li diffusion modeled with Eq. (4.4) which is 11-78 times faster than with the fitted values in this study (Table 4.3). Consequently, the determined time scales of the degassing process are differing due to the applied diffusion coefficients. In this study, the same diffusion coefficient has been assumed for both diffusion steps in this study, however, as it may depend on temperature but also fO_2 and the fluid content in the melt (Laurence A Coogan et al., 2005; Dohmen et al., 2007). Hence, there are uncertainties regarding the applied diffusion coefficients which might be underestimated for the degassing scenario. This means that the time scales obtained in our study for the degassing process represent a conservative estimate for the duration of this event. Lithium diffusivity during the second event may have been faster which would result in smaller time scales.

Table 4.2: Modeling parameters of the first and second diffusive event. Note that for the first diffusion event t was fixed Oeser et al. (2015) and D was fitted, while for the second diffusion event t was the model outcome

	t_{step1} (days)[+]	D_{fit} (m²/s)	δ^7Li_{start} (‰)	C_{core} (µg/g)	C_{rim1} (µg/g)	β_{step1}	C_{rim2} (µg/g)	β_{step2}	t_{step2} (days)
BdOr1-ol1*	~ 239	$2*10^{-16}$	3.5	1.2	11	0.15	6	0.15	20-40
BdOr1-ol2	~ 239	$5*10^{-16}$	3.5	1.1	12	0.23	6	0.25	20-60
BdOr1-olxen1	~ 252	$4.5*10^{-16}$	3.5	7	21	0.2	8	0.2	40-80
BdOr1-olxen2	~ 252	$3.5*10^{-16}$	3.5	2	10	0.15	8	0.2	20-60
St3-3a_ol1	~ 1190	$2.5*10^{-16}$	2.3	1.1	4.5	0.15	3.8	0.25	100-200
St3-3a_ol2	~ 1190	$3.0*10^{-16}$	2.3	0.7	3.5	0.19	2.5	0.25	100-200
St6-2b_ol4	~ 1190	$2.0*10^{-16}$	3.3	2.8	9/7.5[#]	0.22	5/3[#]	0.2	60-120
St6-2b_ol5	~ 1190	$5.0*10^{-16}$	3.3	2.2	6.5	0.2	5.5	0.25	30-90

* BdOr1-ol1 was modeled in a 3-step model with an additional step 0 before step 1 with C_{rim0}=5 µg/g, β_{step0}=0.25 and t_{step0}=2760 days

[+] t_{step1} durations were taken from Oeser et al. (2015)

[#] St6-2b_ol4 war measured from rim to rim, for modeling C_{rim} was adjusted relative to $C_{measured}$

Chapter 4: Multi-stage magma evolution in intra-plate volcanoes: Insights from combined *in situ* Li and Mg-Fe chemical and isotopic diffusion profiles in olivine
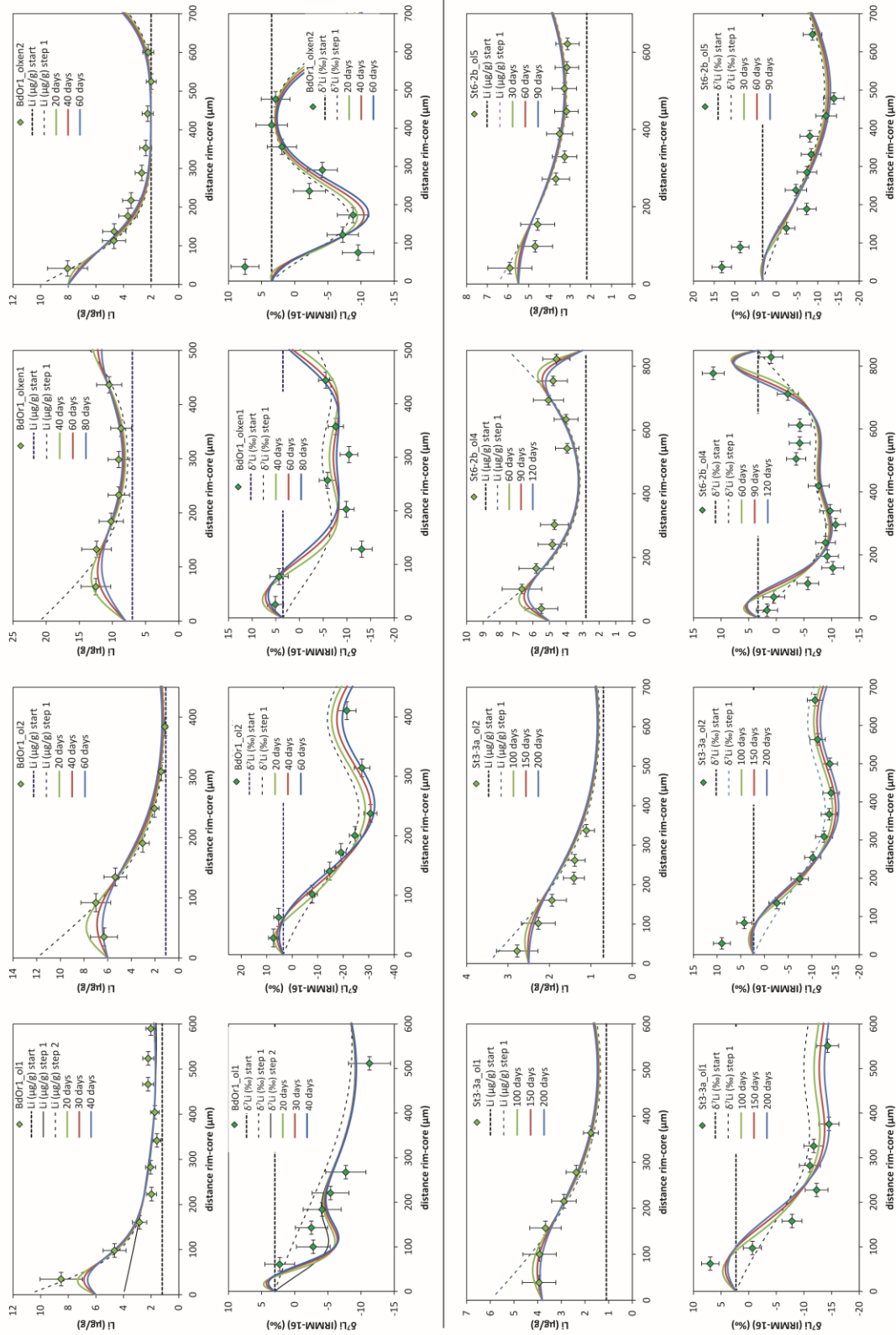

Figure 4.4: Lithium concentration and Li isotope profiles fitted with t=239-252 days for Banne D'Ordanche (BdOr1 samples) and t=3.26 years for Roche Sauterre (St3-3a and St6-2b samples).

Chapter 4: Multi-stage magma evolution in intra-plate volcanoes: Insights from combined *in situ* Li and Mg-Fe chemical and isotopic diffusion profiles in olivine

The β-values for Li determined in this study do not exceed 0.25 which is lower than the β-values of 0.4 ±0.1 determined by (Richter et al., 2017) for the crystallographic a- and c-axes (somewhat lower along the b-axis) and also than that which was modeled by the same authors for a natural olivine (β=0.3-0.36). The β-values obtained in the model in this study indicates a 1.6 % (β=0.1) to 3.9 % (β=0.25) higher relative diffusivity of ^{6}Li as compared to ^{7}Li. This is more similar to the results of Dohmen et al. (2010), who determined a ~3 % faster diffusion of ^{6}Li relative to ^{7}Li in their experiments which corresponds to β=0.19.

4.6.3   Diffusion coefficients

Relative diffusivities are obtained from the equations for the analytical solution in Table A.4.1 and yield D_{Li}/D_{Mg-Fe} ratios of ~2 for BdOr1, which means the diffusivity of Li is twice as fast as the diffusivity of Mg-Fe in BdOr1. For St3-3a and St6-2b the diffusivity of Li is ~1.5 times faster than the diffusivity of Mg-Fe (Figure 4.5).

The parametrization for the determination of the diffusion coefficient of Mg-Fe diffusion in olivine by Dohmen and Chakraborty (2007) depends on temperature (T), pressure (P), oxygen fugacity (fO$_2$) the mole fraction of the fayalite component (X_{Fe}), and the crystallographic orientation of the measured profile. With Eq. (4.3) and the relative diffusivities of Mg-Fe and Li and the absolute calculated diffusion coefficients for Mg-Fe (D_{Mg-Fe}) the diffusion coefficient for Li (D_{Li}) is obtained (Table 4.3). The experimentally determined diffusion coefficient for Li is obtained according to Eq. (4.4) from Dohmen et al. (2010) at a temperature of 1250 °C (Figure 4.6). Though, experimentally determined diffusion coefficients have been determined in the temperature range of 800°C and 1200°C (Dohmen et al., 2010).

Chapter 4: Multi-stage magma evolution in intra-plate volcanoes: Insights from combined *in situ* Li and Mg-Fe chemical and isotopic diffusion profiles in olivine
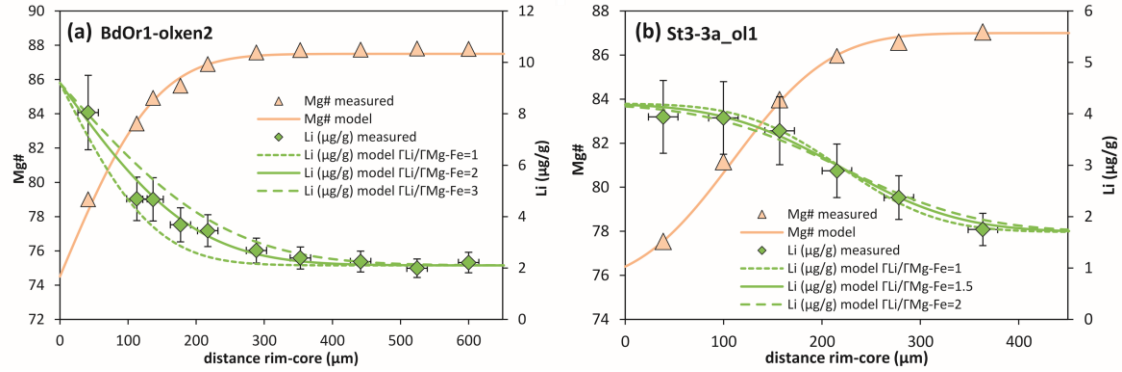
Figure 4.5: Relative modeling of Mg# and Li (µg/g). The Mg# and Li profiles are fitted by adjusting $\Gamma_{Mg\text{-}Fe}$, and Γ_{Li}, respectively. The ratio of the Γ-values is calculated giving the relative diffusivity of Li relative to Mg-Fe. (a) BdOr1-olxen2 is modeled with an infinite analytical approach Figure A.4.1 assuming a fixed rim concentration and (b) St3-3a_ol1 is modeled with a semi-infinite analytical approach assuming the equilibration of two chemically distinct layers of the crystal over time.

Table 4.3: Diffusion coefficients for Li for the relative determination of D_{Li} with Mg-Fe, for the case of fitting D_{Li} and the experimentally determined D_{Li}, all D_{Li}s are compared with $D_{Mg\text{-}Fe}$

	$D_{Mg\text{-}Fe}$ (m²/sec)*	$(D_{Li}/D_{Mg\text{-}Fe})$ relative	$D_{Li\_relative}$ (m²/sec)	D_{Li_fit} (m²/sec)	$(D_{Li}/D_{Mg\text{-}Fe})$ fit	D_{Li_exp} (m²/sec) [#]	$(D_{Li}/D_{Mg\text{-}Fe})$ experimental
BdOr1-ol1	$5.65*10^{-17}$	2.0	$1.13*10^{-16}$	$2*10^{-16}$	3.5	$4.42*10^{-15}$	78.2
BdOr1-ol2	$2.62*10^{-16}$	2.0	$5.24*10^{-16}$	$5*10^{-16}$	2.1	$4.42*10^{-15}$	16.9
BdOr1-olxen1	$3.01*10^{-16}$	2.0	$6.02*10^{-16}$	$4.5*10^{-16}$	1.5	$4.42*10^{-15}$	14.7
BdOr1-olxen2	$7.44*10^{-17}$	2.0	$1.49*10^{-16}$	$3.5*10^{-16}$	4.7	$4.42*10^{-15}$	59.4
St3-3a_ol1	$1.01*10^{-16}$	1.5	$1.51*10^{-16}$	$2.5*10^{-16}$	2.5	$4.42*10^{-15}$	43.9
St3-3a_ol2	$7.53*10^{-17}$	1.5	$1.13*10^{-16}$	$3.0*10^{-16}$	4.0	$4.42*10^{-15}$	58.7
St6-2b_ol4	$9.52*10^{-17}$	1.5	$1.43*10^{-16}$	$2.0*10^{-16}$	2.1	$4.42*10^{-15}$	46.4
St6-2b_ol5	$3.89*10^{-16}$	1.5	$5.84*10^{-16}$	$5.0*10^{-16}$	1.3	$4.42*10^{-15}$	11.4

* calculated at P=500 Pa, T=1250°C, f_{O_2}=NNO-2, crystallographic orientation, X_{Fe} and concentration profiles from

(Oeser et al., 2015)

[#] calculated at 1250°C

Chapter 4: Multi-stage magma evolution in intra-plate volcanoes: Insights from combined *in situ* Li and Mg-Fe chemical and isotopic diffusion profiles in olivine
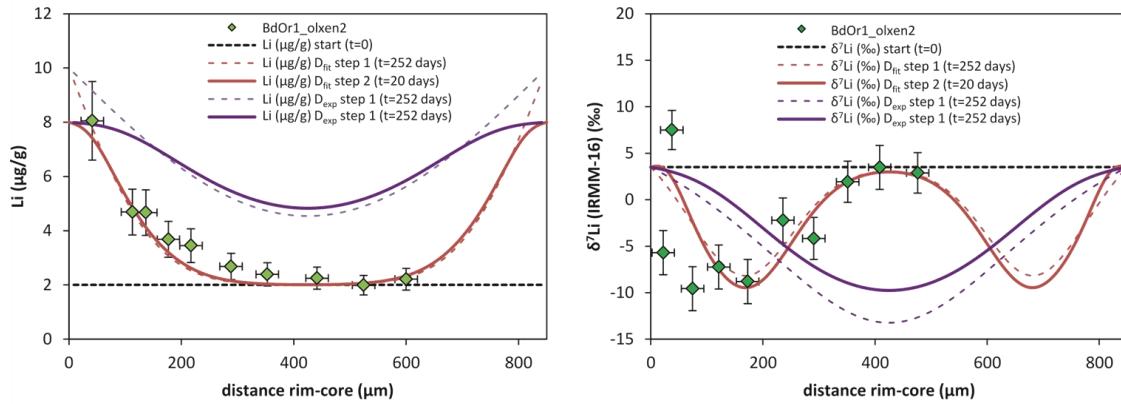

Figure 4.6: Comparison of 2-step model with D$_{fit}$ and D$_{exp}$, as in the model in Figure 4.4, for diffusive event 1 a diffusion time of 239 days is applied, for the second diffusive event 20 days are assumed.

In a recent experimental study Richter et al. (2014) have demonstrated a strong sensitivity of Li diffusion in clinopyroxene to fO_2. Furthermore, Dohmen et al. (2010) imply that the diffusion mechanism of Li in olivine depends on environmental variables, such as fO_2 and $aSiO_2$ (amongst other factors). They have a control on the vacancy concentrations in olivine which are linked to the diffusion mechanism which will be activated (Dohmen et al., 2010). For a series of trace elements in olivine, namely Al, Cr and Be, several studies have been performed with the result of a dependence of diffusivity on factors such as silica activity ($aSiO_2$) and oxygen fugacity (fO_2)(Jollands et al., 2016a; Jollands et al., 2016b; Zhukova et al., 2017). The diffusivity of Al in forsterite at low $aSiO_2$ for example is up to three orders of magnitude slower than at high $aSiO_2$ (Zhukova et al., 2017). These studies show that diffusion in olivine depends on parameters involving the activity and fugacity of SiO_2 and O_2, respectively. A systematic investigation on the influence of fO_2 and $aSiO_2$ could help to better understand the conditions of Li diffusion.

4.7 Conclusion

Combined *in situ* Li concentration and isotope analyses have been successfully applied to analyze zoned olivines from the Massif Central volcanic region. A diffusive origin of Li concentration and isotope profiles is deducted from the correlation with Mg-Fe isotopic inter-diffusion. Two diffusive episodes can be distinguished, with the first one

Chapter 4: Multi-stage magma evolution in intra-plate volcanoes: Insights from combined *in situ* Li and Mg-Fe chemical and isotopic diffusion profiles in olivine

likely representing the (relatively long) residence time of olivine in a (deeper) magma chamber, as implied by Mg-Fe isotope diffusion modeling (Oeser et al., 2015). The first diffusive episode is likely driven by an increase in Li concentration in the melt and also likely by an increase in the partitioning of Li between olivine and melt, potentially as a result of decreasing Mg# during fractional crystallization. This caused Li diffusion into the olivines evoking low δ^7Li-values in the cores of the crystals. A second and shorter diffusion event resulted in Li diffusion out of olivine, indicating a Li decrease in the melt, potentially due to degassing of the melt, resulting in the mobilization of Li into the vapor phase. Such a diffusion event can be deducted by simultaneous modeling of Li concentration and Li isotope profiles. The second diffusive episode is not displayed in the Mg-Fe profiles which highlights that Li profiles contain additional information on the magmatic evolution to those which are received from Mg-Fe modeling, potentially due to the volatile character of Li in magmatic fluids. These findings demonstrate that combining information from chemical and isotopic zoning of Li with those from Fe-Mg is a very powerful tool to unravel the timing of complex magma evolution scenarios, such as commonly observed in magma plumbing systems.

Furthermore, the findings of this study indicate that under natural conditions Li diffusion may be slower than experimentally determined and only slightly faster than that of the major elements Mg and Fe. However, there are presently no systematic studies concerning the dependence of Li diffusivity on parameters, such as the Li concentration, aSiO$_2$ or fO$_2$ indicating a need for further more detailed experimental investigations in order to obtain more reliable information on time scales of magmatic processes from modeling of Li concentration and isotope profiles.

Conclusion and Outlook

Between crystals in magmatic environments and the surrounding melts chemical gradients are developing, when they are in chemical disequilibrium. These gradients evoke a chemical flux of elements into or out of the crystal which results in a kinetic fractionation process - diffusion. Lithium is susceptible to chemical re-equilibration due to its physical and chemical properties. Its moderately incompatible character causes an increase in concentration in a differentiating melt at the early magmatic stages, resulting in diffusion of Li into the crystals. In the pre- or syneruptive stage Li is susceptible to volatilization into the fluid or vapor phase, which results in a decrease of Li concentration, Li diffusion out of the crystals, and hence an opposite process at late magmatic stages. These processes, the early and as well the late magmatic process, can be observed in the Li chemical and isotope composition of olivine. The more established Mg-Fe diffusion couple, in contrast, is only able to display differentiation but not degassing-induced concentration and isotopic changes. Diffusion at magmatic temperatures is in the here investigated samples largely visible on the mineral scale, whereas isotopic variations on the outcrop scale could not be observed.

Chemical and isotopic profiles can be modeled by the established diffusion equations. By adjusting the diffusion coefficients a fitting of measured and modeled traverses from the rims to the cores of olivines crystals can be achieved. The approach to determine diffusion coefficients in this study depends on the relative diffusivity of Li to Mg-Fe. The diffusion coefficients, which are obtained from natural samples, are lower compared to those from experimental studies. Fitting the profiles is possible by applying a two-step diffusion process which contains the enrichment of Li in the melt and diffusion into the crystal in the first, relatively long-lasting event, and the decrease of Li and diffusion out of the crystal in the second, short-lived and presumably pre- or synerupive degassing event. The reconstruction of the magmatic evolution history thus is enhanced by the opportunity of analyzing the versatile element of Li.

Though many years of research on Li have been conducted, there is still a broad field with great potential, especially regarding the characteristics of Li diffusion in high temperature environments. The constriction of diffusion coefficients at varying conditions (e.g. fO$_2$, aSiO$_2$, matrix elements, crystal structures and different concentration levels) needs to be further evaluated, in order to reduce the uncertainty when determining time scales of Li diffusion. Furthermore, besides olivine and plagioclase, pyroxenes are important Li carriers in volcanic rock suites and the data base of all these minerals is still expandable.

References

<div style="text-align: right">

References

</div>

Abdelfadil K. M., Romer R. L. and Glodny J. (2014) Mantle wedge metasomatism revealed by Li isotopes in orogenic lamprophyres. *Lithos* **196**–**197**, 14–26.

Ackerman L., Medaris Jr. G., Špaček P. and Ulrych J. (2015) Geochemical and petrological constraints on mantle composition of the Ohře(Eger) rift, Bohemian Massif: peridotite xenoliths from the České Středohoří Volcanic complex and northern Bohemia. *Int. J. Earth Sci.* **104**, 1957–1979.

Ackerman L., Špaček P., Magna T., Ulrych J., Svojtka M., Hegner E. and Balogh K. (2013) Alkaline and carbonate-rich melt metasomatism and melting of subcontinental lithospheric mantle: Evidence from mantle xenoliths, ne bavaria, bohemian massif. *J. Petrol.* **54**, 2597–2633.

Albert H., Costa F. and Martí J. (2014) Timing of magmatic processes and unrest associated with mafic historical monogenetic eruptions in Tenerife Island. *J. Petrol.* **56**, 1945–1966.

Ammannati E., Jacob D. E., Avanzinelli R., Foley S. F. and Conticelli S. (2016) Low Ni olivine in silica-undersaturated ultrapotassic igneous rocks as evidence for carbonate metasomatism in the mantle. *Earth Planet. Sci. Lett.* **444**, 64–74.

Ariskin A. A., Barmina G. S., Ozerov A. Y. and Nielsen R. L. (1995) Genesis of High-Alumina Basalts from Klyuchevskoi Volcano. *Petrology* **3**, 449–472.

Batanova V. G., Thompson J. M., Danyushevsky L. V., Portnyagin M. V., Garbe-Schönberg D., Hauri E., Kimura J. I., Chang Q., Senda R., Goemann K., Chauvel C., Campillo S., Ionov D. A. and Sobolev A. V. (2019) New Olivine Reference Material for In Situ Microanalysis. *Geostand. Geoanalytical Res.* **43**, 453–473.

Beck P., Barrat J. A., Chaussidon M., Gillet P. and Bohn M. (2004) Li isotopic variations in single pyroxenes from the Northwest Africa 480 shergottite (NWA 480): A record of degassing of Martian magmas? *Geochim. Cosmochim. Acta* **68**, 2925–2933.

Beck P., Chaussidon M., Barrat J. A., Gillet P. and Bohn M. (2006) Diffusion induced Li isotopic fractionation during the cooling of magmatic rocks: The case of pyroxene phenocrysts from nakhlite meteorites. *Geochim. Cosmochim. Acta* **70**, 4813–4825.

Blundy J. D. and Shimizu N. (1991) Trace element evidence for plagioclase recycling in calc-alkaline magmas. *Earth Planet. Sci. Lett.* **102**, 178–197.

Bouman C., Elliott T. and Vroon P. Z. (2004) Lithium inputs to subduction zones. *Chem. Geol.* **212**, 59–79.

Bouman C., Trinquier A., Lloyd N., Schwieters J., Koornneef J. and Davies G. (2015) New Design 10 13 Ω Amplifiers for Measurement of Small Ion Beam Currents. *Thermo Fish. Sci. Bremen*, 1–2.

Brant C., Coogan L. A., Gillis K. M., Seyfried W. E., Pester N. J. and Spence J. (2012) Lithium and Li-isotopes in young altered upper oceanic crust from the East Pacific Rise. *Geochim. Cosmochim. Acta* **96**, 272–293.

Brenan J. M., Neroda E., Lundstrom C. C., Shaw H. F., Rverson F. J. and Phinney D. L. (1998) Behaviour of boron, beryllium, and lithium during melting and crystallization: constraints from mineral-melt partitioning experiments. *Geochim. Cosmochim. Acta* **62**, 2129–2141.

References

Brooker R. A., James R. H. and Blundy J. D. (2004) Trace elements and Li isotope systematics in Zabargad peridotites: Evidence of ancient subduction processes in the Red Sea mantle. *Chem. Geol.* **212**, 179–204.

Cabato J., Altherr R., Ludwig T. and Meyer H. P. (2013) Li, Be, B concentrations and δ7Li values in plagioclase phenocrysts of dacites from Nea Kameni (Santorini, Greece). *Contrib. to Mineral. Petrol.* **165**, 1135–1154.

Chan L. H., Alt J. C. and Teagle D. A. H. (2002) Lithium and lithium isotope profiles through the upper oceanic crust: A study of seawater-basalt exchange at ODP Sites 504B and 896A. *Earth Planet. Sci. Lett.* **201**, 187–201.

Chan L. H. and Edmond J. M. (1988) Variation of lithium isotope composition in the marine environment: a preliminary report. *Geochim. Cosmochim. Acta* **52**, 1711–1717.

Chan L. H., Edmond J. M., Thompson G. and Gillis K. (1992) Lithium isotopic composition of submarine basalts: implications for the lithium cycle in the oceans. *Earth Planet. Sci. Lett.* **108**, 151–160.

Chan L. H. and Frey F. A. (2003) Lithium isotope geochemistry of the Hawaiian plume: Results from the Hawaii scientific drilling project and Koolau volcano. *Geochemistry, Geophys. Geosystems* **4**, 8707-8727.

Chapman S. and Cowling T. G. (1953) *Mathematical Theory of Non-uniform Gases - An account of the kinetic theory of viscosity, thermal conduction and diffusion in gases*. 3rd ed., Cambridge Mathematical Library, Cambridge, 447p.

Chiarizia R., Horwitz E. P., Alexandratos S. D. and Gula M. J. (1997) Diphonix® resin : A review of its properties and applications. *Sep. Sci. Technol.* **32**, 1-35.

Collinet M., Charlier B., Namur O., Oeser M.,

Médard E., Vander Auwera J. and Weyer S. (2014) Fe and Mg isotope fractionation in olivine from the NWA 1068 shergottite. *Goldschmidt Abstr. 2014* **443**.

Collinet M., Charlier B., Namur O., Oeser M., Médard E. and Weyer S. (2017) Crystallization history of enriched shergottites from Fe and Mg isotope fractionation in olivine megacrysts. *Geochim. Cosmochim. Acta* **207**, 277–297.

Coogan L. A., Gillis K. M., Pope M. and Spence J. (2017) The role of low-temperature (off-axis) alteration of the oceanic crust in the global Li-cycle: Insights from the Troodos ophiolite. *Geochim. Cosmochim. Acta* **203**, 201–215.

Coogan L. A., Hain A., Stahl S. and Chakraborty S. (2005) Experimental determination of the diffusion coefficient for calcium in olivine between 900°C and 1500°C. *Geochim. Cosmochim. Acta* **69**, 3683–3694.

Coogan Laurence A, Kasemann S. A. and Chakraborty S. (2005) Rates of hydrothermal cooling of new oceanic upper crust derived from lithium-geospeedometry. *Earth Planet. Sci. Lett.* **240**, 415–424.

Costa F., Dohmen R. and Chakraborty S. (2008) Time Scales of Magmatic Processes from Modeling the Zoning Patterns of Crystals. *Rev. Mineral. Geochemistry* **69**, 545–594.

Craig G., Hu Z., Zhang A., Lloyd N. S., Bouman C. and Schwieters J. (2017) Dynamic time correction for high precision isotope ratio measurements. *Thermo Fish. Sci. Bremen*, 1–8.

Crank J. (1975) *The Mathematics of Diffusion*. 2nd ed., Clarendon Press, Oxford, 421p.

Deer W. A., Howie R. A. and Zussman J. (2013) *An Introduction to the Rock-forming Minerals*. 3rd ed., The Mineralogical Society, London.

References

Dellinger M., Gaillardet J. Ô., Bouchez J., Calmels D., Galy V., Hilton R. G., Louvat P. and France-Lanord C. (2014) Lithium isotopes in large rivers reveal the cannibalistic nature of modern continental weathering and erosion. *Earth Planet. Sci. Lett.* **401**, 359–372.

DePaolo D. J. (1981) Trace element and isotopic effects of combined wallrock assimilation and fractional crystallization. *Earth Planet. Sci. Lett.* **53**, 189–202.

Dohmen R., Becker H. W. and Chakraborty S. (2007) Fe-Mg diffusion in olivine I: Experimental determination between 700 and 1,200°C as a function of composition, crystal orientation and oxygen fugacity. *Phys. Chem. Miner.* **34**, 389–407.

Dohmen R. and Chakraborty S. (2007) Fe-Mg diffusion in olivine II: Point defect chemistry, change of diffusion mechanisms and a model for calculation of diffusion coefficients in natural olivine. *Phys. Chem. Miner.* **34**, 409–430.

Dohmen R., Kasemann S. A., Coogan L. and Chakraborty S. (2010) Diffusion of Li in olivine. Part I: Experimental observations and a multi species diffusion model. *Geochim. Cosmochim. Acta* **74**, 274–292.

Elliott T., Jeffcoate A. and Bouman C. (2004) The terrestrial Li isotope cycle: Light-weight constraints on mantle convection. *Earth Planet. Sci. Lett.* **220**, 231–245.

Elliott T., Thomas A., Jeffcoate A. and Niu Y. (2006) Lithium isotope evidence for subduction-enriched mantle in the source of mid-ocean-ridge basalts. *Nature* **443**, 565–568.

Fernández B., Claverie F., Pécheyran C. and Donard O. F. X. (2007) Direct analysis of solid samples by fs-LA-ICP-MS. *Trends Anal. Chem.* **26**, 951–966.

Flesch G. D., Anderson A. R. J. and Svec H. J. (1973) A Secondary Isotopic Standard for 6Li/7Li Determinations. *Int. J. Mass Spectrom. Ion Phys.* **12**, 265–272.

Foley S. F., Jacob D. E. and O'Neill H. S. C. (2011) Trace element variations in olivine phenocrysts from Ugandan potassic rocks as clues to the chemical characteristics of parental magmas. *Contrib. to Mineral. Petrol.* **162**, 1–20.

Foley S. F., Prelevic D., Rehfeldt T. and Jacob D. E. (2013) Minor and trace elements in olivines as probes into early igneous and mantle melting processes. *Earth Planet. Sci. Lett.* **363**, 181–191.

Ganguly J. (2002) Diffusion kinetics in minerals: Principles and applications to tectono-metamorphic processes. *EMU Notes Mineral. Energy Model. Miner.* **4**, 271–309.

Ginibre C., Wörner G. and Kronz A. (2007) Crystal zoning as an archive for magma evolution. *Elements* **3**, 261–266.

Giuffrida M., Viccaro M. and Ottolini L. (2018) Ultrafast syn-eruptive degassing and ascent trigger high-energy basic eruptions. *Sci. Rep.* **8**, 1–7.

Gu X., Deloule E., France L. and Ingrin J. (2016) Multi-stage metasomatism revealed by trace element and Li isotope distributions in minerals of peridotite xenoliths from Allègre volcano (French Massif Central). *Lithos* **264**, 158–174.

Hamelin C., Seitz H. M., Barrat J. A., Dosso L., Maury R. C. and Chaussidon M. (2009) A low δ7Li lower crustal component: Evidence from an alkalic intraplate volcanic series (Chaîne des Puys, French Massif Central). *Chem. Geol.* **266**, 205–217.

Hansteen T. H., Klügel A. and Schmincke H. U. (1998) Multi-stage magma ascent beneath the Canary Islands: Evidence from fluid inclusions. *Contrib. to Mineral. Petrol.* **132**, 48–64.

Heinrichs H. (1989) Aufschlussverfahren in der Analytischen Geochemie (Teil 1). *LaborPraxis* **12**, 1–6.

References

Hergenröder R. (2006) Hydrodynamic sputtering as a possible source for fractionation in LA-ICP-MS. *J. Anal. At. Spectrom.* **21**, 517–524.

Heumann K. G., Gallus S. M., Rädlinger G. and Vogl J. (1998) Precision and accuracy in isotope ratio measurements by plasma source mass spectrometry. *J. Anal. At. Spectrom.* **13**, 1001–1008.

Holzapfel C., Chakraborty S., Rubie D. C. and Frost D. J. (2007) Effect of pressure on Fe-Mg, Ni and Mn diffusion in (Fe x Mg 1-x) 2 SiO 4 olivine. *Phys. Earth Planet. Inter.* **162**, 186–198.

Horn I. (2008) Comparison of femtosecond and nanosecond laser interactions with geologic matrices and their influence on accuracy and precision of LA-ICP-MS data. In *Laser Ablation ICP-MS in the Earth Sciences: Current Practices and Outstanding Issues* (ed. P. Sylvester). Mineralogical Association Canada, Vancouver. pp. 53–65.

Horn I. and von Blanckenburg F. (2007) Investigation on elemental and isotopic fractionation during 196 nm femtosecond laser ablation multiple collector inductively coupled plasma mass spectrometry. *Spectrochim. Acta Part B At. Spectrosc.* **62**, 410–422.

Horn I., von Blanckenburg F., Schoenberg R., Steinhoefel G. and Markl G. (2006) In situ iron isotope ratio determination using UV-femtosecond laser ablation with application to hydrothermal ore formation processes. *Geochim. Cosmochim. Acta* **70**, 3677–3688.

Huh Y., Chan L.-H., Zhang L. and Edmond J. M. (1998) Lithium and its isotopes in major world rivers: implications for weathering and the oceanic budget. *Geochim. Cosmochim. Acta* **62**, 2039–2051.

Ionov D. A. and Seitz H.-M. (2008) Lithium abundances and isotopic compositions in mantle xenoliths from subduction and intra-plate settings: Mantle sources vs. eruption histories. *Earth Planet. Sci. Lett.* **266**, 316–331.

Ito M. and Ganguly J. (2006) Diffusion kinetics of Cr in olivine and 53Mn-53Cr thermochronology of early solar system objects. *Geochim. Cosmochim. Acta* **70**, 799–809.

Jackson S. E. (2008) LAMTRACE Data Reduction Software for LA-ICP-MS. In *Laser Ablation ICP-MS in the Earth Sciences: Current Practices and Outstanding Issues* (ed. P. Sylvester). Mineralogical Association Canada. pp. 305–307.

Jackson S. E. and Günther D. (2003) The nature and sources of laser induced isotopic fractionation in laser ablation-multicollector-inductively coupled plasma-mass spectrometry. *J. Anal. At. Spectrom.* **18**, 205–212.

James R. H. and Palmer M. R. (2000) The lithium isotope composition of international rock standards. *Chem. Geol.* **166**, 319–326.

Jan M. Q. and Khan M. A. (1996) Petrology of gem peridot from Sapat mafic-ultramafic complex, Kohistan, NW Himalaya. *J. Himal. Earth Sci.* **29**, 17–26.

Jarosewich E., Nelen J. A. and Norbers J. A. (1980) Reference Samples for Electron Microprobe Analysis. *Geostand. Newsl.* **4**, 43–47.

Jeffcoate A. B., Elliott T., Kasemann S. A., Ionov D., Cooper K. and Brooker R. (2007) Li isotope fractionation in peridotites and mafic melts. *Geochim. Cosmochim. Acta* **71**, 202–218.

Jeffcoate A. B., Elliott T., Thomas A. and Bouman C. (2004) Precise , Small Sample Size Determinations of Lithium Isotopic Compositions of Geological Reference Materials and Modern Seawater by MC-ICP-MS. *Geostand. Geoanalytical Res.* **28**, 161–172.

References

Jochum K. P. and Stoll B. (2008) Reference materials for elemental and isotopic analyses by LA-(MC)-ICP-MS: successes and outstanding needs. In *Laser Ablation ICP-MS in the Earth Sciences: Current Practices and Outstanding Issues* (ed. P. Sylvester). Vancouver. pp. 147–168.

Jochum K. P., Stoll B., Herwig K., Willbold M., Hofmann A. W., Amini M., Aarburg S., Abouchami W., Hellebrand E., Mocek B., Raczek I., Stracke A., Alard O., Bouman C., Becker S., Dücking M., Brätz H., Klemd R., De Bruin D., Canil D., Cornell D., De Hoog C.-J., Dalpé C., Danyushevshy L., Eisenhauer A., Gao Y., Snow J. E., Groschopf N., Günther D., Latkoczy C., Guillong M., Hauri E. H., Höfer H. E., Lahaye Y., Horz K., Jacob D. E., Kasemann S. A., Kent A. J. R., Ludwig T., Zack T., Mason P. R. D., Meixner A., Rosner M., Misawa K., Nash B. P., Pfänder J., Premo W. R., Sun W. D., Tiepolo M., Vannucci R., Vennemann T., Wayne D. and Woodhead J. D. (2006) MPI-DING reference glasses for in situ microanalysis: New reference values for element concentrations and isotope ratios. *Geochemistry, Geophys. Geosystems* **7**, 1–44.

Jochum K. P., Wilson S. A., Abouchami W., Amini M., Chmeleff J., Eisenhauer A., Hegner E., Iaccheri L. M., Kieffer B., Krause J., Mcdonough W. F., Mertz-Kraus R., Raczek I., Rudnick R. L., Scholz D., Steinhoefel G., Stoll B., Stracke A., Tonarini S., Weis D., Weis U. and Woodhead J. D. (2011) GSD-1G and MPI-DING Reference Glasses for In Situ and Bulk Isotopic Determination. *Geostand. Geoanalytical Res.* **35**, 193–226.

Jollands M. C., Burnham A. D., O'Neill H. S. C., Hermann J. and Qian Q. (2016a) Beryllium diffusion in olivine: A new tool to investigate timescales of magmatic processes. *Earth Planet. Sci. Lett.* **450**, 71–82.

Jollands M. C., Hermann J., St. O'Neill H. C., Spandler C. and Padrón-Navarta J. A. (2016b) Diffusion of Ti and some divalent cations in olivine as a function of temperature, oxygen fugacity, chemical potentials and crystal orientation. *J. Petrol.* **57**, 1983–2010.

Jollands M. C., O'Neill H. S. C., Van Orman J., Berry A. J., Hermann J., Newville M. and Lanzirotti A. (2018) Substitution and diffusion of Cr2+ and Cr3+ in synthetic forsterite and natural olivine at 1200–1500 °C and 1 bar. *Geochim. Cosmochim. Acta* **220**, 407–428.

Kahl M., Chakraborty S., Costa F. and Pompilio M. (2011) Dynamic plumbing system beneath volcanoes revealed by kinetic modeling, and the connection to monitoring data: An example from Mt. Etna. *Earth Planet. Sci. Lett.* **308**, 11–22.

Kahl M., Chakraborty S., Costa F., Pompilio M., Liuzzo M. and Viccaro M. (2013) Compositionally zoned crystals and real-time degassing data reveal changes in magma transfer dynamics during the 2006 summit eruptive episodes of Mt. Etna. *Bull. Volcanol.* **75**, 1–14.

Kahl M., Chakraborty S., Pompilio M. and Costa F. (2015) Constraints on the nature and evolution of the magma plumbing system of Mt. Etna volcano (1991-2008) from a combined thermodynamic and kinetic modelling of the compositional record of minerals. *J. Petrol.* **56**, 2025–2068.

Kasemann S. A., Jeffcoate A. B. and Elliott T. (2005) Lithium isotope composition of basalt glass reference material. *Anal. Chem.* **77**, 5251–5257.

Kersting A. B. and Arculus R. J. (1994) Klyuchevskoy volcano, kamchatka, Russia: The role of high-flux recharged, tapped, and fractionated magma chamber(s) in the genesis of high-Al2O3 from high-MgO basalt. *J. Petrol.* **35**, 1–41.

Kimura J.-I., Chang Q., Kanazawa N., Sasaki S. and Vaglarov B. S. (2016) High-precision in situ analysis of Pb isotopes in glasses using 1013 Ω resistor high gain amplifiers with ultraviolet femtosecond laser ablation multiple Faraday collector inductively coupled plasma mass

References

spectrometry. *J. Anal. At. Spectrom.* **31**, 790–800.

Kisakurek B., Widdowson M. and James R. H. (2004) Behaviour of Li isotopes during continental weathering: The Bidar laterite profile, India. *Chem. Geol.* **212**, 27–44.

Kobayashi K., Tanaka R., Moriguti T., Shimizu K. and Nakamura E. (2004) Lithium, boron, and lead isotope systematics of glass inclusions in olivines from Hawaiian lavas: Evidence for recycled components in the Hawaiian plume. *Chem. Geol.* **212**, 143–161.

Koornneef J. M., Bouman C., Schwieters J. B. and Davies G. R. (2014) Analytica Chimica Acta Measurement of small ion beams by thermal ionisation mass spectrometry using new 10 13 Ohm resistors. *Anal. Chim. Acta* **819**, 49–55.

Košler J., Kučera M. and Sylvester P. (2001) Precise measurement of Li isotopes in planktonic foraminiferal tests by quadrupole ICPMS. *Chem. Geol.* **181**, 169–179.

Kramida A. E. and Ryabtsev A. N. (2007) A critical compilation of energy levels and spectral lines of neutral boron. *Phys. Scr.* **76**, 544–557.

Krienitz M. S., Garbe-schönberg C. D., Romer R. L., Meixner A., Haase K. M. and Stroncik N. A. (2012) Lithium isotope variations in ocean Island Basalts-implications for the development of mantle heterogeneity. *J. Petrol.* **53**, 2333–2347.

Kroslakova I. and Günther D. (2007) Elemental fractionation in laser ablation-inductively coupled plasma-mass spectrometry: evidence for mass load induced matrix effects in the ICP during ablation of a silicate glass. *J. Anal. At. Spectrom.* **22**, 51–62.

Kuritani T. and Nakamura E. (2006) Elemental fractionation in lavas during post-eruptive degassing: Evidence from trachytic lavas, Rishiri Volcano, Japan. *J. Volcanol. Geotherm. Res.* **149**, 124–138.

Lazarov M. and Horn I. (2015) Matrix and energy effects during in-situ determination of Cu isotope ratios by ultraviolet-femtosecond laser ablation multicollector inductively coupled plasma mass spectrometry. *Spectrochim. Acta Part B At. Spectrosc.* **111**, 64–73.

Lemarchand E., Chabaux F., Vigier N., Millot R. and Pierret M. C. (2010) Lithium isotope systematics in a forested granitic catchment (Strengbach, Vosges Mountains, France). *Geochim. Cosmochim. Acta* **74**, 4612–4628.

Lin J., Liu Y., Tong X., Zhu L., Zhang W. and Hu Z. (2017) Improved in situ Li isotopic ratio analysis of silicate by optimizing signal intensity, isotopic ratio stability and intensity matching using ns-LA-MC-ICP-MS. *J. Anal. At. Spectrom.* **32**, 834–842.

Liu S. A., Teng F. Z., Yang W. and Wu F. Y. (2011) High-temperature inter-mineral magnesium isotope fractionation in mantle xenoliths from the North China craton. *Earth Planet. Sci. Lett.* **308**, 131–140.

Liu X. M., Rudnick R. L., McDonough W. F. and Cummings M. L. (2013) Influence of chemical weathering on the composition of the continental crust: Insights from Li and Nd isotopes in bauxite profiles developed on Columbia River Basalts. *Geochim. Cosmochim. Acta* **115**, 73–91.

Lloyd N. S. ., Sadekov A. Y. and Misra S. (2018) Application of 10 13 ohm Faraday cup current amplifiers for boron isotopic analyses by solution mode and laser ablation multicollector inductively coupled plasma mass spectrometry. *Rapid Commun. Mass Spectrom.* **32**, 9–18.

Longerich H. P. (1989) Mass Spectrometric Determination of the Temperature of an Argon Inductively Coupled Plasma From the Formation of the Singly Charged Monoxide Rare Earths and their Known Dissociation Energies. *J. Anal. At. Spectrom.* **4**, 491–497.

Longerich H. P., Jackson S. E. and Günther D. (1996) Laser ablation inductively coupled

References

plasma mass spectrometric transient signal data acquisition and analyte concentration calculation. *J. Anal. At. Spectrom.* **11**, 899–904.

Lorand J. P., Alard O., Luguet A. and Keays R. R. (2003) Sulfur and selenium systematics of the subcontinental lithospheric mantle: Inferences from the Massif Central xenolith suite (France). *Geochim. Cosmochim. Acta* **67**, 4137–4151.

Lundstrom C. C., Chaussidon M., Hsui A. T., Kelemen P. and Zimmerman M. (2005) Observations of Li isotopic variations in the Trinity Ophiolite: Evidence for isotopic fractionation by diffusion during mantle melting. *Geochim. Cosmochim. Acta* **69**, 735–751.

Lynn K. J., Shea T., Garcia M. O., Costa F. and Norman M. D. (2018) Lithium diffusion in olivine records magmatic priming of explosive basaltic eruptions. *Earth Planet. Sci. Lett.* **500**, 127–135.

Magna T., Ionov D. A., Oberli F. and Wiechert U. (2008) Links between mantle metasomatism and lithium isotopes: Evidence from glass-bearing and cryptically metasomatized xenoliths from Mongolia. *Earth Planet. Sci. Lett.* **276**, 214–222.

Magna T., Wiechert U. and Halliday A. N. (2006) New constraints on the lithium isotope compositions of the Moon and terrestrial planets. *Earth Planet. Sci. Lett.* **243**, 336–353.

Marks M. A. W., Rudnick R. L., McCammon C., Vennemann T. and Markl G. (2007) Arrested kinetic Li isotope fractionation at the margin of the Ilímaussaq complex, South Greenland: Evidence for open-system processes during final cooling of peralkaline igneous rocks. *Chem. Geol.* **246**, 207–230.

Marschall H. R., Altherr R. and Rüpke L. (2007a) Squeezing out the slab - modelling the release of Li, Be and B during progressive high-pressure metamorphism.

Chem. Geol. **239**, 323–335.

Marschall H. R., Pogge von Strandmann P. A. E., Seitz H. M., Elliott T. and Niu Y. (2007b) The lithium isotopic composition of orogenic eclogites and deep subducted slabs. *Earth Planet. Sci. Lett.* **262**, 563–580.

McDade P., Blundy J. D. and Wood B. J. (2003) Trace element partitioning on the Tinaquillo solidus at 1.5 GPa. *Phys. Earth Planet. Inter.* **139**, 129–147.

Millot R., Guerrot C. and Vigier N. (2004a) Accurate and high-precision measurement of lithium isotopes in two reference materials by MC-ICP-MS. *Geostand. Geoanalytical Res.* **28**, 153–159.

Millot R., Guerrot C. and Vigier N. (2004b) Accurate and high-precision measurement of lithium isotopes in two reference materials by MC-ICP-MS. *Geostand. Geoanalytical Res.* **28**, 153–159.

Millot R., Scaillet B. and Sanjuan B. (2010) Lithium isotopes in island arc geothermal systems: Guadeloupe, Martinique (French West Indies) and experimental approach. *Geochim. Cosmochim. Acta* **74**, 1852–1871.

Moriguti T., Shibata T. and Nakamura E. (2004) Lithium, boron and lead isotope and trace element systematics of Quaternary basaltic volcanic rocks in northeastern Japan: Mineralogical controls on slab-derived fluid composition. *Chem. Geol.* **212**, 81–100.

Nehlig P., Boivin P., de Goër A., Mergoil J., Poutrau G., Sustrac G. and Thiéblemont D. (2001) Les volcans du Massif Central. *Géologues* **130/131**, 66–91.

Neukampf J., Ellis B. S., Laurent O., Steinmann L. K., Dohmen R., Ubide T., Oeser M., Magna T., Weyer S. and Bachmann O. (2019) Timescales of degassing in rhyolitic magmas tracked by Li in plagioclase. *Goldschmidt Abstr. 2019*.

References

Nishio Y., Nakai S., Ishii T. and Sano Y. (2007) Isotope systematics of Li, Sr, Nd, and volatiles in Indian Ocean MORBs of the Rodrigues Triple Junction: Constraints on the origin of the DUPAL anomaly. *Geochim. Cosmochim. Acta* **71**, 745–759.

Nishio Y., Nakai S., Yamamoto J., Sumino H., Matsumoto T., Prikhod'ko V. S. and Arai S. (2004) Lithium isotopic systematics of the mantle-derived ultramafic xenoliths: Implications for EM1 origin. *Earth Planet. Sci. Lett.* **217**, 245–261.

Oeser-Rabe M. (2015) Constraints on the Evolution of Magmas from Diffusion-driven Chemical and Fe-Mg Isotopic Zoning in Natural Olivines analyzed by Femtosecond-LA-ICP-MS.,

Oeser M., Dohmen R., Horn I., Schuth S. and Weyer S. (2015) Processes and time scales of magmatic evolution as revealed by Fe–Mg chemical and isotopic zoning in natural olivines. *Geochim. Cosmochim. Acta* **154**, 130–150.

Oeser M., Ruprecht P. and Weyer S. (2018) Combined Fe-Mg chemical and isotopic zoning in olivine constraining magma mixing-to-eruption timescales for the continental arc volcano Irazú (Costa Rica) and Cr diffusion in olivine. *Am. Mineral.* **103**, 582–599.

Oeser M., Weyer S., Horn I. and Schuth S. (2014) High-precision fe and mg isotope ratios of silicate reference glasses determined in situ by femtosecond LA-MC-ICP-MS and by solution nebulisation MC-ICP-MS. *Geostand. Geoanalytical Res.* **38**, 311–328.

Ottolini L., Laporte D., Raffone N., Devidal J.-L. and Le Fèvre B. (2009) New experimental determination of Li and B partition coefficients during upper mantle partial melting. *Contrib. to Mineral. Petrol.* **157**, 313–325.

Palm W. J. I. (2005) *System Dynamics*. 2nd ed., McGraw Hill, New York, 834p.

Parkinson I. J., Hammond S. J., James R. H. and Rogers N. W. (2007) High-temperature lithium isotope fractionation: Insights from lithium isotope diffusion in magmatic systems. *Earth Planet. Sci. Lett.* **257**, 609–621.

Penniston-Dorland S., Liu X.-M. and Rudnick R. L. (2017) Lithium Isotope Geochemistry eds. F. Z. Teng, J. Watkins, and N. Dauphas. *Rev. Mineral. Geochemistry* **82**, 165–217.

Petry C., Chakraborty S. and Palme H. (2004) Experimental determination of Ni diffusion coefficients in olivine and their dependence on temperature, composition, oxygen fugacity, and crystallographic orientation. *Geochim. Cosmochim. Acta* **68**, 4179–4188.

Pistiner J. S. and Henderson G. M. (2003) Lithium-isotope fractionation during continental weathering processes. *Earth Planet. Sci. Lett.* **214**, 327–339.

Pogge von Strandmann P. A. E., Burton K. W., James R. H., van Calsteren P., Gíslason S. R. and Mokadem F. (2006) Riverine behaviour of uranium and lithium isotopes in an actively glaciated basaltic terrain. *Earth Planet. Sci. Lett.* **251**, 134–147.

Pogge von Strandmann P. A. E., Burton K. W., Opfergelt S., Eiríksdóttir E. S., Murphy M. J., Einarsson A. and Gislason S. R. (2016) The effect of hydrothermal spring weathering processes and primary productivity on lithium isotopes: Lake Myvatn, Iceland. *Chem. Geol.* **445**, 4–13.

Pogge von Strandmann P. A. E., Elliott T., Marschall H. R., Coath C., Lai Y. J., Jeffcoate A. B. and Ionov D. A. (2011) Variations of Li and Mg isotope ratios in bulk chondrites and mantle xenoliths. *Geochim. Cosmochim. Acta* **75**, 5247–5268.

Poitrasson F., Mao X., Mao S. S., Freydier R. and Russo R. E. (2003) Comparison of Ultraviolet Femtosecond and Nanosecond Laser Ablation Inductively Coupled

References

Plasma Mass Spectrometry Analysis in Glass, Monazite, and Zircon. *Anal. Chem.* **75**, 6184–6190.

Pouchou J. L. and Pichoir F. (1991) Quantitative analysis of homogeneous or stratified microvolumes applying the model "PAP." In *Electron Probe Quantitation* (eds. K. F. J. Heinrich and D. E. Newbury). Springer, Boston, MA. pp. 31–32.

Purton J. A., Allan N. L. and Blundy J. D. (1997) Calculated solution energies of heterovalent cations in forsterite and diopside: Implications for trace element partitioning. *Geochim. Cosmochim. Acta* **61**, 3927–3936.

Qi H., Taylor P., Berglund M. and De Bièvre P. (1997) Calibrated measurements of the isotopic composition and atomic weight of the natural Li isotopic reference material IRMM-016. *Int. J. Mass Spectrom. Ion Process.* **171**, 263–268.

Qian Q., O'Neill H. S. C. and Hermann J. (2010) Comparative diffusion coefficients of major and trace elements in olivine at ~950 °C from a xenocryst included in dioritic magma. *Geology* **38**, 331–334.

Richet P. (2003) *Guide des volcans de France*. 1st ed.. BRGM, Belin, Paris.

Richter F., Chaussidon M., Bruce Watson E., Mendybaev R. and Homolova V. (2017) Lithium isotope fractionation by diffusion in minerals Part 2: Olivine. *Geochim. Cosmochim. Acta* **219**, 124–142.

Richter F. M., Dauphas N. and Teng F. Z. (2009) Non-traditional fractionation of non-traditional isotopes: Evaporation, chemical diffusion and Soret diffusion. *Chem. Geol.* **258**, 92–103.

Richter F. M., Davis A. M., DePaolo D. J. and Watson E. B. (2003) Isotope fractionation by chemical diffusion between molten basalt and rhyolite. *Geochim. Cosmochim. Acta* **67**, 3905–3923.

Richter F. M., Liang Y. and Davis A. M.

(1999) Isotope fractionation by diffusion in molten oxides. *Geochim. Cosmochim. Acta* **63**, 2853–2861.

Richter F., Watson B., Chaussidon M., Mendybaev R. and Ruscitto D. (2014) Lithium isotope fractionation by diffusion in minerals. Part 1: Pyroxenes. *Geochim. Cosmochim. Acta* **126**, 352–370.

Le Roux P. J. (2010) Lithium isotope analysis of natural and synthetic glass by laser ablation MC-ICP-MS. *J. Anal. At. Spectrom.* **25**, 1033–1038.

Rudnick R. L. and Ionov D. A. (2007) Lithium elemental and isotopic disequilibrium in minerals from peridotite xenoliths from far-east Russia: Product of recent melt/fluid-rock reaction. *Earth Planet. Sci. Lett.* **256**, 278–293.

Rudnick R. L., Tomascak P. B., Njo H. B. and Gardner L. R. (2004) Extreme lithium isotopic fractionation during continental weathering revealed in saprolites from South Carolina. *Chem. Geol.* **212**, 45–57.

Ruprecht P., Bergantz G. W. and Dufek J. (2008) Modeling of gas-driven magmatic overturn: Tracking of phenocryst dispersal and gathering during magma mixing. *Geochemistry, Geophys. Geosystems* **9**, Q07017.

Ryan J. G. and Kyle P. R. (2004) Lithium abundance and lithium isotope variations in mantle sources: Insights from intraplate volcanic rocks from Ross Island and Marie Byrd Land (Antarctica) and other oceanic islands. *Chem. Geol.* **212**, 125–142.

Ryan J. G. and Langmuir C. H. (1987) The systematics of lithium abundances in young volcanic rocks. *Geochim. Cosmochim. Acta* **51**, 1727–1741.

Saha M. N. (1920) LIII. Ionization in the solar chromosphere. *London, Edinburgh, Dublin Philos. Mag. J. Sci.* **40**, 472–488.

Sakuyama M. and Kushiro I. (1979) Vesiculation of hydrous andesitic melt and transport of alkalies by separated vapor

References

phase. *Contrib. to Mineral. Petrol.* **71**, 61–66.

Schauble E. A. (2004) Applying stable isotope fractionation theory to new systems. *Rev. Mineral. Geochemistry* **55**, 65–111.

Schiavi F., Kobayashi K., Moriguti T., Nakamura E., Pompilio M., Tiepolo M. and Vannucci R. (2010) Degassing, crystallization and eruption dynamics at Stromboli: Trace element and lithium isotopic evidence from 2003 ashes. *Contrib. to Mineral. Petrol.* **159**, 541–561.

Schuessler J. A. and Von Blanckenburg F. (2014) Testing the limits of micro-scale analyses of Si stable isotopes by femtosecond laser ablation multicollector inductively coupled plasma mass spectrometry with application to rock weathering. *Spectrochim. Acta - Part B At. Spectrosc.* **98**, 1–18.

Seitz H.-M., Brey G. P., Lahaye Y., Durali S. and Weyer S. (2004) Lithium isotopic signatures of peridotite xenoliths and isotopic fractionation at high temperature between olivine and pyroxenes. *Chem. Geol.* **212**, 163–177.

Seitz H.-M., Brey G. P., Weyer S., Durali S., Ott U., Münker C. and Mezger K. (2006) Lithium isotope compositions of Martian and lunar reservoirs. *Earth Planet. Sci. Lett.* **245**, 6–18.

Seitz H.-M. and Woodland A. B. (2000) The distribution of lithium in peridotitic and pyroxenitic mantle lithologies - an indicator of magmatic and metasomatic processes. *Chem. Geol.* **166**, 47–64.

Shannon R. D. (1976) Revised effective ionic radii in halides and chalcogenides. *Acta Crystallogr.* **A32**, 751–767.

Sio C. K. I., Dauphas N., Teng F. Z., Chaussidon M., Helz R. T. and Roskosz M. (2013) Discerning crystal growth from diffusion profiles in zoned olivine by in situ Mg-Fe isotopic analyses. *Geochim. Cosmochim. Acta* **123**, 302–321.

Spandler C. and O'Neill H. S. C. (2010) Diffusion and partition coefficients of minor and trace elements in San Carlos olivine at 1,300°C with some geochemical implications. *Contrib. to Mineral. Petrol.* **159**, 1–28.

Spandler C., O'Neill H. S. C. and Kamenetsky V. S. (2007) Survival times of anomalous melt inclusions from element diffusion in olivine and chromite. *Nature* **447**, 303–306.

Steinmann L. K., Oeser M., Horn I., Seitz H.-M. and Weyer S. (2019) In situ high-precision lithium isotope analyses at low concentration levels with femtosecond-LA-MC-ICP-MS. *J. Anal. At. Spectrom.* **34**, 1447–1458.

Strelow F. W. E., Weinert C. H. S. W. and Van Der Walt T. N. (1974) Separation of lithium from sodium, beryllium and other elements by cation-exchange chromatography in nitric acid-methanol. *Anal. Chim. Acta* **71**, 123–132.

Su B. X., Zhou M. F. and Robinson P. T. (2016) Extremely large fractionation of Li isotopes in a chromitite-bearing mantle sequence. *Sci. Rep.* **6**, 1–9.

Tang Y. J., Zhang H. F., Deloule E., Su B. X., Ying J. F., Xiao Y. and Hu Y. (2012) Slab-derived lithium isotopic signatures in mantle xenoliths from northeastern North China Craton. *Lithos* **149**, 79–90.

Tang Y., Zhang H. and Ying J. (2007) Review of the Lithium Isotope System as a Geochemical Tracer. *Int. Geol. Rev.* **49**, 374–388.

Tanner S. D. (1995) Characterization of ionization and matrix suppression in inductively coupled 'cold' plasma mass spectrometry. *J. Anal. At. Spectrom.* **10**, 905–921.

Taura H., Yurimoto H., Kurita K. and Sueno S. (1998) Pressure dependence on partition coefficients for trace elements between olivine and the coexisting melts. *Phys. Chem. Miner.* **25**, 469–484.

References

Taylor T. I. and Urey H. C. (1938) Fractionation of the lithium and potassium isotopes by chemical exchange with zeolites. *J. Chem. Phys.* **6**, 429–438.

Teng F. Z., Dauphas N., Helz R. T., Gao S. and Huang S. (2011) Diffusion-driven magnesium and iron isotope fractionation in Hawaiian olivine. *Earth Planet. Sci. Lett.* **308**, 317–324.

Teng F. Z., Li W. Y., Rudnick R. L. and Gardner L. R. (2010) Contrasting lithium and magnesium isotope fractionation during continental weathering. *Earth Planet. Sci. Lett.* **300**, 63–71.

Teng F. Z., McDonough W. F., Rudnick R. L., Dalpé C., Tomascak P. B., Chappell B. W. and Gao S. (2004) Lithium isotopic composition and concentration of the upper continental crust. *Geochim. Cosmochim. Acta* **68**, 4167–4178.

Teng F. Z., McDonough W. F., Rudnick R. L. and Walker R. J. (2006) Diffusion-driven extreme lithium isotopic fractionation in country rocks of the Tin Mountain pegmatite. *Earth Planet. Sci. Lett.* **243**, 701–710.

Teng F. Z., McDonough W. F., Rudnick R. L. and Wing B. A. (2007a) Limited lithium isotopic fractionation during progressive metamorphic dehydration in metapelites: A case study from the Onawa contact aureole, Maine. *Chem. Geol.* **239**, 1–12.

Teng F. Z., Rudnick R. L., McDonough W. F. and Wu F. Y. (2009) Lithium isotopic systematics of A-type granites and their mafic enclaves: Further constraints on the Li isotopic composition of the continental crust. *Chem. Geol.* **262**, 370–379.

Teng F. Z., Wadhwa M. and Helz R. T. (2007b) Investigation of magnesium isotope fractionation during basalt differentiation: Implications for a chondritic composition of the terrestrial mantle. *Earth Planet. Sci. Lett.* **261**, 84–92.

Teng F. Z., Yang W., Rudnick R. L. and Hu Y. (2013) Heterogeneous magnesium isotopic composition of the lower continental crust: A xenolith perspective. *Geochemistry, Geophys. Geosystems* **14**, 3844–3856.

Tomascak P. B. (2004) Developments in the Understanding and Application of Lithium Isotopes in the Earth and Planetary Sciences. *Rev. Mineral. Geochemistry* **55**, 153–195.

Tomascak P. B., Carlson R. W. and Shirey S. B. (1999a) Accurate and precise determination of Li isotopic compositions by multi-collector sector ICP-MS. *Chem. Geol.* **158**, 145–154.

Tomascak P. B., Langmuir C. H., Le Roux P. J. and Shirey S. B. (2008) Lithium isotopes in global mid-ocean ridge basalts. *Geochim. Cosmochim. Acta* **72**, 1626–1637.

Tomascak P. B., Magna T. and Dohmen R. (2016) *Advances in Lithium Isotope Geochemistry*. 1st ed., Springer International Publishing, Cham, Heidelberg, New York, Dordrecht, London.

Tomascak P. B., Tera F., Helz R. T. and Walker R. J. (1999b) The absence of lithium isotope fractionation during basalt differentiation : New measurements by multicollector sector ICP-MS. *Geochim. Cosmochim. Acta* **63**, 907–910.

Tomascak P. B., Widom E., Benton L. D., Goldstein S. L. and Ryan G. (2002) The control of lithium budgets in island arcs. *Earth Planet. Sci. Lett.* **196**, 227–238.

Umino S. and Horio A. (1998) Multistage magma mixing revealed in phenocryst zoning of the Yunokuchi Pumice, Akagi Volcano, Japan. *J. Petrol.* **39**, 101–124.

Vanhaecke F., Dams R. and Vandecasteele C. (1993) 'Zone model' as an explanation for signal behaviour and non-spectral interferences in inductively coupled plasma mass spectrometry. *J. Anal. At. Spectrom.* **8**, 433–438.

References

Vlastélic I., Koga K., Chauvel C., Jacques G. and Télouk P. (2009) Survival of lithium isotopic heterogeneities in the mantle supported by HIMU-lavas from Rurutu Island, Austral Chain. *Earth Planet. Sci. Lett.* **286**, 456–466.

Vlastélic I., Staudacher T., Bachèlery P., Télouk P., Neuville D. and Benbakkar M. (2011) Lithium isotope fractionation during magma degassing: Constraints from silicic differentiates and natural gas condensates from Piton de la Fournaise volcano (Réunion Island). *Chem. Geol.* **284**, 26–34.

Webster J. D., Holloway J. R. and Hervig R. L. (1989) Partitioning of lithophile trace elements between H 2O and H 2O + CO 2 fluids and topaz rhyolite melt. *Econ. Geol.* **84**, 116–134.

Weyer S. and Ionov D. A. (2007) Partial melting and melt percolation in the mantle: The message from Fe isotopes. *Earth Planet. Sci. Lett.* **259**, 119–133.

Weyer S. and Seitz H.-M. (2012) Coupled lithium- and iron isotope fractionation during magmatic differentiation. *Chem. Geol.* **294**–**295**, 42–50.

Weyrauch M., Zipfel J. and Weyer S. (2019) Origin of metal from CB chondrites in an impact plume – A combined study of Fe and Ni isotope composition and trace element abundances. *Geochim. Cosmochim. Acta* **246**, 123–137.

Wunder B., Meixner A., Romer R. L., Feenstra A., Schettler G. and Heinrich W. (2007) Lithium isotope fractionation between Li-bearing staurolite, Li-mica and aqueous fluids: An experimental study. *Chem. Geol.* **238**, 277–290.

Wunder B., Meixner A., Romer R. L. and Heinrich W. (2006) Temperature-dependent isotopic fractionation of lithium between clinopyroxene and high-pressure hydrous fluids. *Contrib. to Mineral. Petrol.* **151**, 112–120.

Wunder B., Meixner A., Romer R. L. and Jahn S. (2011) Li-isotope fractionation between silicates and fluids: Pressure dependence and influence of the bonding environment. *Eur. J. Mineral.* **23**, 333–342.

Xu R., Liu Y., Tong X., Hu Z., Zong K. and Gao S. (2013) In-situ trace elements and Li and Sr isotopes in peridotite xenoliths from Kuandian, North China Craton: Insights into Pacific slab subduction-related mantle modification. *Chem. Geol.* **354**, 107–123.

You C.-F. and Chan L.-H. (1996) Precise determination of lithium isotopic composition in low concentration natural samples. *Geochim. Cosmochim. Acta* **60**, 909–915.

Zack T., Tomascak P. B., Rudnick R. L., Dalpé C. and McDonough W. F. (2003) Extremely light Li in orogenic eclogites: The role of isotope fractionation during dehydration in subducted oceanic crust. *Earth Planet. Sci. Lett.* **208**, 279–290.

Zanetti A., Tiepolo M., Oberti R. and Vannucci R. (2004) Trace-element partitioning in olivine: Modelling of a complete data set from a synthetic hydrous basanite melt. *Lithos* **75**, 39–54.

Zhao X., Zhang H., Zhu X., Tang S. and Tang Y. (2010) Iron isotope variations in spinel peridotite xenoliths from North China Craton: Implications for mantle metasomatism. *Contrib. to Mineral. Petrol.* **160**, 1–14.

Zhukova I., O'Neill H. and Campbell I. H. (2017) A subsidiary fast-diffusing substitution mechanism of Al in forsterite investigated using diffusion experiments under controlled thermodynamic conditions. *Contrib. to Mineral. Petrol.* **172**, 1–12.

Appendix

Appendix Chapter 1

Table A.1.1: Conditions of the Neptune Plus MC-ICP-MS

MC-ICP-MS	ThermoScientific Neptune Plus
Cool gas (Ar)	15 l/min
Auxiliary gas (Ar)	0.7 – 0.8 l/min
Sample gas (Ar)	1.18 – 1.2 l/min
Carrier gas (He)	0.75 – 0.81 l/min
RF power	900 W
Sample cone	Ni H
Skimmer cone	Ni X

Table A.1.2: Calculation for error propagation

Noise Error	Step 1	$$NE = \frac{SE}{(\text{measured signal})}$$
	Step 2	$$NE_{\frac{^7Li}{^6Li}} = \sqrt{(\text{RSE}_{\text{detector}_{^7\text{Li}}})^2 + (\text{RSE}_{\text{detector}_{^6Li}})^2}$$
Counting error	Step 1	See Eq. (1.3)
	Step 2	See Eq. (1.4)
Total error		$$TE_{\frac{^7Li}{^6Li}} = \sqrt{(NE_{\frac{^7Li}{^6Li}})^2 + (CE_{\frac{^7Li}{^6Li}})^2}$$

Appendix

Table A.1.3: δ⁷Li values measured by fs-LA-MC-ICP-MS in this study

δ⁷Li (‰)	MPI-DING reference glasses								USGS reference glasses		
	KL2-G	ML3B-G	GOR128-G		ATHO-G	T1-G	StHs6/80-G		BIR-1G	BCR-2G	BHVO-2G
	6.5	5.1	12.6	13.6	2.1	1.7	2.1	3.7	4.8	5.1	4.8
	6.5	5.8	12.0	11.9	3.2	0.3	2.4	3.5	3.3	3.9	4.1
	5.5	5.2	12.9	16.7	1.8	2.4	2.9	1.6	2.7	3.2	5.7
	3.9	3.6	15.2	16.2	5.0	1.7	2.0	5.1	4.0	4.1	5.8
	3.9	1.7	14.3	13.7	4.4	1.9	5.6		2.8	4.5	6.3
	2.1	3.4	14.2	12.1	3.5	0.8	3.4		2.7	5.9	5.9
	5.7	2.3	14.5	12.7	4.4	1.2	2.5		3.2	4.8	6.8
	5.2	2.1	15.7	12.1	4.5	-0.2	2.1		2.8	3.0	7.7
	4.3	2.2	14.0	13.6	6.5	1.8	3.7		3.2	2.7	8.9
	4.7	2.0	15.9		4.8	1.9	2.2		5.4	5.6	5.6
		1.0	14.3			0.6	3.2		4.5		7.1
			13.4			-0.6	2.7				
			13.0			2.4	3.0				
			14.7			1.9	3.8				
			12.2			0.7	2.3				
			13.3			3.2	3.6				
			15.6			0.5	2.9				
			14.7			0.3	2.9				
mean	4.8	3.1	13.9		4.0	1.2	3.1		3.6	4.3	6.2
2 SD	2.7	3.2	2.8		2.8	2.0	1.9		1.9	2.2	2.7
n	10	11	27		10	18	22		11	10	11

Appendix

Appendix Chapter 2

Table A.2.1: Concentrations in the multi-element solution mixed for column calibration

Element	Concentration in multi-element solution(μg/g)	Manufacturer	Compound in 2-3 % HNO_3	Concentration in stock solution (mg/l)
Al	103.0	Merck	Al-$(NO_3)_3$	1,000
Ca	103.6	Merck	$Ca(NO_3)_2$	10,000
Fe	107.7	Merck	$Fe(NO_3)_3$*	10,000
Mg	105.0	Merck	$Mg(NO_3)_2$	10,000
Na	51.6	Merck	$NaNO_3$	10,000
Ni	50.3	Merck	$Ni(NO_3)_2$	10,000
Mn	50.9	Merck	$Mn(NO_3)_2$	1,000
Ti	51.4	Alfa Aesar	Ti[#]	1,000
Li	20.4	Merck	$LiNO_3$	1,000

* 10 % HNO_3

[#] 5 % HNO_3, traces HF

Table 2.2: Dissolution procedure of powdered rock samples for Li analysis

Step	Acid	Heating on hot plate	Evaporation
1	1 ml conc. HNO_3* + 3 ml 40% HF	140°C for 2 days	100°C
2	1.3 ml conc. HNO_3 + 2.6 ml 9 M HCL	120°C for 1 day	120°C
3	4 ml conc. HNO_3	120°C for 1 day	120°C
4	4 ml 6 M HCL	120°C for 1 day	120°C
5	4 ml 6 M HNO_3	120°C for 1 day	120°C
6[#]	take up in 5 ml 5 M HNO_3		

* conc. HNO_3 = 14.5 M HNO_3

[#] solution for storage

Appendix
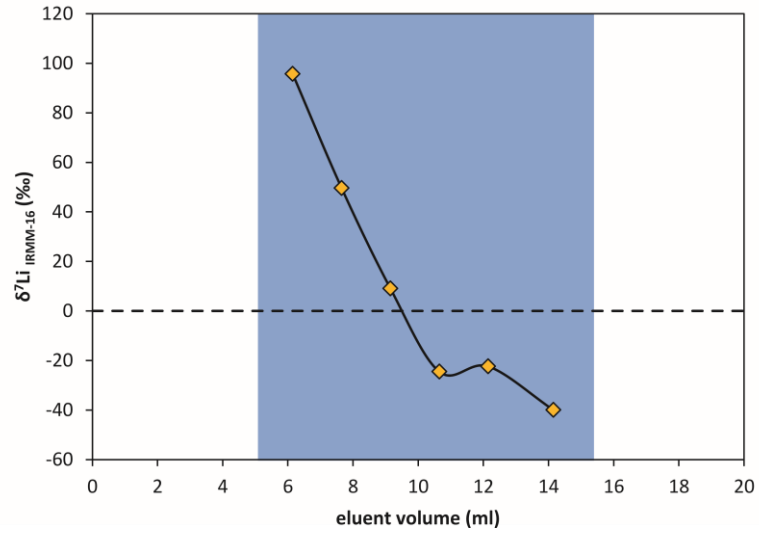
Figure A.2.1: Isotopic composition of 2 ml fractions washed off the column.
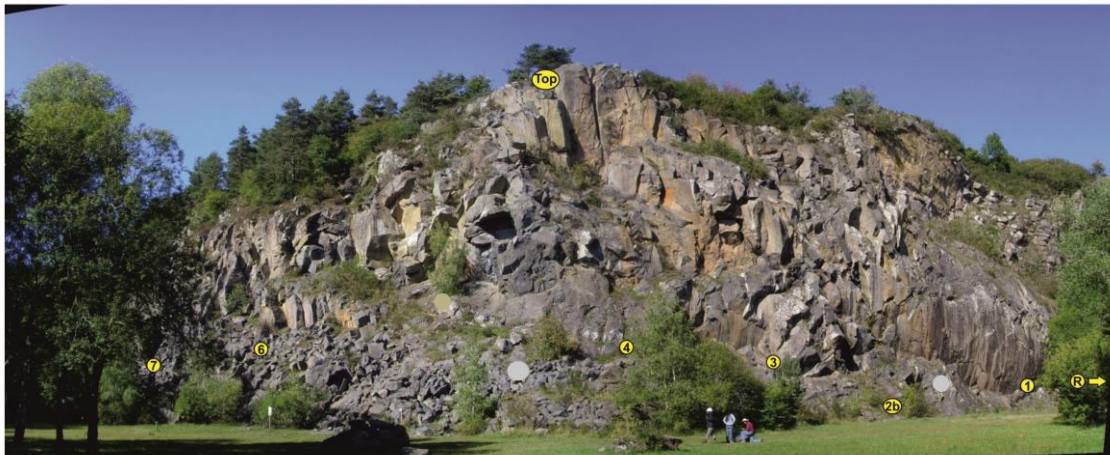
Figure A.2.2: Outcrop of Roche Sauterre. Photo by Martin Oeser, published in Oeser 2015, slightly modified. Persons for scale, view towards north.

Appendix

Appendix Chapter 3

Table A.3.1: Analytical uncertainties for trace elements in internal reference material BIR-1G measured by fs-LA-SF-ICP-MS, calibrated with BCR-2G, internal standard SiO_2

Element	Isotopic mass analyzed	Unit	Reference *	Mean	Median	SD	RSD (%)	n
Li	**7**	**µg/g**	3.0	3.3	3.2	0.1	3.8	25
Na_2O	**23**	**wt%**	1.85	1.84	1.81	0.09	5.0	25
MgO	**25**	**wt%**	9.6	10.0	9.9	0.3	2.8	25
Al_2O_3	**27**	**wt%**	15.5	15.3	15.1	0.5	3.5	25
SiO_2[#]	**29**	**wt%**	47.5	-	-	-	-	-
P_2O_5	**31**	**wt%**	0.027	0.047	0.044	0.008	16.8	25
CaO	**43**	**wt%**	13.3	12.7	12.7	0.3	2.4	25
Sc	**45**	**µg/g**	43.0	42.0	41.6	1.4	3.3	25
TiO_2	**47**	**wt%**	1.00	0.94	0.93	0.03	2.7	25
V	**51**	**µg/g**	326	322	321	8	2.5	25
Cr	**53**	**µg/g**	392	356	355	31	8.7	25
MnO	**55**	**wt%**	0.175	0.177	0.177	0.004	2.4	25
FeO	**57**	**wt%**	10.4	10.2	10.3	0.5	4.5	25
Co	**59**	**µg/g**	52.0	53.3	53.2	1.3	2.5	25
Ni	**60**	**µg/g**	176	193	161	112	58.0	25
Cu	**63**	**µg/g**	119	105	110	11	10.6	25
Y	**89**	**µg/g**	14.3	14.7	14.6	0.5	3.6	25
Zr	**90**	**µg/g**	14.0	13.8	13.7	0.5	3.4	25
La	**139**	**µg/g**	0.61	0.59	0.59	0.03	4.7	25
Pr	**141**	**µg/g**	0.37	0.38	0.37	0.02	5.1	25
Sm	**147**	**µg/g**	1.09	1.14	1.12	0.07	6.0	25
Tb	**159**	**µg/g**	0.35	0.35	0.34	0.02	6.5	25
Ho	**165**	**µg/g**	0.56	0.55	0.54	0.03	6.0	25
Tm	**169**	**µg/g**	0.24	0.26	0.26	0.02	7.6	25
Yb	**172**	**µg/g**	1.64	1.65	1.63	0.10	5.8	25

* Preferred values reported in the GeoREM database (Jochum et al. 2005)

[#] applied as internal standard

Appendix
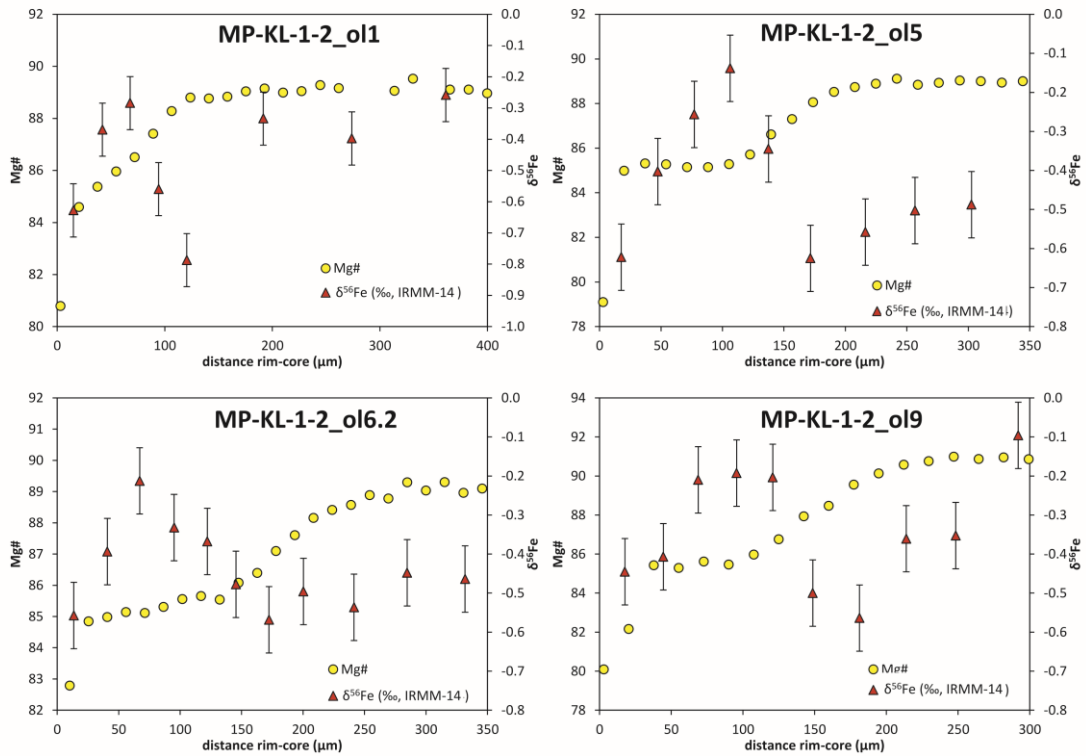
Figure A.3.1: Mg# and δ⁵⁶Fe with variations of ~0.5 ‰ within the isotope profiles, changes are coinciding with changes in Mg# (δ⁵⁶Fe values have been measured by M. Oeser-Rabe). The analytical procedure for Fe isotope measurements by fs-LA-MC-ICP-MS has been described by Oeser et al. (2014). For *in situ* Fe isotope analysis a Ni H-type sample and skimmer X-type cones have been employed. The masses ⁵³Cr, ⁵⁴Fe, ⁵⁶Fe, ⁵⁷Fe, ⁵⁸Ni and ⁶⁰Ni were measured simultaneously in high mass resolution mode with the injection of a Ni solution (NIST SRM 986) with known isotopic composition for instrumental mass bias correction and ⁵³Cr is measured for isobaric interference correction of ⁵⁴Cr on ⁵⁴Fe. The alignment of measurement lines to measure isotope profiles from rim to core of the crystals is performed similarly to the approach used for Li isotopes.

Appendix

Table A.3.2: Forsterite and Lithium concentrations in the rims, mantles and cores of Klyuchevskoy olivines

	sample	type	core Fo	mantle Fo	rim Fo	core Li (µg/g)	mantle Li (µg/g)	rim Li (µg/g)
F-cone	ol 1	A*	89	x	81	2.2	x	3.3
	ol 2	A	87-88	x	81	2.4	x	2.9
	ol 3	A	85-86	x	80	2.9	x	3.0
	ol 4	A	85-86	x	80	2.7	x	2.9
	ol 5	B'	89	85-86	79	2.3	2.9	3.3
	ol6_1	B	89	85-86	81	2.5	3.1	3.0
	ol6_2	B	89	85-86	81	2.1	2.8	2.9
	ol 7	B	90	85-86	80	2.2	3.1	3.9
	ol 8	C#/B	90	88	79	2.1	2.3	2.6
	ol 9	B	91	85-86	80	1.8	3.5	3.1
	ol 10	B	87	85-86	81	2.9	2.7	2.9
E cone	ol1	A	81	x	79	2.8	x	4.5
	ol2	A	87	x	78	2.7	x	3.7
	ol3	A	82	x	77	2.7	x	2.8
	ol4	C	81-82	83	81	2.5	2.6	3.2
	ol5	B	88	83	77	2.7	2.7	2.8
	ol6	B	89	83	79	2.5	2.8	3.0
	ol7	B	89	81	79	2.4	2.7	2.9
	ol8	A	88	x	81	2.7	x	3.0
	ol9	C	73	82	80	5.8	3.3	3.1
	ol10	D+	69	x	73	6.4	x	5.9
	ol11	A	87	x	79	2.3	x	3.1
Bilyukai	ol1	C	74	73	70	6.1	5.7	6.6
	ol2	B	80	73	65	3.7	6.7	7.2
	ol3	C	79	80	75	3.7	3.7	4.9
	ol8	B	82	73-74	70	3.4	6.0	7.0
	ol9	B	83	75	70	3.4	4.3	6.3
	ol11	A	80	x	70	3.8	x	5.9

* normally zoned crystal: Mg-rich core, Fe-rich rim

' complexly zoned crystal with mantle: mantle more Fe-rich than core, rim more Fe-rich than mantle

complexly zoned crystal with mantle: mantle more Mg-rich than core, rim more Fe-rich than core

+ reversely zoned crystal: Fe-rich core, Mg-rich rim

Appendix

Table A.3.4: Γ_{Mg-Fe} and Γ_{Li}, $\Gamma_{Li}/\Gamma_{Mg-Fe}$, for the Klyuchevskoy and SFA sample suites

Sample		Γ_{Mg-Fe} (m²)	Γ_{Li} (m²)	$\Gamma_{Li}/\Gamma_{Mg-Fe}$	Model-type
MP-KL-1-2	ol1	$1.5*10^{-9}$	$2.1*10^{-9}$	1.4	infinite
	ol2	$1.0*10^{-9}$	$1.2*10^{-9}$	1.2	semi-infinite
	ol3	$3.0*10^{-10}$	$6.0*10^{-10}$	2.0	semi-infinite
	ol4	$1.0*10^{-10}$	$2.0*10^{-10}$	2.0	semi-infinite
	ol5	$5.5*10^{-10}$	$1.7*10^{-9}$	3.0	infinite
	ol6_1	$1.0*10^{-9}$	$1.1*10^{-9}$	1.1	infinite
	ol6_2	$1.0*10^{-9}$	$1.0*10^{-9}$	1.0	infinite
	ol7	$6.0*10^{-10}$	$8.4*10^{-10}$	1.4	infinite
	ol8	$3.0*10^{-10}$	$9.0*10^{-10}$	3.0	infinite
	ol9	$6.0*10^{-10}$	$7.8*10^{-10}$	1.3	infinite
	ol10	$6.0*10^{-10}$	$1.1*10^{-9}$	1.8	infinite
MP-KL-2-2	ol1	$4.0*10^{-10}$	$5.2*10^{-10}$	1.3	semi-infinite
	ol2	$2.0*10^{-9}$	$2.4*10^{-9}$	1.2	semi-infinite
	ol3	$2.0*10^{-10}$	$4.0*10^{-10}$	2.0	semi-infinite
	ol4	$1.5*10^{-10}$	$2.3*10^{-10}$	1.5	infinite
	ol4	$1.5*10^{-10}$	$2.3*10^{-10}$	1.5	semi-infinite
	ol5	$7.0*10^{-10}$	$1.4*10^{-9}$	2.0	infinite
	ol6	$4.0*10^{-10}$	$6.0*10^{-10}$	1.5	infinite
	ol7	$3.0*10^{-10}$	$3.6*10^{-10}$	1.2	infinite
	ol8	$2.0*10^{-10}$	$2.4*10^{-10}$	1.2	semi-infinite
	ol9	$6.0*10^{-10}$	$4.8*10^{-10}$	0.8	infinite
	ol10	$2.0*10^{-10}$	$2.4*10^{-10}$	1.2	semi-infinite
	ol11	$6.0*10^{-10}$	$7.2*10^{-10}$	1.2	semi-infinite
MP-KL-4-3	ol1	$1.5*10^{-10}$	$2.3*10^{-10}$	1.5	infinite
	ol1	$8.0*10^{-11}$	$3.2*10^{-10}$	4.0	semi-infinite
	ol2	$4.0*10^{-10}$	$5.6*10^{-10}$	1.4	infinite
	ol3	$3.0*10^{-10}$	$6.0*10^{-10}$	2.0	infinite
	ol3	$1.5*10^{-10}$	$1.8*10^{-10}$	1.2	semi-infinite
	ol8	$8.0*10^{-10}$	$9.6*10^{-10}$	1.2	infinite
	ol9	$7.0*10^{-10}$	$8.4*10^{-10}$	1.2	infinite
	ol11	$6.5*10^{-10}$	$7.2*10^{-10}$	1.2	semi-infinite
Arafo	ol1	$8.0*10^{-10}$	$1.2*10^{-9}$	1.5	infinite
	ol2	$8.0*10^{-10}$	$1.2*10^{-9}$	1.5	semi-infinite
	ol6	$3.0*10^{-10}$	$3.6*10^{-10}$	1.2	semi-infinite
	ol7	$4.0*10^{-10}$	$4.8*10^{-10}$	1.2	infinite

Appendix

	ol8	$4.0*10^{-10}$	$4.8*10^{-10}$	1.2	semi-infinite
	ol9	$1.0*10^{-10}$	$1.6*10^{-10}$	1.6	semi-infinite
	ol11	$1.0*10^{-10}$	$2.5*10^{-10}$	2.5	semi-infinite
	ol14	$1.0*10^{-10}$	$2.0*10^{-10}$	2.0	infinite
	ol18	$4.0*10^{-10}$	$1.0*10^{-10}$	2.5	semi-infinite
	ol19	$4.0*10^{-10}$	$7.2*10^{-10}$	1.8	semi-infinite
	ol20	$3.0*10^{-10}$	$5.1*10^{-10}$	1.7	semi-infinite
Siete Fuentes	ol1	$1.5*10^{-10}$	$2.3*10^{-10}$	1.5	infinite
	ol2	$1.5*10^{-10}$	$2.3*10^{-10}$	1.5	infinite
	ol2	$8.0*10^{-11}$	$3.2*10^{-10}$	4.0	semi-infinite
	ol4	$8.0*10^{-11}$	$2.0*10^{-10}$	2.5	semi-infinite
	ol4	$1.0*10^{-10}$	$1.5*10^{-10}$	1.5	infinite
	ol5	$5.0*10^{-11}$	$2.0*10^{-10}$	4.0	semi-infinite
	ol6	$1.5*10^{-10}$	$6.0*10^{-10}$	4.0	semi-infinite
	ol7	$1.0*10^{-10}$	$4.2*10^{-10}$	4.2	semi-infinite
	ol8	$3.0*10^{-10}$	$9.0*10^{-10}$	3.0	semi-infinite
	ol9	$1.0*10^{-10}$	$1.5*10^{-10}$	1.5	infinite
	ol11	$1.0*10^{-10}$	$4.0*10^{-10}$	4.0	semi-infinite
	ol12	$2.0*10^{-10}$	$3.0*10^{-10}$	1.5	infinite
	ol13	$2.0*10^{-10}$	$4.0*10^{-10}$	2.0	semi-infinite
	ol15	$5.0*10^{-11}$	$7.5*10^{-11}$	1.5	infinite
	ol16	$4.0*10^{-10}$	$4.0*10^{-10}$	1.0	semi-infinite

Appendix

Appendix Chapter 4
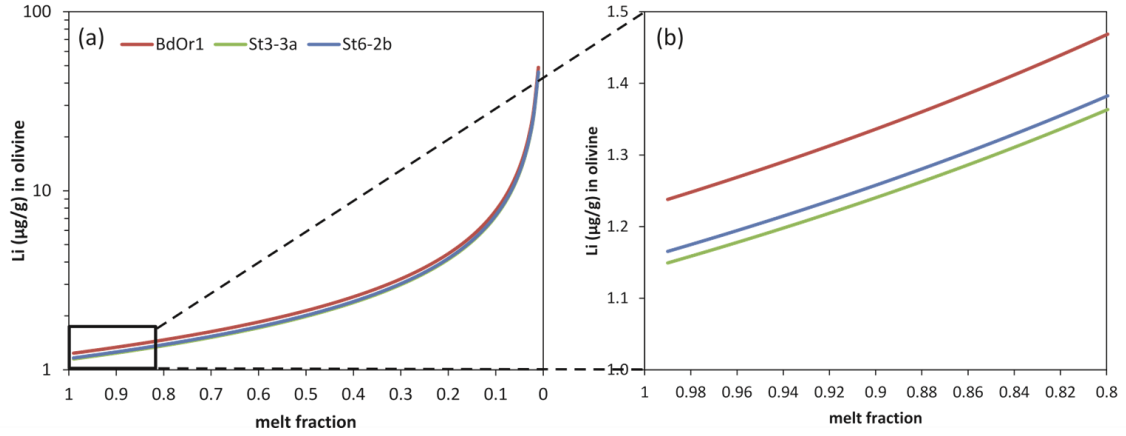
Figure A.4.1: (a) Modeled equilibrium Li concentration for fractionate crystallization with given bulk rock Li concentrations for BdOr1, St3-3a and St6-2b at $K_D = 0.2$ and **(b)** excerpt from 1 to 1.5 µg/g and a melt fraction of 0.8 to 0.99 calculated with $C_R = K_D F^{(K_D-1)} \times C_0$.for fractional crystallization with C_R = concentration of a trace element in crystallizing mineral (Li$_{core}$), K_D = partitioning coefficient, F = fraction of rest melt, C_0 = concentration of trace element in starting melt (Li$_{bulk}$). Core concentrations of the olivines are assumed to be in equilibrium with the melt they crystallized in, for this purpose whole rock Li concentration data from Oeser et al. (2015) was used for calculations (BdOr1 = 6.14 µg/g, St3-3a =5.7 µg/g and St6-2b = 5.78 µg/g(Oeser et al., 2015) and K_D=0.2 (Brenan et al., 1998; Seitz and Woodland, 2000) is applied. C_R is expected to be between 1.16 and 1.47 µg/g for a range of melt fractions from 0.98 to 0.8.

Table A.4.1: Equations for the analytical and numerical solution of the diffusion equation

Analytical solution to the diffusion equation (Crank, 1975)	$C_{semi-infinite} = C_1 + ((C_2 - C_1) \times \mathrm{erf}(\frac{x}{2\sqrt{\Gamma}})$	(Eq. A.4.1)
	$C_{infinite} = C_1 + (\frac{1}{2}(C_2 - C_1) \times \mathrm{erf}(\frac{x}{2\sqrt{\Gamma}}))$	(Eq. A.4.2)
Numerical solution to the diffusion equation (Crank, 1975; Costa et al., 2008)	$C_{i,j+1} = C_{i,j} + D\Delta t * \left(\frac{C_{i+1,j} - 2C_{i,j} + C_{i-1,j}}{\Delta x^2}\right)$	(Eq. A.4.3)

Appendix

Table A.4.2: Mg# and Li concentrations in Roche Sauterre and Banne D'Ordanche samples, published in (Oeser et al., 2015)

BdOr-1 ol1			BdOr-1 ol2			BdOr-1 ol-xen1			BdOr-1 ol-xen2		
distance (µm)	Mg#	Li (µg/g)	distance (µm)	Mg#	Li (µg/g)	distance (µm)	Mg#	Li (µg/g)	distance (µm)	Mg#	Li (µg/g)
35	0.805	8.5	35	0.800	6.3	64	0.822	12.5	41	0.790	8.1
98	0.862	4.7	92	0.862	7.0	133	0.851	12.4	113	0.834	4.7
161	0.884	2.8	135	0.887	5.4	184	0.869	10.2	137	0.849	4.7
223	0.888	2.0	191	0.901	3.1	233	0.876	9.0	177	0.856	3.7
283	0.888	2.0	249	0.906	2.1	298	0.879	9.1	217	0.869	3.5
342	0.887	1.6	310	0.907	1.5	356	0.879	8.7	288	0.876	2.7
404	0.887	1.7	384	0.906	1.2	436	0.881	10.5	353	0.877	2.4
466	0.888	2.2							441	0.877	2.3
524	0.887	2.2							524	0.878	2.0
590	0.888	2.0							600	0.878	2.2
646	0.887	2.4									

St3-3a ol1			St3-3a ol2			St6-2b ol4b			St6-2b ol5		
distance (µm)	Mg#	Li (µg/g)	distance (µm)	Mg#	Li (µg/g)	distance (µm)	Mg#	Li (µg/g)	distance (µm)	Mg#	Li (µg/g)
39	0.8	3.9	32	0.777	2.8	39	0.739	5.5	41	0.759	5.9
100	0.8	3.9	102	0.823	2.3	101	0.770	6.7	98	0.792	4.7
157	0.8	3.7	160	0.846	1.9	166	0.814	5.8	154	0.828	4.6
215	0.9	2.9	216	0.852	1.4	241	0.840	4.8	212	0.849	
278	0.9	2.4	262	0.854	1.4	303	0.848	4.7	272	0.864	3.7
363	0.9	1.8	337	0.853	1.1	368	0.848		329	0.865	3.3
						543	0.863	3.9	389	0.866	3.5
						633	0.859	4.0	447	0.866	3.2
						694	0.845	5.1	506	0.866	3.3
						754	0.815	4.8	561	0.866	3.2
						823	0.762	4.6	622	0.866	3.1

Appendix

Table A.4.3: Results for Lithium isotope measurement, δ⁷Li- and 2σ-values in ‰

BdOr-1_oll			BdOr-1_ol2			BdOr-1_olxen1			BdOr-1_olxen2		
distance (μm)	$\delta^7Li_{IRMM-16}$	2σ	distance (μm)	$\delta^7Li_{IRMM-16}$	2σ	distance (μm)	$\delta^7Li_{IRMM-16}$	2σ	distance (μm)	$\delta^7Li_{IRMM-16}$	2σ
60.9	2.3	2.3	28	7.4	1.9	25	5.1	1.7	22	-5.7	
100.1	-2.8	2.5	63	5.3	1.9	77	4.3	1.9	38	7.5	2.4
142.9	-2.5	2.4	102	-7.9	2.0	128	-13.1	2.2	74	-9.6	2.4
183.7	-4.1	2.9	141	-14.7	2.1	203	-9.9	1.7	121	-7.2	2.4
220.7	-5.4	2.8	172	-19.1	2.0	257	-5.9	1.7	173	-8.8	2.4
267.5	-7.7	3.0	201	-24.6	2.2	305	-10.5	1.9	236	-2.2	2.3
511.5	-11.3	3.2	238	-30.7	2.5	358	-7.7	1.6	291	-4.2	2.2
			411	-21.4	3.6	444	-5.6	1.5	351	1.9	2.4
			314	-27.4	3.1				408	3.5	2.2
									476	2.9	2.1

St3-3a_oll			St3-3a_ol2			St6-2b_ol4b			St6-2b_ol5		
distance (μm)	$\delta^7Li_{IRMM-16}$	2σ	distance (μm)	$\delta^7Li_{IRMM-16}$	2σ	distance (μm)	$\delta^7Li_{IRMM-16}$	2σ	distance (μm)	$\delta^7Li_{IRMM-16}$	2σ
26	-7.7	2.4	29	9.0	1.8	21	1.0	2.1	37	13.2	2.4
62	7.0	3.2	83	4.3	1.6	73	11.4	2.0	89	8.7	2.1
97	-0.7	3.3	135	-2.6	1.7	139	-2.1	1.9	138	-2.5	2.0
158	-7.8	1.6	198	-7.4	1.9	238	-4.3	2.0	189	-7.3	2.3
228	-12.3	1.7	254	-10.2	1.7	295	-4.2	1.9	238	-4.7	2.6
282	-11.1	1.8	309	-12.6	1.8	345	-3.6	1.8	285	-7.4	2.4
326	-11.8	2.1	367	-13.7	1.7	510	-9.7	1.9	332	-8.4	2.4
376	-14.5	1.9	423	-14.1	1.7	431	-7.7	1.9	379	-8.1	2.4
551	-14.3	1.8	500	-13.8	1.6	554	-10.7	1.8	432	-12.0	2.5
			563	-11.2	1.6	611	-8.9	1.8	478	-13.9	2.5
			666	-10.7	1.6	654	-9.2	2.0	646	-8.7	2.3
						691	-10.2	2.0			
						741	-5.7	2.0			
						784	0.5	2.0			
						826	1.7	1.9			

Appendix

Table A.4.4: Iron and magnesium isotope profiles, published in (Oeser et al., 2015)

	Fe isotopes			Mg isotopes		
	distance (μm)	$\delta^{56}Fe_{IRMM-14}$	2 SD	distance (μm)	$\delta^{26}Mg_{DSM-3}$	2 SD
BdOr-1_ol2	20	-0.386	0.070	27	-0.293	0.072
	70	-1.429	0.070	72	-0.025	0.072
	140	-2.085	0.070	122	0.015	0.072
	198	-1.526	0.070	167	-0.030	0.072
	260	-0.881	0.070	216	-0.171	0.072
	325	-0.468	0.070	273	-0.260	0.072
	385	-0.387	0.070	327	-0.239	0.072
	472	-0.414	0.070	386	-0.275	0.072
	548	-0.388	0.070			
BdOr-1_olxen2	36	-0.652	0.070	26	-0.105	0.074
	105	-1.388	0.070	72	0.099	0.074
	184	-1.757	0.070	120	-0.250	0.074
	257	-1.122	0.070	171	-0.238	0.074
	331	-1.034	0.070	226	-0.208	0.074
	409	-1.024	0.070	283	-0.287	0.074
	488	-1.020	0.070			
	560	-0.985	0.070			
	681	-1.060	0.070			
St3-3a_ol1	42	-0.389	0.090	38	-0.390	0.100
	97	-1.172	0.090	85	-0.167	0.100
	167	-1.372	0.090	138	-0.100	0.100
	228	-0.969	0.090	186	-0.101	0.100
	304	-0.559	0.090	241	-0.263	0.100
	378	-0.376	0.090	292	-0.377	0.100
	444	-0.328	0.090	347	-0.377	0.100
	520	-0.279	0.090	414	-0.414	0.100
	598	-0.289	0.090	496	-0.516	0.100
	760	-0.242	0.090	573	-0.423	0.100
	971	-0.270	0.090	760	-0.359	0.100
	1068	-0.457	0.090	946	-0.493	0.100
	1144	-0.589	0.090	990	-0.321	0.100
	1200	-0.757	0.090	1071	-0.454	0.100
	1263	-0.893	0.090	1130	-0.279	0.100
	1342	-1.147	0.090	1191	-0.385	0.100
	1427	-1.246	0.090	1251	-0.022	0.100

Curriculum Vitae

Personal Details

Name	Lena Steinmann
Date and place of birth	1989-01-10, Lindenfels
Nationality	German

Work Experience

10/2016 – 11/2019 — *Research assistant/ PhD student* at the Institut für Mineralogie, Leibniz Universität Hannover

> Lithium isotope fractionation in magmatic systems: Constraints from in situ δ^7Li determinations on magmatic minerals by femtosecond-laser ablation-MC-ICP-MS

01/2015 – 09/2016 — Student research assistant at the at Leibniz Universität Hannover, research groups Experimental Petrology and Geochemistry

11/2013 – 06/2014 — Student research assistant at Ruprecht-Karls-Universität Heidelberg, research group Petrology and Geochemistry and as tutor for lecture "physical-chemical processes in system earth"

08/2008-09/2011 — Practical terms at Alstom Power Systems GmbH, Mannheim, during studies at University of Cooperative Education Baden-Württemberg Mannheim, Germany

> Departments: Logistics, Controlling, Human Resources, market research and materials management

Education

10/2014 – 09/2016 — *Master of Science in Earth S*ciences at Gottfried Wilhelm Leibniz Universität Hannover, Germany, Specialization Mineralogy and Geochemistry

> Title of Master thesis: *"Copper Isotope and Trace Element Fractionation in lherzolites and pyroxenites from Balmuccia Peridotite Massif (Ivrea Zone, NW Italy)"*

10/2011-09/2014 — *Bachelor of Science in Earth Sciences* at Ruprecht-Karls-Universität Heidelberg, Germany, Specialization Mineralogy

> Title of Bachelor thesis: *"Metamorphic history of metabasites from the mafic complex in the Ivrea Zone (Val Mastallone, Piemont, Italy)"*

10/2008-09/2011 — *Bachelor of Arts in* Business Administration at University of Cooperative Education Baden-Württemberg Mannheim, Germany, in cooperation with Alstom Power Systems GmbH

> Title of Bachelor thesis: *"Ansätze zur Verbesserung der Bereitstellung von Teilen für die Brennkammermontage der ALSTOM Power Systems GmbH"*

09/1999-06/2008 — *Secondary school (A-levels)* Überwald-Gymnasium, Wald-Michelbach, Germany, intensive courses: Mathematics and French

Curriculum Vitae

Scholarship

10/2015 – 09/2016	Deutschlandstipendium, scholarship funded by the Federal Ministry for Education and Research and üstra AG, Hanover

Internships and Field Trips

03/2017 and 03/2018	Field trip, 10 days to Tenerife, Canary Islands as supervisor/organizer and for sample collection
09/2013 – 10/2013	Internship, 6 weeks at Fraunhofer Institute for Silicate Research, division Glass Research
07/2014 – 08/2014	Internship, 4 weeks at Freudenberg New Technologies, division Chemistry and Surface Technology
07/2010 – 09/2010	Internship at Alstom Power Systems in Rugby, UK

Additional Skills

International	Participation and presentation of scientific results at international conferences
Experience:	(USA, Italy, Spain, France)
	Travelling to Peru, China and Nepal during the last years
Short courses	03/2019-04/2019: "Patent Law in Natural Sciences", lecturer Dr. Tilman Breitenstein
	10/2018: Short course "Application of diffusion studies to the determination of timescales in geochemistry and petrology" at Ruhr Universität Bochum, lecturer: Prof. Dr. Sumit Chakraborty, Dr. Ralf Dohmen and others
	11/2017: "Introduction to Secondary Ion Mass Spectrometry in the Earth Sciences" short course at Geoforschungszentrum Potsdam, lecturer Dr. Michael Wiedenbeck
Analytical skills	femtosecond-laser ablation-MC-ICP-MS, Electron Microprobe, Secondary electron microscopy, Secondary Ion mass spectrometry, Laboratory experience
Languages:	German (native), English (very good, both oral and written), French (very good, both oral and written), Spanish (B1), Chinese (A2)
Engagement:	2018- today: vice chairwoman of the association "Freunde der Geowissenschaften Hannover e.V."
	2017-2019: student member in the advisory board of the Deutsche Mineralogische Gesellschaft

List of Publications

Peer reviewed articles:

Steinmann, L. K., Oeser, M., Horn, I., Seitz, H.-M., Weyer, S. (2019): **In situ** high-precision lithium isotope analyses at low concentration levels with femtosecond-LA-MC-ICP-MS, Journal of Analytical Atomic Spectrometry, 34, 1447-1458.

Wang, Z., Lazarov, M., **Steinmann, L. K**., Becker, H., Zou, Z., Geng, X. (2018): The distribution of lead and thallium in mantle rocks: Insights from the Balmuccia peridotite massif (Italian Alps), American Mineralogist 103, 1185-1199.

Conference Contributions:

Steinmann, L.K., Oeser, M., Almeev, R.R., Portnyagin, M., Weyer, S. (2019) Lithium chemical and isotope diffusion in natural olivines and its implications on the timing of magmatic events, GeoMünster 2019, Münster (Germany).

Steinmann, L.K., Oeser, M., Weyer, S. (2019) Correlation of Li chemical and isotope profiles with Fe-Mg inter-diffusion in volcanic olivines, Goldschmidt Conference 2019, Barcelona (Spain).

Neukampf, J., Ellis, B.S., Laurent, O., **Steinmann, L.K.,** Dohmen, R., Ubide, T., Oeser, M., Magna, T., Weyer, S., Bachmann, O. (2019) Timescales of degassing in rhyolitic magmas tracked by Li in plagioclase, Goldschmidt Conference 2019, Barcelona (Spain).

Neukampf, J., **Steinmann, L.K**., Ellis, B.S., Oeser, M., Dohmen, R., Laurent, O., Ubide, T., Magna, T., Weyer, S., Bachmann, O. (2019) Tracking degassing of explosive eruption with lithium isotopes, VSMG 2019, St. Andrews (UK).

Neukampf, J., **Steinmann, L.K.,** Ellis, B.S., Oeser, M., Dohmen, R., Ubide, T., Magna, T., Weyer, S., Bachmann, O. (2018): Lithium isotopic and concentration gradients in plagioclase – implications for pre- and syn-eruptive magmatic processes, AGU Fall Meeting 2018, Washington D.C. (USA) as presenting author.

Steinmann, L. K., Oeser, M., Horn, I., Weyer, S. (2018): Femtosecond-LA-MC-ICP-MS *in situ* analyses of Li isotopes in volcanic olivines, AGU Fall Meeting2018, Washington D.C. (USA).

List of Publications

Steinmann, L. K., Oeser, M., Horn, I., Weyer, S. (2018): *In situ* analyses of Li isotopes in olivines from volcanic rocks with femtosecond laser ablation MC-ICP-MS, Joint Meeting of DGGV, DMG and Paläontologische Gesellschaft, Bonn (Germany).

Steinmann, L. K., Oeser, M., Horn, I., Weyer, S. (2018): *In situ* analyses of Li isotopes in reference glasses and olivines with fs-LA-MC-ICP-MS, DMG section meeting geochemistry and petrology, Göttingen (Germany).

Steinmann, L. K., Oeser, M., Horn, I., Weyer, S. (2017): A new *in situ* method for Li isotope measurements with femtosecond-LA-MC-ICP-MS, ASI 2017, Jahrestagung der Arbeitsgemeinschaft Stabile Isotope e.V., Hannover (Germany).

Steinmann, L.K., Oeser, M., Horn, I., Weyer, S. (2017): New developments in Li isotope *in situ* analyses with fs-LA-MC-ICP-MS, Goldschmidt Conference 2017, Paris (France).

Steinmann, L.K., Oeser, M., Horn, I., Weyer, S. (2017): Development and application of a new in situ femtosecond-LA-MC-ICP-MS method for Li isotope measurements, GeoBremen2017, Joint Meeting of DGGV and DMG, Bremen (Germany).

Steinmann, L., Lazarov, M., Weyer, S., Wang., Z. (2016): Siderophile and Chalcophile Trace Metal Distribution in the Mantle (Balmuccia Peridotite Massif, Italy), DMG section meeting geochemistry and petrology, Bremen (Germany).

Steinmann, L., Lazarov, M., Wang, Z., Becker, H., Weyer, S. (2016): The Distribution of Siderophile and Chalcophile Trace Metals in Mantle Rocks (Balmuccia, Italy), European Mineralogical Conference 2016, Rimini (Italy).

Meyer, H.-P., Varychev, A., Grim, J., **Steinmann, L.** (2014): p-ED-XRF analyses including Na and Mg of ancient glasses, DMG Annual Meeting 2014, Jena (Germany).